UNIVERSITEIT • STELLENBOSCH • UNIVERSITY

Solar Tower Power Plant Performance Characteristics

by

Johannes Petrus Pretorius

Thesis presented at the University of Stellenbosch in partial fulfilment of the requirements for the degree of

Master of Mechanical Engineering

Department of Mechanical Engineering
University of Stellenbosch
Private Bag X1, 7602 Matieland, South Africa

Supervisors:

Prof D.G. Kröger Prof T.W. von Backström

April 2004

Declaration

I, the undersigned, hereby declare that the work contained in this thesis is my own original work and that I have not previously in its entirety or in part submitted it at any university for a degree.

Signature: .....

J.P. Pretorius

Date: .....

Pectora roborant cultus recti

Uittreksel

Uitsetkarakteristieke van 'n Sontoring-Kragstasie

("Solar Tower Power Plant Performance Characteristics")

J.P. Pretorius

Departement Meganiese Ingenieurswese
Universiteit van Stellenbosch
Privaatsak X1, 7602 Matieland, Suid-Afrika

Tesis: MScIng (Meg)

April 2004

Hierdie studie ondersoek elektrisiteitsopwekking deur grootskaalse sontoring-kragstasies. Die uitsetkarakteristieke van 'n sogenaamde verwysings-kragstasie met 'n 4000 m deursnee glas kollektor en 'n 1500 m hoë, 160 m deursnee toring word ondersoek vir 'n spesifieke ligging in Suid-Afrika. Die toepaslike trek- en behoudsvergelykings word afgelei, gediskretiseer en geimplementeer in 'n numeriese rekenaarmodel. Die rekenaarmodel los die betrokke vergelykings op deur gebruik te maak van gespesifiseerde meteorologiese invoerdata en bepaal dan die uitset gelewer deur die kragstasie.

Die uitset van 'n sontoring-kragstasie oor 'n periode van vier-en-twintig uur word getoon. Ooreenstemmende temperatuurverdelings in die grond onder die kollektor word geïllustreer. Die variasie in seisoenale elektrisiteitsopwekking word ondersoek en die totale jaarlikse elektriese uitset bepaal. Die invloed wat die kragstasie dimensies (kollektor deursnee en toring hoogte) op die uitset het, word bestudeer en resultate getoon. Daar is ook bevind dat verhoogde uitset meegebring kan word deur die vorm en hoogte van die kollektordak te optimeer. Die geringe effek van die toringskadu op die kollektor word bespreek, terwyl bevind is dat heersende winde 'n beduidende effek op die kragstasie uitset het.

Pectora roborant cultus recti

Abstract

Solar Tower Power Plant Performance Characteristics

J.P. Pretorius

Department of Mechanical Engineering
University of Stellenbosch
Private Bag X1, 7602 Matieland, South Africa

Thesis: MScEng (Mech)

April 2004

This study investigates energy generation by large-scale solar tower power plants. The performance characteristics of a so-called reference plant with a 4000 m diameter glass collector roof and a 1500 m high, 160 m diameter tower are determined for a site located in South Africa. The relevant draught and conservation equations are derived, discretized and implemented in a numerical model which solves the equations using specified meteorological input data and determines the power delivered by the plant.

The power output of a solar tower power plant over a twenty-four hour period is presented. Corresponding temperature distributions in the ground under the collector are shown. Variations in seasonal generation are evaluated and the total annual electrical output is determined. The dependency of the power output on collector diameter and tower height is illustrated, while showing that greater power production can be facilitated by optimizing the roof shape and height. The minor influence of the tower shadow falling across the collector is evaluated, while the effect of prevailing winds on the power generated is found to be significant.

Pectora roborant cultus recti

Acknowledgements

I would like to express my sincere gratitude to the following people who have contributed to making this work possible:

- Prof D.G. Kröger and Prof T.W. von Backström of the University of Stellenbosch as my supervisors,
- Dr J.D. Buys of the Mathematics Department at the University of Stellenbosch for his assistance in the development of a numerical simulation model,
- Mr D. Els of the University of Stellenbosch for his support regarding optimization and layout of this document,
- Mr C. Coetzee of the University of Stellenbosch for his advice on best programming practices.

Most of all, I am thankful to the Lord in Heaven for His grace and guidance during this study.

Contents

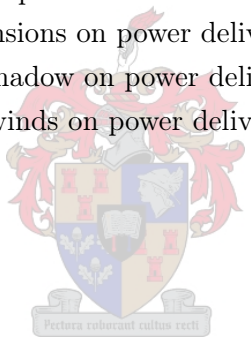

List of Figures

List of Tables

Nomenclature

Variables:

A	Area [m^2]
a	Coefficient
b	Exponent or coefficient
C	Coefficient
c	Coefficient
c_p	Specific heat capacity [J/kg·K]
d	Diameter [m]
DOY	Day of year [days]
EOT	Equation of time [minutes]
F	Force [N] or radiation transfer factor
Fr	Froude number
f	Friction factor
g	Gravitational acceleration [9.8 m/s^2]
H	Height [m]
h	Convective heat transfer coefficient [W/m^2·K]
I	Solar irradiation [W/m^2]
K	Loss coefficient
k	Thermal conductivity [W/m·K]
$\dot{m}$	Mass flow rate [kg/s]
n	Number or refractive index
P	Pitch [m] or Power [W]
p	Pressure [N/m^2]

Pr	Prandtl number
q	Heat flux [W/m^2]
r	Radius [m]
R	Gas Constant
Re	Reynolds number
t	Time [s] or thickness [m]
T	Temperature [K] or [°C]
V	Volume flow rate [m^3/s]
v	Velocity [m/s]
z	Depth in ground or axial height of tower [m]

Greek symbols:

α	Absorptivity or coefficient or angle [radians *or* degrees]
β	Coefficient
Δ	Differential
δ	Boundary layer thickness [m]
ϵ	Emissivity
ε	Roughness [m]
θ	Angle [radians *or* degrees]
μ	Dynamic viscosity [kg/m·s]
ρ	Density [kg/m^3] or reflectivity
σ	Boltzmann's constant [5.67×10^{-8} W/m^2·K^4]
$\sum$	Sum
τ	Shear stress [N/m^2] or transmissivity
ϕ	Angle [radians *or* degrees]

Subscripts:

a	Ambient air
avg	Average
b	Beam
bw	Bracing wheel
$coll$	Collector

cr	Center
cv	Control volume
D	Drag
d	Diffuse
dyn	Dynamic
e	Effective or extinction
g	Ground
gr	Ground to collector roof
gh	Ground to air under collector roof
h	Horizontal surface or air under collector roof or hydraulic
i	Inlet or node index
j	Node index
k	Node index
m	Mean
new	Next time step
o	Outlet
old	Previous time step
$\parallel$	Parallel
$\perp$	Perpendicular
p	Pressure
r	Roof or radial
ra	Collector roof to ambient air
rh	Collector roof to air under collector roof
rs	Collector roof to sky
srD	Support drag at a specific collector radius
s	Support or solar
sD	Support drag
sh	Shadow
sky	Sky
$supports$	Collector roof supports
t	Tower or tangential or total or throat

tg	Turbo-generator
ti	Tower control volume inlet or tower inlet
to	Tower control volume outlet or tower outlet
$turb$	Turbine
$turb, i$	Turbine inlet
w	Wind

Chapter 1

Introduction

With the decrease of fossil fuel resources and increasing worldwide pollution problems, there is a growing need for an environmentally friendly renewable energy source. It is vital that the utilization of this energy source be economically viable, especially for its possible use in Third World countries. Engineers and scientists are increasingly looking to solar energy as a potential answer to this problem.

Man has already tried to harness energy from the sun in various different ways. These include Parabolic Trough solar power plants, Central Receiver power plants, Dish-Stirling systems, Solar Pond power plants and Photovoltaic power plants.

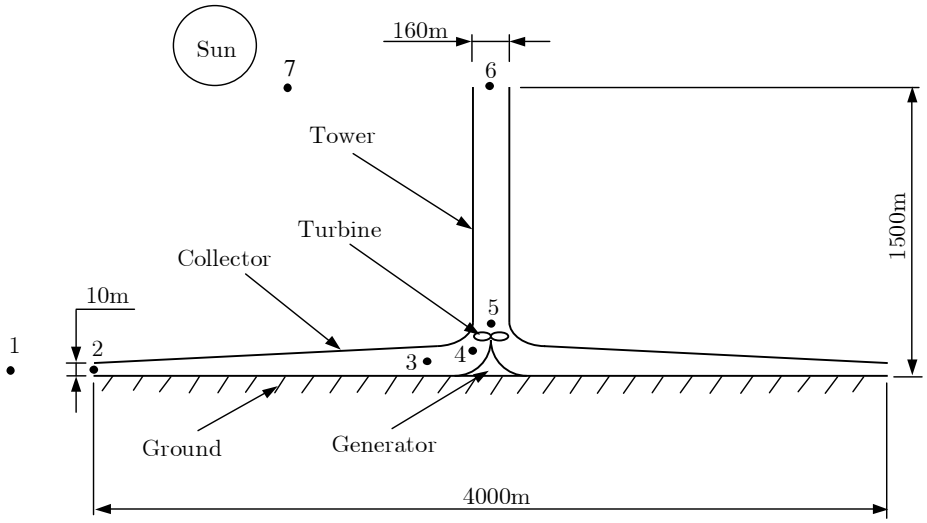

Figure 1.1: Schematic illustration of a solar tower power plant

Since the 1970's, the development of solar tower power plants have been investigated and have since become a good prospect for large scale energy generation. The solar tower power plant consists of a translucent collector (located a few meters above ground level) with a central tower which houses a turbo-generator at its base, as shown schematically in figure 1.1.

The operation of such a solar tower plant is relatively simple. Solar radiation heats the ground beneath a clear glass collector. Underneath the collector, the heated ground heats the air, causing the air to rise. The warm air is trapped under the collector but rises through the central tower, driving the turbine and consequently generating electricity.

Solar tower power plants have some advantage over the above mentioned power generation schemes, such as the Parabolic Trough and Central Receiver solar power plants. These include the use of both beam and diffuse radiation, while energy is stored naturally in the ground during the day and is released at nighttime, thus producing electricity over a twenty-four hour period. Solar towers make use of simple technologies, are built from low cost materials and have no water requirements.

1.1 Literature review

The earliest modern day reference to a solar tower concept appears in a German book by Günther & de Haas (1931), in which reference is made to a proposal by B.Dubos concerning the possibility of constructing a solar updraught power plant on the side of a steep hill or mountain, with a glass covered collector located on a relatively horizontal area near the base of the mountain. A large duct would channel heated air up the mountainside to a turbo-generator.

In 1983, Haaf *et al.* (1983) discusses the basic solar tower idea, construction and power generation principles. Haaf points out that a similar concept was used centuries ago by Leonardo da Vinci, who designed a barbecue-spit driven by an updraft through a tower. He also refers to an earlier study by Simon (1976). Some of the design features of the 50 kW pilot plant (with a 244 m diameter collector and 194.6 m high, 10 m diameter tower) built in Manzanares, Spain are mentioned. A photo of this pilot plant is shown in figure 1.2.

In a follow-up study, Haaf (1984) communicates preliminary test results from the Manzanares pilot plant, with findings corresponding well with model calculations.

Figure 1.2: The prototype solar tower power plant in Manzanares, Spain

Mullett (1987) presents an analysis for determining the overall efficiency of a solar tower power plant. He concludes that a solar tower has a low overall efficiency, making a large scale project the only economically viable option.

Specific work was done by Padki *&* Sherif (1988) on the tower, investigating the effects of various geometrical configurations on tower performance and efficiency.

In 1991, Schlaich (1991) calls for urgent reaction to the world's growing problems of energy demand, population explosion and pollution through the use of large scale solar energy utilization.

In his book, Schlaich (1994) promotes the idea of using solar tower power plants for future electricity generation. Schlaich discusses the prototype solar tower in Manzanares, giving details concerning the construction, building materials used, operation, tests and experiments conducted and overall performance of the plant. Based on the experience gained at Manzanares, Schlaich presents rough investment and energy production cost calculations for developing large solar towers, having dimensions in the order of those shown in figure 1.1.

In a supplement to this book, water-filled black tubes are identified as a possible mechanism to increase the energy storage naturally.

Pasumarthi *&* Sherif (1998*a*) developed an approximate mathematical

model for a solar tower and in a following article (Pasumarthi and Sherif, 1998*b*) verified the model against experimental test results from a small scale solar tower model.

In a study by Kröger & Blaine (1999) on the driving potential for a solar tower, different theoretical models were evaluated and the influence of prevailing ambient conditions investigated. They find that moisture in the air generally enhances the potential and that under certain conditions condensation may occur in the tower.

With the goal of an advanced assessment of the performance of a solar tower's collector, Kröger & Buys (1999) develop analytical relations for determining the pressure differential due to frictional effects, and heat transfer coefficient, for developing radial flow between two essentially parallel discs.

In his paper on tension structures, Schlaich (1999) briefly discusses the performance, construction methods and cost of various solar energy generation schemes. Schlaich presents the idea of placing stiffening spoked wheels inside the tower to prevent deformation or buckling due to wind suction.

Hedderwick (2001) derived energy and draught equations that approximate the heat transfer and flow encountered in a solar tower power plant. A numerical model was also developed for the performance evaluation of a reference solar tower power plant (shown in figure 1.1).

Kröger & Buys (2001) developed relevant equations for a solar tower power plant.

Following a somewhat different approach, Von Backström & Gannon (2000*b*) regard the solar tower power plant as an air standard thermodynamic cycle and derive certain parameter relationships.

More recently, Gannon (2002) and Gannon & Von Backström (2003) investigated the performance of solar tower power plant turbines. Turbine design and layout suggestions are made, while an experimental model is used to predict turbine performance and efficiency.

Bernardes *et al.* (2003) present a thermal and technical analysis of a solar tower power plant. An analytical and numerical model is developed and simulation results are compared with experimental results from the Manzanares pilot plant. Simulation results are also presented which predict the performance characteristics for large-scale plants.

1.2 Objectives

The main objective of this thesis is to evaluate the performance of a solar tower power plant. The work builds on previous studies, with the aim of gaining a better understanding of the operation and performance of large-scale solar tower power plants.

Some of the major goals of this study include:

- The derivation of the relevant equations,
- The simplification of the relevant equations,
- The derivation and implementation of accurate discretization schemes,
- The development of a sound and user-friendly computer simulation model that is able to evaluate various solar tower power plant configurations at any global location and requiring less computation time than previous models,
- The incorporation into the model of factors such as wind effects, tower shadow effects and property changes across the turbine.

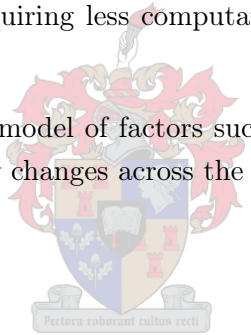

Pectora roborant cultus recti

Chapter 2

Discretization of Conservation Equations

In Appendix A, relevant conservation equations are derived for the collector and tower of the solar tower power plant. This chapter expands on the terms in these equations as well as discretizing the equations for their ultimate use in the numerical model with which the plant performance is evaluated.

2.1 Derived conservation equations

The relevant conservation equations for the solar tower power plant, as derived in Appendix A, is presented here in its final form before discretization for convenience.

2.1.1 Collector

Continuity equation

$$\frac{1}{r}\frac{\partial}{\partial r}\left(\rho v r H\right) = 0 \tag{2.1}$$

Momentum equation

$$-\left(H\frac{\partial p}{\partial r} + \tau_r + \tau_g + \frac{F_{\text{supports}}}{r\Delta\theta}\right) = \rho v H\frac{\partial v}{\partial r} \tag{2.2}$$

Roof energy equation

$$\alpha_{eb}I_{hb} + \alpha_{ed}I_{hd} + q_{gr} = q_{ra} + q_{rs} + q_{rh} \tag{2.3}$$

Ground energy equation

At z = 0 (Ground surface)

$$(\tau_e \alpha_g)_b \, I_{hb} + (\tau_e \alpha_g)_d \, I_{hd} = q_{gr} - k_g \left. \frac{\partial T_g}{\partial z} \right|_{z=0} + q_{gh} \tag{2.4}$$

At z > 0

$$- k_g \frac{\partial^2 T_g}{\partial z^2} + \rho_g c_{pg} \frac{\partial T_g}{\partial t} = 0 \tag{2.5}$$

At z = ∞

$$\frac{\partial T_g}{\partial z} = 0 \tag{2.6}$$

Air energy equation

$$q_{rh} + q_{gh} = \rho v H \frac{\partial}{\partial r} \left(c_p T \right) \tag{2.7}$$

2.1.2 Tower

Continuity equation

$$\frac{\partial}{\partial z} \left(\rho_t v_t \right) = 0 \tag{2.8}$$

Momentum equation

$$- \frac{\partial p_t}{\partial z} - \left(\frac{\tau_t \, \pi \, d_t + F_{bw}}{A_t} \right) = \rho_t \left(g + v_t \frac{\partial v_t}{\partial z} \right) \tag{2.9}$$

Energy equation

$$\rho_t v_t \frac{\partial}{\partial z} \left(c_{pt} T_t \right) + \frac{\partial}{\partial z} \left(\rho_t v_t \, g \, z \right) = 0 \tag{2.10}$$

2.2 Collector discretization schemes

When discretizing equations, a certain control volume convention must be defined. The finite difference grid used for the discretization of the collector conservation equations is shown in figure 2.1. The figure clearly shows how the collector roof, collector air and ground control volumes are defined for the evaluation of the solar tower power plant collector.

The subscript i denotes the radial node position in the collector, starting from the outer boundary of the collector and moving towards the tower. Furthermore, the subscript k represents the node position in the ground under the collector, starting from the ground surface and moving deeper into the ground.

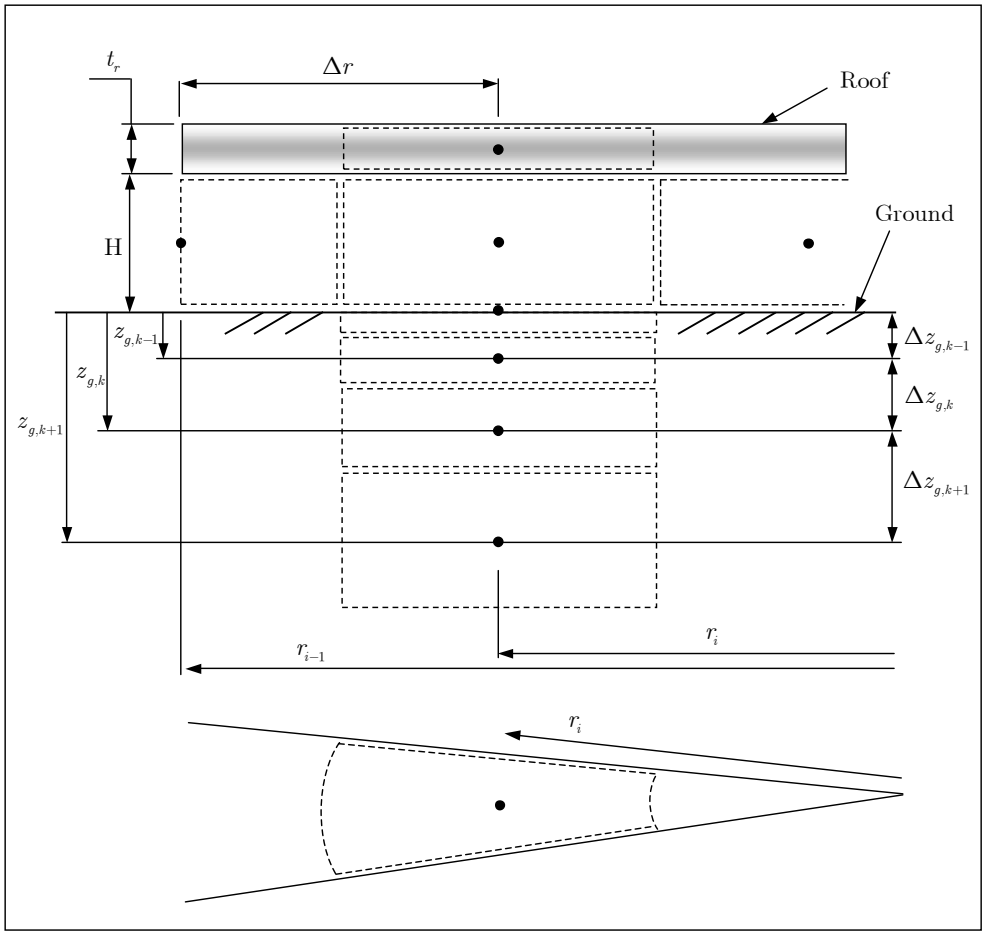

Figure 2.1: Collector finite difference grid

2.2.1 Collector air scheme

At first, a simple backward difference discretization scheme was used to discretize the continuity, momentum and air energy equations of the collector. This scheme approximates the gradient at a node by a finite difference between the specific node and the adjacent upwind node, as shown in equation (2.11). No time derivatives are necessary due to the steady state assumption

(this statement will be elaborated on in due course) employed for all air flow equations in the solar tower power plant model.

$$\left(\frac{\partial \phi}{\partial r}\right)\bigg|_i = \frac{\phi_{i-1} - \phi_i}{\Delta r} + O(\Delta r) \tag{2.11}$$

Through personal communication, Buys (2003-2004) suggested using a slightly different, more accurate discretization scheme. This scheme, described by equation (2.12), approximates the gradient at a node by the finite difference between the specific node and the two previous upwind nodes. The derivation of this discretization scheme is performed in Appendix D of this document.

$$\left(\frac{\partial \phi}{\partial r}\right)\bigg|_i = \frac{-3\phi_i + 4\phi_{i-1} - \phi_{i-2}}{2\Delta r} + O(\Delta r^2) \tag{2.12}$$

It should be noted that this scheme can only be introduced at the third node of the grid, due to its value depending on the previous two nodes.

Thus, it was decided to use the simple backward difference scheme (described by equation (2.11)) when stepping from the first to the second radial node in the collector, and then applying the more accurate difference scheme (from equation (2.12)) for the remainder of the collector nodes.

2.2.2 Collector ground scheme

At first attempt, an implicit Crank-Nicolson scheme was developed (for a grid with varying control volume thicknesses, not shown here) for the ground control volumes. This scheme approximates the gradient at a node by taking the average of the current and old values of the finite difference between the specific node and the two adjacent nodes, as indicated by equation (2.14). For

$$\frac{\partial \phi}{\partial t} = \frac{\partial^2 \phi}{\partial z^2} \tag{2.13}$$

the Crank-Nicolson method is

$$\frac{\phi_k - {\phi_k}^{old}}{\Delta t} = \frac{1}{2}\left[\frac{\phi_{k+1} - 2\phi_k + \phi_{k-1}}{\Delta z^2} + \frac{{\phi_{k+1}}^{old} - 2{\phi_k}^{old} + {\phi_{k-1}}^{old}}{\Delta z^2}\right] \tag{2.14}$$

Through personal communication, Buys (2003-2004) again suggested using a more accurate discretization scheme. This scheme, derived by Buys (2003-

2004), is basically a modified version of the Crank-Nicolson method and is described by equation (2.15). The derivation of this discretization scheme is performed in Appendix D of this document. Equation (2.13) is discretized by this method in the following way

$$a_k\,\phi_{k-1} + b_k\,\phi_k + c_k\,\phi_{k+1} = {a_k}^*{\phi_{k-1}}^{old} + {b_k}^*{\phi_k}^{old} + {c_k}^*{\phi_{k+1}}^{old} \tag{2.15}$$

where a_k, b_k, c_k, ${a_k}^*$, ${b_k}^*$ and ${c_k}^*$ are coefficients as defined in Appendix D.

2.3 Collector continuity equation

From the partial differential equation (A.4), the collector continuity equation is discretized according to the simple backward difference method in the following way

$$\frac{1}{r_i}\,\frac{(\rho v r H)_{i-1} - (\rho v r H)_i}{\Delta r} = 0 \tag{2.16}$$

which can be simplified to yield for the velocity at node i

$$v_i = \frac{(\rho v r H)_{i-1}}{(\rho\, r H)_i} \tag{2.17}$$

for $i = 1$, where N is the total number of collector control volumes.

Equation (A.4) is also discretized according to the method suggested by Buys (2003-2004) as follows:

$$\frac{1}{r_i}\,\frac{-3(\rho v r H)_i + 4(\rho v r H)_{i-1} - (\rho v r H)_{i-2}}{2\Delta r} = 0 \tag{2.18}$$

which can again be simplified to give for the velocity at node i

$$v_i = \frac{4(\rho v r H)_{i-1} - (\rho v r H)_{i-2}}{3(\rho\, r H)_i} \tag{2.19}$$

for $i = 2, 3, ...N$.

Equations (2.17) and (2.19) are the discretized equations used in the numerical model of the solar tower power plant to solve for the air velocity in the collector.

2.4 Collector momentum equation

The following section expands on the terms of the partial differential momentum equation (A.17), as derived in Appendix A. The collector momentum equation is then discretized according to the schemes discussed at the beginning of this chapter.

It is assumed that the air flow in the collector is turbulent, fully developed and can be approximated as flow between parallel plates.

2.4.1 Collector roof shear stress

In their paper, Kröger & Buys (1999) develop a relation for the shear stress due to radial flow over smooth surfaces. With the assumption that the collector roof may be regarded as a smooth surface ($\varepsilon \approx 0$), this relation is used to describe the shear stress on the collector roof due to the radial air flow in the collector

$$\tau_r = 0.023 \frac{\rho v^2}{Re^{0.2}} \tag{2.20}$$

where the Reynolds number is

$$Re = \frac{\rho v d_h}{\mu} \tag{2.21}$$

The hydraulic diameter (d_h) for flow between parallel plates is based on twice the distance between the plates, in this case $2H$. By substituting equation (2.21) into equation (2.20) and simplifying, we find

$$\tau_r = 0.02 \, \frac{\rho^{0.8} v^{1.8} \mu^{0.2}}{H^{0.2}} \tag{2.22}$$

2.4.2 Ground surface shear stress

In the same paper, Kröger & Buys (1999) develop an equation for the shear stress due to radial flow on rough surfaces. This equation is used to model the shear stress on the ground surface caused by the airflow in the collector

$$\tau_g = \frac{f \rho v^2}{2} \tag{2.23}$$

where the turbulent friction factor for rough surfaces, according to Kröger & Buys (1999), can be approximated by

$$f = 0.02975 \left(\frac{\varepsilon}{d_h}\right)^{0.254} \left[1.75 \left(\frac{\mu}{\rho v \varepsilon}\right)^{0.51} + 1\right] \tag{2.24}$$

Substitute equation (2.24) into equation (2.23) and find

$$\tau_g = 0.014875\, \rho v^2 \left(\frac{\varepsilon_g}{2H}\right)^{0.254} \left[1.75 \left(\frac{\mu}{\rho v \varepsilon_g}\right)^{0.51} + 1\right] \tag{2.25}$$

where ε_g is the roughness of the ground surface.

The specific composition of the ground surface is as yet unknown. The proposed site for a solar tower power plant is a hot, sunny location, for instance a desert area. Kröger (2004) lists some roughness lengths for various types of vegetation and natural surfaces. Table 2.1 gives an extract of the most relevant values by Kröger (2004).

Table 2.1: Extract of some natural surface roughness lengths by Kröger (2004)

Surface Configuration	*Roughness* [m]
Uncut grass	0.07
Crop stubble	0.02
Short grass	0.002
Bare sand	0.0004

In a paper regarding a solar tower power plant, Kröger & Buys (2001) assume a granite ground surface in the collector with a roughness of $\varepsilon_g = 0.05$ m.

2.4.3 Collector roof supports

As the air flows under the collector roof towards the tower, the collector roof supports exert a drag force on the air. Figure 2.2 gives a schematic illustration of the spacing convention used when calculating this drag force.
The drag force exerted on the air by each of the supports are

$$F_{sD} = C_{sD} \frac{1}{2} \rho v^2 H d_s \tag{2.26}$$

where C_{sD} is the support drag coefficient (based on the frontal support area), ρ is the air density, v is the local free stream velocity, H is the height of the collector roof (hence the height of the support) and d_s is the support diameter.

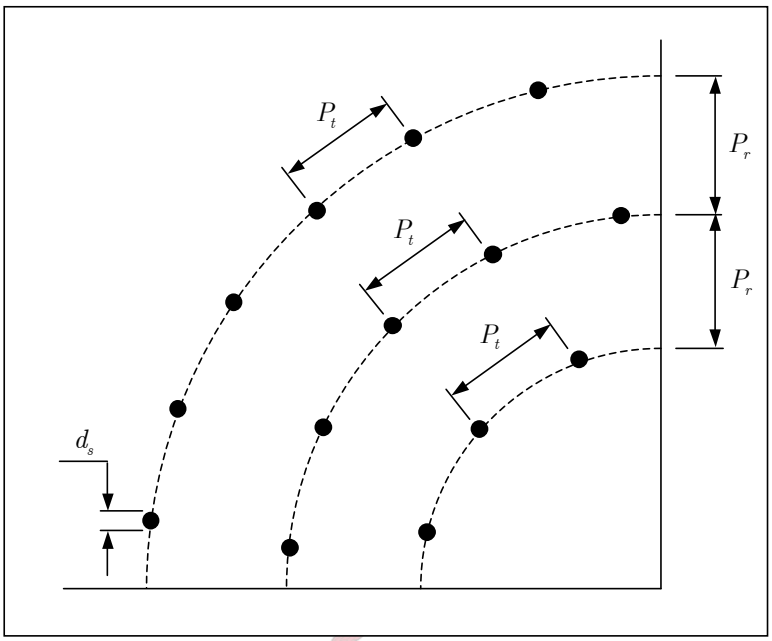

Figure 2.2: Schematic plan view of a segment of the collector roof, showing the position of the supports

Both White (1999) and Kröger (2004) give values for C_{sD} of between 1 and 1.2 for $10^4 < Re < 2 \times 10^5$. For $Re > 2 \times 10^5$, the drag coefficient decreases to a value between 0 and 1. Due to changing mass flow rates (and therefore changing Reynolds numbers) in the collector, there exists some uncertainty in specifying an accurate value for C_{sD}. Kröger & Buys (2001) specify a relatively conservative supports drag coefficient value of $C_{sD} = 1$.

The number of supports at a specific collector radius may be calculated by

$$n_r = \frac{2\pi r}{P_t} \tag{2.27}$$

where n_r, r and P_t are the number of supports, the specific radius where the supports are located and the tangential pitch between the supports (see figure 2.2) respectively.

The collector roof supports should be optimized to provide maximum structural stability, while enforcing a minimum drag force on the flow of air in the collector. Hedderwick (2001) as well as Kröger & Buys (2001) assume cylindrical supports with a diameter of $d_s = 0.15$ m. They also suggest a supports positioning configuration shown in figure 2.2, with both a tangential and radial pitch of 10 m.

The drag force enforced on the air by all the supports at a specific collector radius is given by

$$F_{srD} = n_r F_{sD} = \frac{C_{sD}\,\rho v^2 H d_s \pi r}{P_t} \tag{2.28}$$

where the free stream velocity is

$$v = \frac{\dot{m}}{\rho(2\pi r H)} \tag{2.29}$$

where $\dot{m}$ is the mass flow of the air in the collector.

The height of the collector roof at a specific radius may be found using the following relation

$$H = H_2 \left(\frac{r_2}{r}\right)^b \tag{2.30}$$

where H_2 is the height of the collector roof (see figure 1.1) at the collector perimeter radius, r_2, while b is an exponent.

Both Hedderwick (2001) and Kröger & Buys (2001) produce annual power output results for a reference plant with a perimeter collector radius of $r_2 =$ 2000 m at a perimeter height of $H_2 =$ 10 m, with a collector roof shape coefficient of $b = 0.5$. Kröger & Buys (2001) also state that the output of the plant can be increased by changing the shape of the collector roof and perimeter height. Their results give a maximum power output with $b = 1$ and $H_2 =$ 3.3 m. They also find that increasing the collector area increases the power output.

When substituting equations (2.30) and (2.29) into equation (2.28) and simplifying, we find

$$F_{srD} = \frac{C_{sD}\,\dot{m}^2 d_s\, r^{b-1}}{4\pi\rho P_t H_2\, {r_2}^b} \tag{2.31}$$

For an annular control volume (360° control volume between two collector radii), the support drag force per unit radial length is calculated as follows

$$F_{supports} = \frac{\sum F_{srD}}{\Delta r} \tag{2.32}$$

where $\sum F_{srD}$ is the sum of all the support drag forces in the specific control volume.

Now, the partial differential momentum equation (A.17) is discretized according to the simple backward difference method and solved for the pressure at node i as follows

$$p_i = p_{i-1} - \left[(\rho v H)_i \frac{(v_i - v_{i-1})}{\Delta r} - \tau_{r,\,i} - \tau_{g,\,i} - \frac{F_{supports,\,i}}{r_i \Delta\theta}\right]\left(\frac{\Delta r}{H_i}\right) \tag{2.33}$$

for $i = 1$.

Discretizing equation (A.17) according to the method suggested by Buys (2003-2004) and solving for the pressure at node i gives

$$p_i = -\frac{1}{3}\left[(\rho v H)_i \left(\frac{3v_i - 4v_{i-1} + v_{i-2}}{2\Delta r}\right) - \tau_{r,\,i} - \tau_{g,\,i} - \frac{F_{supports,\,i}}{r_i \Delta\theta}\right]\left(\frac{2\Delta r}{H_i}\right) + \frac{4}{3}p_{i-1} - \frac{1}{3}p_{i-2} \tag{2.34}$$

for $i = 2, 3, ...N$.

Equations (2.33) and (2.34) are the discretized equations used in the numerical model of the solar tower power plant to solve for the air pressure in the collector.

2.5 Collector energy equations

The following section expands on the terms of the partial differential energy equations derived in Appendix A. These equations are then discretized according to the schemes discussed at the beginning of this chapter.

2.5.1 Collector roof

In this section, the terms of the collector roof energy equation (A.21), derived in Appendix A, are expanded and the equation is discretized.

2.5.1.1 Solar radiation

The solar radiation incident from the sun consists of two components, as discussed in Appendix E, namely beam and diffuse radiation. Therefore, the total solar radiation incident on a horizontal surface can be expressed as

$$I_h = I_{hb} + I_{hd} \tag{2.35}$$

In Appendix E, equation (E.6) defines the effective absorptivity of the collector roof. From this equation, the respective beam and diffuse effective absorptivities may be evaluated separately, as follows

$$\alpha_{eb} = \frac{1}{2}\left(\alpha_{\parallel,b} + \alpha_{\perp,b}\right) \tag{2.36}$$

for the beam radiation component and

$$\alpha_{ed} = \frac{1}{2}\left(\alpha_{\parallel,d} + \alpha_{\perp,d}\right) \tag{2.37}$$

for the diffuse radiation component, where the subscripts $\parallel$ and $\perp$ indicate the parallel and perpendicular polarization components. The variables $\alpha_{\parallel,b}$, $\alpha_{\perp,b}$, $\alpha_{\parallel,d}$ and $\alpha_{\perp,d}$ are evaluated according to equation (E.4), taking into consideration the polarization component (parallel or perpendicular) and the radiation component (beam or diffuse).

Furthermore from Appendix E, $\rho_{\parallel,b}$ and $\rho_{\parallel,d}$ are determined by equation (E.1), $\rho_{\perp,b}$ and $\rho_{\perp,d}$ are found using equation (E.2), while $\tau_{\alpha b}$ and $\tau_{\alpha d}$ are calculated using equation (E.8). It should be noted that the appropriate beam and diffuse incidence and refractive angles must be employed in the above mentioned equations.

2.5.1.2 Ground radiation

The radiation heat flux from the ground to the collector roof is given by

$$q_{gr} = F_{gr}\sigma({T_g}^4 - {T_r}^4) \tag{2.38}$$

where F_{gr} and σ are the radiation transfer factor and Boltzmann's constant respectively, while T_g and T_r are the ground surface and roof temperatures.

In order to determine a radiation transfer factor, it is assumed that the ground surface and collector roof may be approximated as two large parallel walls facing each other. From Mills (1995), the transfer factor in such a case is

$$F_{gr} = \frac{1}{\frac{1}{\epsilon_g} + \frac{1}{\epsilon_r} - 1} \tag{2.39}$$

where ϵ_g and ϵ_r represent the ground and roof emissivities respectively.

The specific emissivities for the ground and the collector roof is as yet unknown and must be chosen. Mills (1995) lists some radiative properties for various materials. An extract from this is given in table 2.2.

Table 2.2: Extract of some relevant emissivity values given by Mills (1995)

Material	*Emissvity*
Polished Glass	0.87 - 0.92
Pyrex Glass	0.8
Smooth Glass	0.91
Granite	0.44
Limestone	0.92
Sand	0.75
Soil	0.94

An extract is also presented in table 2.3 of radiative properties of some materials, as given by Modest (1993).

Table 2.3: Extract of some relevant emissivity values given by Modest (1993)

Material	*Emissvity*
Pyrex Glass	0.85 - 0.95
Smooth Glass	0.94
Sandstone	0.83 - 0.9

For their work on the collector, Kröger & Buys (2001) chose emissivity values of $\epsilon_g = 0.9$ and $\epsilon_r = 0.87$ for the ground and collector roof respectively.

By substituting equation (2.39) into equation (2.38) and factorizing, we find

$$q_{gr} = \left(\frac{1}{\frac{1}{\epsilon_g} + \frac{1}{\epsilon_r} - 1} \right) \sigma({T_g}^2 + {T_r}^2)(T_g + T_r)(T_g - T_r) \tag{2.40}$$

In order to linearize the energy equation that is to be discretized, a radiative heat transfer coefficient h_{gr} for heat transfer from the ground surface to the roof can be defined such that equation (2.40) may be written as

$$q_{gr} = h_{gr}(T_g - T_r) \tag{2.41}$$

where

$$h_{gr} = \left(\frac{1}{\frac{1}{\epsilon_g} + \frac{1}{\epsilon_r} - 1} \right) \sigma({T_g}^2 + {T_r}^2)(T_g + T_r) \tag{2.42}$$

2.5.1.3 Convection to ambient

The convection heat flux from the collector roof to the ambient air may be expressed as

$$q_{ra} = h_{ra}(T_r - T_a) \tag{2.43}$$

where h_{ra} is the convective heat transfer coefficient for heat transfer from the roof to the ambient air, while T_r and T_a are the roof and ambient temperatures respectively.

The convective heat transfer coefficient used in the present study is recommended by McAdams (1954), as follows:

$$h_{ra} = 5.7 + 3.8\, v_w \tag{2.44}$$

where v_w is the ambient wind velocity.

In very recent work done by Kröger (2001-2004), a possibly more reliable relation was developed for the convective heat transfer coefficient for a heated horizontal surface, facing upwards. By assuming that the collector roof may be approximated as a horizontal surface, it is possible to calculate h_{ra} by using equation (2.45)

$$h_{ra} = \frac{0.243 + 0.0015\, v_w \left[\frac{\rho T_m}{\mu g \Delta T} \right]^{1/3}}{\left[\frac{\mu T_m}{g \Delta T c_p\, k^2 \rho^2} \right]^{1/3}} \tag{2.45}$$

where T_m is the mean temperature between the roof and ambient air, g is the gravitational constant and ΔT is the difference between the roof and ambient air temperature. The variables ρ, μ, c_p and k are the density, dynamic viscosity, specific heat capacity and thermal conductivity of the air respectively, all calculated at the mean temperature.

Future studies should consider employing equation (2.45) rather than equation (2.44) for mixed convection calculations on a horizontal surface.

2.5.1.4 Radiation to sky

Energy is lost through radiation by the collector roof to the sky. This radiative heat flux is expressed as

$$q_{rs} = \epsilon_r \sigma ({T_r}^4 - {T_{sky}}^4) \tag{2.46}$$

where T_r is the roof temperature and T_{sky} the sky temperature. The sky temperature can be calculated using the following relation by Swinbank (1963)

$$T_{sky} = 0.0552\, {T_a}^{1.5} \tag{2.47}$$

Once again, in order to linearize the energy equation that is to be discretized, a radiative heat transfer coefficient h_{rs} for heat transfer from the roof to the sky can be defined such that equation (2.46) may be expressed as

$$q_{rs} = h_{rs}(T_r - T_{sky}) \tag{2.48}$$

where

$$h_{rs} = \epsilon_r \sigma ({T_r}^2 + {T_{sky}}^2)(T_r + T_{sky}) \tag{2.49}$$

2.5.1.5 Convection to air in collector

The convection heat flux from the collector roof to the air in the collector may be found using

$$q_{rh} = h_{rh}(T_r - T) \tag{2.50}$$

where h_{rh} is the convective heat transfer coefficient for heat transfer from the roof to the collector air, T_r the roof temperature and T the temperature of the air in the collector.

As mentioned previously, the collector roof is approximated to be a horizontal surface, while the flow in the collector is approximated as flow between parallel plates.

The convective heat transfer coefficient from the collector roof to the air in the collector is determined using Gnielinski's equation for turbulent flow

$$h_{rh} = \frac{(f/8)\,(Re - 1000)Pr}{1 + 12.7\,(f/8)^{1/2}\,(Pr^{2/3} - 1)} \left(\frac{k}{d_h}\right) \tag{2.51}$$

where f is the friction factor, Re is the Reynolds number, Pr is the Prandtl number and k is the thermal conductivity of the air. The Reynolds number is based on the hydraulic diameter ($d_h = 2\text{H}$) and all properties and the Prandtl number are evaluated at the mean air temperature.

Kröger (2004) states that for smooth surfaces the friction factor may be evaluated by

$$f = (1.82\, log_{10} Re - 1.64)^{-2} \tag{2.52}$$

where Re is the Reynolds number.

For rough surfaces, Haaland (1983) recommends the following equation

$$f = 0.3086 \left[log_{10} \left(\frac{6.9}{Re} + \left(\frac{\varepsilon/d_h}{3.75} \right)^{1.11} \right) \right]^{-2} \qquad for\ \varepsilon/d_h > 10^{-4} \tag{2.53}$$

where Re is again the Reynolds number and ε/d_h is the relative roughness of the surface, with d_h the hydraulic diameter.
Haaland (1983) also suggests

$$f = 2.7778 \left[log_{10} \left(\left(\frac{7.7}{Re} \right)^{3} + \left(\frac{\varepsilon/d_h}{3.75} \right)^{3.33} \right) \right]^{-2} \qquad for\ \varepsilon/d_h \leq 10^{-4} \tag{2.54}$$

for cases where ε/d_h is very small.

Discretizing and solving equation (A.21) for the roof temperature at node i, the collector roof energy equation may be written as

$$T_{r,\,i} = \frac{\alpha_{eb} I_{hb} + \alpha_{ed} I_{hd} + h_{gr} T_{g,1,\,i} + h_{ra} T_a + h_{rs} T_{sky} + h_{rh} T_i}{h_{ra} + h_{rs} + h_{rh} + h_{gr}} \tag{2.55}$$

where all the specified heat transfer coefficients and temperatures are the local values at node i. The subscript $(g, 1, i)$ refers to the ground surface temperature (node 1) at radial node i in the collector.

Equation (2.55) is therefore then the discretized equation used in the numerical model of the solar tower power plant to solve for the collector roof temperature.

2.5.2 Ground under collector

In the following section, the terms of the ground energy equations (A.24), (A.27) and (A.28), derived in Appendix A, are expanded and the equations discretized.

2.5.2.1 At z = 0 (Ground surface)

The first two terms of equation (A.24) may be evaluated by firstly determining the effective beam and diffuse transmissivities according to equation (E.5) in Appendix E, as follows

$$\tau_{eb} = \frac{1}{2}\left(\tau_{\parallel,\,b} + \tau_{\perp,\,b}\right) \tag{2.56}$$

for the beam radiation component and

$$\tau_{ed} = \frac{1}{2}\left(\tau_{\parallel,\,d} + \tau_{\perp,\,d}\right) \tag{2.57}$$

for the diffuse radiation component. The variables $\tau_{\parallel,\,b}$, $\tau_{\perp,\,b}$, $\tau_{\parallel,\,d}$ and $\tau_{\perp,\,d}$ are evaluated according to equation (E.3). For further calculation details, consult section 2.5.1.1 and Appendix E.

Secondly, the beam and diffuse transmittance-absorptance products are determined according to equation (E.9).

The terms I_{hb} and I_{hd} of equation (A.24) are the beam and diffuse solar radiation components on a horizontal surface, as discussed for the collector roof energy equation.

The radiation heat flux from the ground q_{gr} is similar to the term discussed in section 2.5.1.2. This term is also expanded as described by equations (2.38) to (2.42).

The convection heat flux from the ground surface to the air in the collector is given by

$$q_{gh} = h_{gh}(T_g - T) \tag{2.58}$$

where h_{gh} is the convective heat transfer coefficient for heat transfer from the ground surface to the collector air, T_g is the ground surface temperature and T the temperature of the air in the collector.

The ground surface is approximated to be a horizontal surface, while the flow in the collector is, as previously mentioned, approximated as flow between

parallel plates. When evaluating the convective heat transfer from the ground to the air in the collector, two cases must also be considered.

$T_g > T$

For a ground surface temperature greater than the temperature of the air in the collector, the ground surface may be approximated as a heated horizontal surface facing up. For this approximation, it is possible to calculate h_{gh} using (analogous to equation (2.45)) a very recent equation by Kröger (2001-2004)

$$h_{gh} = \frac{0.243 + 0.0015\, v_w \left[\frac{\rho T_m}{\mu g \Delta T}\right]^{1/3}}{\left[\frac{\mu T_m}{g \Delta T c_p\, k^2 \rho^2}\right]^{1/3}} \tag{2.59}$$

with T_m taken as the mean temperature between the ground surface and air in the collector and where ΔT is the difference between the ground surface temperature and the temperature of the collector air.

In the present study, however, the heat transfer coefficient h_{gh} is determined using Gnielinski's equation, analogous to equation (2.51)

$$h_{gh} = \frac{(f/8)\,(Re - 1000)Pr}{1 + 12.7\,(f/8)^{1/2}\,(Pr^{2/3} - 1)} \left(\frac{k}{d_h}\right) \tag{2.60}$$

An assumption is made that the ground surface will have a roughness value. The friction factor f in equation (2.60) is therefore determined using either equation (2.53) or equation (2.54), as appropriate.

In future, is should be considered using equation (2.59) in combination with equation (2.60) for determining h_{gh}.

$T > T_g$

When the temperature of the air in the collector is greater than the ground surface temperature, the ground surface is approximated as a cooled horizontal surface, facing upwards. In this case we also use equation (2.60) to determine h_{gh}.

Rearrange equation (A.24) and discretize according to the scheme discussed in section 2.2.2 and find at a specific radial node i

$$- k_g \left[{\alpha_{-1}}^0 T_{g,0} + {\alpha_0}^0 T_{g,1} + {\alpha_1}^0 T_{g,2} + {\alpha_2}^0 T_{g,3} \right] = \alpha_g(\tau_{eb} I_{hb} + \tau_{ed} I_{ed}) - h_{gr}(T_{g,1} - T_r) - h_{gh}(T_{g,1} - T) \quad (2.61)$$

where α_g and k_g are the ground absorptivity and ground thermal conductivity respectively, while the various α coefficients are those defined in Appendix D. The subscript $(g, 0)$ (and zero superscripts on the α coefficients) indicate the "fictitious" node position, whereas the temperature subscripts 1, 2 and 3 represent the k^{th} node positions deeper into the ground (where 1 is the ground surface node).

Furthermore, it is assumed that the ground in the collector is a gray and diffuse surface. Therefore, the ground absorptivity will be independent of direction and have the same value as its emissivity ($\alpha_g = \epsilon_g$).

Mills (1995) gives some thermal properties of various materials. A small extract from this is presented in table 2.4.

Table 2.4: Extract of some relevant thermal conductivity values listed in Mills (1995)

Material	*Thermal Conductivity* [W/mK]
Dry Soil	1.0
Wet Soil	2.0

Kröger & Buys (2001) chose a value for the ground (granite) thermal conductivity of $k_g = 1.73$.

2.5.2.2 At z > 0

Equation (A.27), the ground energy equation for the control volumes beneath the ground surface, is discretized in accordance with the scheme considered in section 2.2.2. Thus, we find at each radial node i

$$a_k T_{g,k-1} + b_k T_{g,k} + c_k T_{g,k+1} = {a_k}^* {T_{g,k-1}}^{old} + {b_k}^* {T_{g,k}}^{old} + {c_k}^* {T_{g,k+1}}^{old} \quad (2.62)$$

for $k = 1, 2, ...N$, where a_k, b_k, c_k, ${a_k}^*$, ${b_k}^*$ and ${c_k}^*$ are coefficients as defined in Appendix D. The k subscripts indicate the node position in the ground,

whereas the superscript *old* represents the ground temperature value of the previous time step.

2.5.2.3 At z = ∞

The energy equation (A.28) for the deepest ground control volume is discretized as follows:

$$\alpha_{-2}{}^{N+1} T_{N-2} + \alpha_{-1}{}^{N+1} T_{N-1} + \alpha_0{}^{N+1} T_N + \alpha_1{}^{N+1} T_{N+1} = 0 \qquad (2.63)$$

where once again the various α coefficients are those defined in Appendix D. The $N+1$ subscript (and superscripts on the α coefficients) indicate the other "fictitious" node position, whereas the subscripts $N-2$, $N-1$ and N represent the k^{th} node positions deeper into the ground (where N is the number of the deepest node in the ground).

Therefore, equations (2.61), (2.62) and (2.63) are the discretized equations used in the numerical model of the solar tower power plant to solve for the ground temperatures, at various depths, in the collector.

2.5.3 Air stream in the collector

In the following section, the terms of the air stream energy equation (A.35), as derived in Appendix A, are expanded and the equation is discretized.

The convection heat fluxes from the roof (q_{rh}) and ground (q_{gh}) to the air in the collector are the same terms used in the collector roof and ground surface energy equations. These heat fluxes are expressed by equations (2.50) and (2.58) respectively. The heat transfer coefficients h_{rh} and h_{gh} are also evaluated in the same manner as discussed previously in this chapter.

Discretizing equation (A.35) according to the simple backward difference method and solving for the air temperature in the collector at node i gives

$$T_i = \frac{\frac{(\rho v H)_i (c_p T)_{i-1}}{\Delta r} - h_{rh} T_{r,i} - h_{gh} T_{g,1,i}}{\frac{(\rho v H c_p)_i}{\Delta r} - h_{rh} - h_{gh}} \qquad (2.64)$$

for $i = 1$.

All the specified heat transfer coefficients are the local values at node i. As mentioned before, the subscript $(g, 1, i)$ refers to the ground surface temperature (node 1) at radial node i in the collector.

Discretize equation (A.35) according to the method suggested by Buys (2003-2004) and solve for the collector air temperature at node i and find

$$T_i = \frac{\frac{(\rho v H)_i}{2\Delta r}\left[4(c_p T)_{i-1} - (c_p T)_{i-2}\right] - h_{rh} T_{r,\,i} - h_{gh} T_{g,\,1,\,i}}{\frac{3(\rho v H c_p)_i}{2\Delta r} - h_{rh} - h_{gh}} \tag{2.65}$$

for $i = 2, 3, ...N$.

The discretized equations (2.64) and (2.65) are used in the numerical model of the solar tower power plant to solve for the air temperatures in the collector.

2.6 Tower discretization schemes

Figure 2.3 shows the finite difference grid used for the discretization of the tower conservation equations.

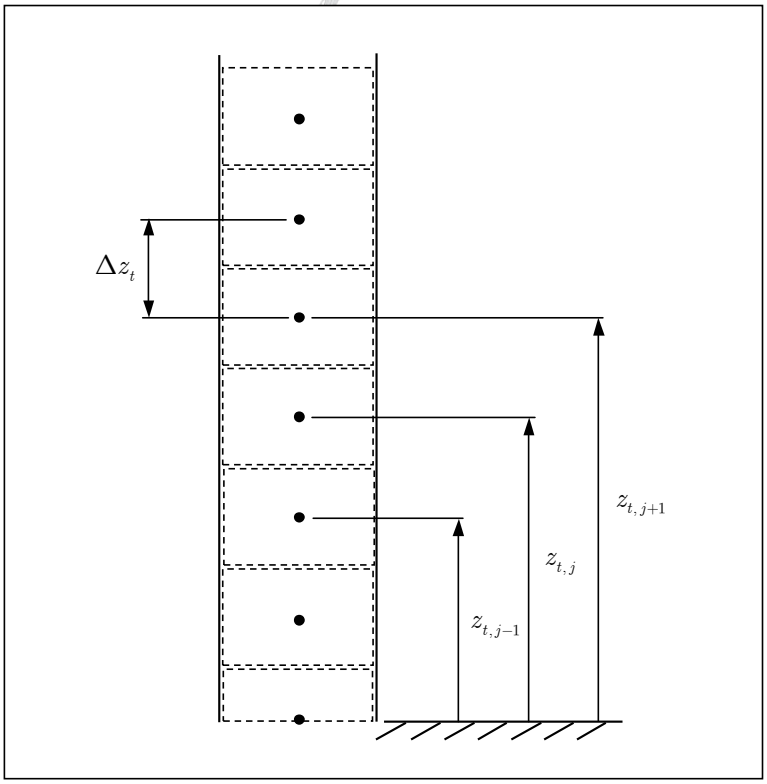

Figure 2.3: Tower finite difference grid

It should be noted that two approximations are made for the tower and the position of the turbine in the tower. It is approximated that the tower starts at ground level and that the turbine is located before the ground level node of the tower. The subscript j, as in figure 2.3, denotes the axial node position inside the tower, starting from ground level up to the height of the tower.

As with the collector, at first a simple backward difference discretization scheme was used to discretize the continuity, momentum and air energy equations of the tower. This scheme is similar to equation (2.11) and is described by equation (2.66). Once again, no time derivatives are necessary due to the steady state assumption employed for all air flow equations in the solar tower power plant model.

$$\left(\frac{\partial \phi}{\partial z}\right)\bigg|_j = \frac{\phi_j - \phi_{j-1}}{\Delta z} + O(\Delta z) \tag{2.66}$$

Buys (2003-2004) also suggested using a different, more accurate discretization scheme for use in the tower. This scheme for the tower, analogous to equation (2.12), is derived in Appendix D and is given by equation (2.67).

$$\left(\frac{\partial \phi}{\partial z}\right)\bigg|_j = \frac{3\phi_j - 4\phi_{j-1} + \phi_{j-2}}{2\,\Delta z} + O(\Delta z^2) \tag{2.67}$$

As for the collector, this scheme can only be introduced at the third node of the grid due to its value depending on the previous two nodes.

Thus, it was decided to use the simple backward difference scheme (described by equation (2.66)) when stepping from the first to the second axial node in the tower, and then applying the more accurate difference scheme (from equation (2.67)) for the remainder of the tower nodes.

2.7 Tower continuity equation

The partial differential tower continuity equation (A.39) is discretized according to the simple backward difference method in the following way

$$\frac{(\rho_t v_t)_j - (\rho_t v_t)_{j-1}}{\Delta z_t} = 0 \tag{2.68}$$

which can be simplified to yield for the velocity in the tower at node j

$$v_{t,\,j} = \frac{(\rho_t v_t)_{j-1}}{\rho_{t,\,j}} \tag{2.69}$$

for $j = 1$, where N is the total number of tower control volumes.

Discretize equation (A.39) according to the method suggested by Buys (2003-2004) and find

$$\frac{3(\rho_t v_t)_j - 4(\rho_t v_t)_{j-1} + (\rho_t v_t)_{j-2}}{2\,\Delta z_t} = 0 \tag{2.70}$$

which can again be simplified to give for the tower velocity at node j

$$v_{t,\,j} = \frac{4(\rho_t v_t)_{j-1} - (\rho_t v_t)_{j-2}}{3\rho_{t,\,j}} \tag{2.71}$$

for $j = 2, 3, ...N$.

Equations (2.69) and (2.71) are the discretized equations used in the numerical model of the solar tower power plant to solve for the air velocity in the tower.

2.8 Tower momentum equation

The following section expands on the terms of the partial differential tower momentum equation (A.47), as derived in Appendix A. The tower momentum equation is then discretized according to the schemes discussed in section 2.6.

The air flow in the tower is assumed turbulent, fully developed and can be approximated as flow in a pipe. It is also assumed that the inside tower wall will have some roughness.

2.8.1 Tower wall shear stress

White (1999) states that the wall shear stress in a pipe may be calculated using

$$\tau_t = \frac{1}{8} f_t \rho_t {v_t}^2 \tag{2.72}$$

where ρ_t and v_t are the density and free stream velocity of the air in the tower respectively. The variable f_t is the friction factor of the tower wall and may be determined using equation (2.53) or equation (2.54), as appropriate. It is assumed that the tower will be constructed from concrete, and that the inside tower wall will therefore be a concrete surface. An extract of a table from White (1999), listing some roughness lengths of selected materials, is presented in table 2.5.

Table 2.5: Extract of some relevant roughness values given by White (1999)

Surface	*Roughness* [m]
Smoothed Concrete	0.00004
Rough Concrete	0.002

Kröger & Buys (2001) selected a roughness length of $\varepsilon_t = 0.002$ m for the inside surface of the tower.
The Reynolds number used in the tower calculations is given by

$$Re_t = \frac{\rho_t v_t d_t}{\mu_t} \tag{2.73}$$

where the subscript t indicates the air properties in the tower and d_t is the inside tower diameter.

2.8.2 Bracing wheel drag force

The structure of the tower is reinforced internally using evenly spaced spoked bracing wheels, as first proposed by Schlaich (1999). These bracing wheels exert a drag force on the upward flowing air in the tower. The total bracing wheel drag force per unit tower height, based on the tower inlet dynamic pressure, is given by

$$F_{bw} = \frac{(A_t K_{bw} \frac{1}{2} \rho_{ti} {v_{ti}}^2)(n_{bw})}{H_t} \tag{2.74}$$

where A_t, H_t and n_{bw} is the tower cross-sectional area, the tower height and the number of bracing wheels respectively, while K_{bw} is the bracing wheel pressure loss coefficient.

Experimental results found by Von Backström *et al.* (2003) state that a very conservative value for the bracing wheel pressure loss coefficient will be in the order of $K_{bw} = 0.1$ per bracing wheel. The publication goes on to suggest that streamlining the bracing wheel structure may reduce this value to $K_{bw} = 0.01$. Furthermore, Kröger & Buys (2001) also select a pressure loss coefficient for an internal tower supporting structure (based on a tower with 10 bracing wheels) of $K_{bw} = 0.1$. The calculations by Von Backström *et al.* (2003) and Kröger & Buys (2001) are based on a reference plant with a 1500 m high tower with an inside diameter of $d_t = 160$ m.

This study assumes a streamlined bracing wheel structure with 10 bracing wheels, with a bracing wheel pressure loss coefficient of $K_{bw} = 0.01$ per bracing wheel.

The partial differential tower momentum equation (A.47) is discretized according to the simple backward difference method and solved for the pressure in the tower at node j

$$p_{t,j} = -\left[\left(\frac{\tau_t \pi d_t + F_{bw}}{A_t}\right) + \rho_{t,j}\left[g + v_{t,j}\left(\frac{v_{t,j} - v_{t,j-1}}{\Delta z_t}\right)\right]\right]\Delta z_t + p_{t,j-1} \tag{2.75}$$

for $j = 1$.

Discretize equation (A.47) according to the method suggested by Buys (2003-2004) and solve for the pressure in the tower at node j and find

$$p_{t,j} = -\frac{2}{3}\left[\rho_{t,j}\left[g + v_{t,j}\left(\frac{3v_{t,j} - 4v_{t,j-1} + v_{t,j-2}}{2\Delta z_t}\right)\right] + \left(\frac{\tau_t \pi d_t + F_{bw}}{A_t}\right)\right]\Delta z_t + \frac{4}{3}p_{t,j-1} - \frac{1}{3}p_{t,j-2} \tag{2.76}$$

for $j = 2, 3, ...N$.

Therefore, equations (2.75) and (2.76) are the discretized equations used in the numerical model of the solar tower power plant to solve for the air pressure in the tower.

2.9 Tower energy equation

In this section, the partial differential tower energy equation (A.54) is discretized in accordance with the schemes previously discussed.

Discretizing using the simple backward difference method and solving for the air temperature in the tower at node j gives

$$T_{t,j} = \frac{\rho_{t,j}\, v_{t,j}(c_{pt}T_t)_{j-1} + (\rho_t v_t\, g z_t)_{j-1} - (\rho_t v_t\, g z_t)_j}{(\rho_t v_t c_{pt})_j} \tag{2.77}$$

for $j = 1$.

When discretizing equation (A.54) according to the method suggested by Buys (2003-2004) and solving for the air temperature in the tower at node j,

we find

$$T_{t,\,j} = \frac{-3(\rho_t v_t\, g z_t)_j + 4(\rho_t v_t\, g z_t)_{j-1} - (\rho_t v_t\, g z_t)_{j-2}}{3(\rho_t v_t c_{pt})_j} + \frac{4(c_{pt} T_t)_{j-1}}{3\, c_{pt,\,j}} - \frac{(c_{pt} T_t)_{j-2}}{3\, c_{pt,\,j}} \tag{2.78}$$

for $j = 2, 3, ...N$.

Equations (2.77) and (2.78) are the discretized equations used in the numerical model of the solar tower power plant to solve for the air temperature in the tower.

Pectora roborant cultus recti

Chapter 3

The Draught Equation

The draught equation calculates the available pressure differential that can be used to drive the turbine by subtracting the various system pressure drops from the driving potential pressure. The following chapter expands on the terms in the draught equation.

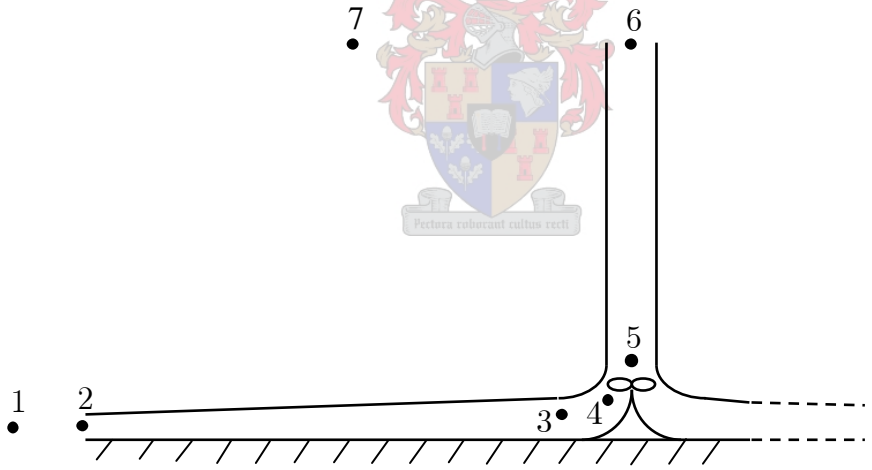

Figure 3.1: Schematic of the solar tower power plant

3.1 Pressure drop across the turbine

The ultimate goal of the draught equation is to determine the pressure drop across the turbine. Using this pressure drop, the power generated by the turbine may be calculated.

The pressure drop across the turbine is calculated as follows:

$$\Delta p_{turb} = \Delta p - (\Delta p_i + \Delta p_{coll} + \Delta p_{turb,\,i} + \Delta p_t + \Delta p_{to} + \Delta p_{dyn}) \tag{3.1}$$

where Δp, Δp_i and Δp_{coll} are the driving potential, the collector inlet pressure drop and the total pressure drop through the collector respectively. The terms $\Delta p_{turb,\,i}$, Δp_t and Δp_{to} represent the turbine inlet pressure drop, the total pressure drop through the tower and the tower outlet pressure differential, while Δp_{dyn} is the tower dynamic outlet loss.

3.2 Power output

The flow of air through the tower of the solar tower power plant drives a turbine at the base of the tower. The turbine drives a generator which generates electricity. The power generated by the turbine may be determined by

$$P = \eta_{tg}\, \Delta p_{turb} V_{avg} \tag{3.2}$$

where η_{tg} is the turbo-generator efficiency and V_{avg} is the average volume flow rate through the turbine which may also be expressed as

$$V_{avg} = \frac{\dot{m}}{\rho_{avg}} \tag{3.3}$$

where ρ_{avg} is the average density through the turbine. The air is assumed to be an ideal gas and the average density is calculated by (from figure 3.1)

$$\rho_{avg} = \frac{p_{avg}}{R\,T_{avg}} = \frac{\frac{1}{2}\,(p_4 + p_5)}{\frac{1}{2} R\,(T_4 + T_5)} \tag{3.4}$$

where the subscript avg indicates the average values through the turbine.

Gannon & von Backström (2000) prescribe a total-to-total turbine efficiency of 80% for their simulation of a large scale solar tower power plant. Experimental results by Gannon & Von Backström (2003) predict a total-to-total turbine efficiency of 85 - 90% for a model solar tower power plant axial turbine. Kröger & Buys (2001) specify a turbo-generator efficiency (combined efficiency of turbine and generator) of 80% for their work in determining an annual power output for a solar tower power plant.

3.3 System pressure drop

3.3.1 Collector inlet pressure drop

From figure 3.1, as the air moves into the collector from an essentially stagnant condition at 1, it experiences a pressure drop at the inlet of the collector. From Kröger (2004), an inlet loss coefficient K_i is defined as

$$K_i = \frac{(p_{t,1} - p_{t,2})}{\frac{1}{2}\rho v^2} \tag{3.5}$$

where $p_{t,1}$ and $p_{t,2}$ are the total pressures at sections 1 and 2.

From figure 3.1, for the stagnant ambient air at 1, $p_{t,1} = p_a = p_1$, while the total pressure at 2 can be written as

$$p_{t,2} = p_2 + \frac{1}{2}\rho_2 {v_2}^2 \tag{3.6}$$

When substituting equation (3.6) into equation (3.5) and rearranging, we find

$$p_1 - \left(p_2 - \frac{1}{2}\rho_2 {v_2}^2\right) = K_i \frac{1}{2}\rho_2 {v_2}^2 \tag{3.7}$$

Therefore the collector inlet pressure drop is given by

$$\Delta p_i = (p_1 - p_2) = K_i \frac{1}{2}\rho_2 {v_2}^2 + \frac{1}{2}\rho_2 {v_2}^2 \tag{3.8}$$

Both Hedderwick (2001) and Kröger & Buys (2001) employ a collector inlet loss coefficient of $K_i = 1$.

The effect of cross-winds on the inlet loss coefficient is assumed to be negligible.

3.3.2 Pressure drop in the collector

The accelerating radial airflow from the collector perimeter towards the tower will result in a pressure change in the collector (Δp_{coll}). Also, the roof and ground friction as well as the drag forces caused by the collector roof supports on the air flow will result in certain pressure drops.

The acceleration, friction and support pressure changes are all incorporated in the collector momentum equation, as derived in Appendix A. Thus the pressure drop over the collector radius is determined by calculating the

difference between the pressures given by the collector momentum equation (equations (2.33) and (2.34)) at the collector perimeter and collector outlet.

3.3.3 Turbine inlet loss

As the air flows from the collector outlet into the turbine inlet, it experiences an acceleration due to a decreasing flow area. The air flowing through the turbine inlet also experience a pressure drop. From figure 3.1, by once again employing equation (3.5), we find

$$K_{turb,\,i} = \frac{(p_{t,\,3} - p_{t,\,4})}{\frac{1}{2}\rho v^2} \tag{3.9}$$

where $K_{turb,\,i}$ is defined as the turbine inlet loss coefficient. Substituting for the total pressures at 3 and 4 and rearranging equation (3.9) gives

$$\left(p_3 + \frac{1}{2}\rho_3 {v_3}^2\right) - \left(p_4 + \frac{1}{2}\rho_4 {v_4}^2\right) = K_{turb,\,i}\frac{1}{2}\rho_4 {v_4}^2 \tag{3.10}$$

Therefore, the pressure drop over the turbine inlet can be expressed in terms of a turbine inlet loss coefficient as follows:

$$\Delta p_{turb,\,i} = (p_3 - p_4) = K_{turb,\,i}\frac{1}{2}\rho_4 {v_4}^2 + \frac{1}{2}\rho_4 {v_4}^2 - \frac{1}{2}\rho_3 {v_3}^2 \tag{3.11}$$

where the density and velocity at position 3 and 4 from figure 3.1 are used in the calculations.

In their paper on solar tower power plant towers (chimneys), Von Backström & Gannon (2000*a*) mention a typically expected turbine inlet loss coefficient of $K_{turb,\,i} = 0.25$. Kröger & Buys (2001) also specify a turbine inlet loss coefficient of $K_{turb,\,i} = 0.25$. Preliminary results from recent studies indicate that $K_{turb,\,i}$ is somewhat lower, with a value of between 0.15 and 0.1.

This study however assumes a conservative value for the turbine inlet loss coefficient of $K_{turb,\,i} = 0.25$.

3.3.4 Tower pressure drop

The accelerating axial airflow in the tower, the inside tower wall friction and the drag forces caused by the internal bracing wheel structures all contribute to a pressure drop over the height of the tower (Δp_t).

The above mentioned pressure changes are all incorporated in the tower momentum equation, as derived in Appendix A. Thus the pressure drop over the tower height is determined by calculating the difference between the pressures given by the tower momentum equation (equations (2.75) and (2.76)) at the tower inlet and tower outlet. It is important to note that the tower momentum equation contains a gravity force term, which must not be reckoned as a tower loss.

3.3.5 Tower outlet loss

The air exiting the tower experiences a pressure differential due to the shape of the tower outlet, and can be expressed as (from figure 3.1)

$$\Delta p_{to} = K_{to} \frac{1}{2} \rho_6 {v_6}^2 \tag{3.12}$$

where K_{to} is the tower outlet loss coefficient.

No-wind conditions

According to Kröger (2004), during relatively quiet (no significant ambient winds) periods, for a hyperbolic cooling tower with a cylindrical outlet where $0.5 \leq d_o/d_i \leq 0.85$, the tower outlet loss coefficient is given by

$$K_{to} = -0.28 {Fr_D}^{-1} + 0.04 {Fr_D}^{-1.5} \tag{3.13}$$

where d_o and d_i is the tower outlet and inlet diameter respectively, while Fr_D is the densimetric Froude number and is determined by

$$Fr_D = \left(\frac{\dot{m}}{A_6} \right)^2 / \left[\rho_6 (\rho_7 - \rho_6) g \, d_t \right] \tag{3.14}$$

The subscript 6 in equation (3.14) represents the tower outlet, while 7 indicates the ambient air condition at a position some distance from, but at the same height as the tower outlet (as shown in figure 3.1).

It is assumed that the solar tower power plant has a tower outlet to inlet diameter ratio of unity. Furthermore, it is assumed that equation (3.13) is applicable to the plant tower, although the tower has a diameter ratio larger than 0.85.

Wind effects

During windy ambient conditions, the tower outlet loss coefficient may be defined as follows:

$$K_{to} = \frac{\left(p_6 + \frac{1}{2}\rho_6 {v_6}^2\right) - \left(p_7 + \frac{1}{2}\rho_7 {v_7}^2\right)}{\frac{1}{2}\rho_6 {v_6}^2} = \frac{\Delta p_w}{\frac{1}{2}\rho_6 {v_6}^2} + 1 - \frac{\rho_7 {v_7}^2}{\rho_6 {v_6}^2} \tag{3.15}$$

where Δp_w is the static pressure difference in windy conditions. The velocity v_7 indicates the ambient wind velocity at the height of the tower (position 7 of figure 3.1), while v_6 is the velocity of the air in the tower exiting the tower at position 6.

A fluid flowing across a cylinder causes the static pressure to vary circumferentially around the cylinder. A static pressure coefficient which describes this variation may be defined as

$$C_p = \frac{(p_\theta - p_a)}{\frac{1}{2}\rho_a {v_a}^2} \tag{3.16}$$

where p_θ is the local static pressure and the subscript a refers to the ambient conditions far from the cylinder.

Buxmann (1983) performed model tests to evaluate the performance characteristics of cooling towers in the presence of wind. He defines an outlet pressure coefficient in terms of the static pressure difference between the throat of the tower and the ambient, as follows:

$$C_{po} = \frac{(\Delta p_w - \Delta p)}{\frac{1}{2}\rho_7 {v_7}^2} \tag{3.17}$$

where Δp_w is once again the static pressure difference in windy conditions and Δp is the static pressure difference during no-wind conditions. Equation (3.17) can be re-written as

$$C_{po} = \frac{\Delta p_w - (p_6 - p_7)}{\frac{1}{2}\rho_7 {v_7}^2} \tag{3.18}$$

In the case of no wind outside the tower, it is assumed that $p_6 \approx p_7$ and therefore equation (3.18) simplifies to

$$C_{po} = \frac{\Delta p_w}{\frac{1}{2}\rho_7 {v_7}^2} \tag{3.19}$$

Substitute equation (3.19) into equation (3.15) and find the tower outlet loss coefficient in windy conditions:

$$K_{to} = C_{po}\frac{\rho_7 {v_7}^2}{\rho_6 {v_6}^2} + 1 - \frac{\rho_7 {v_7}^2}{\rho_6 {v_6}^2} \tag{3.20}$$

According to Du Preez (1992), the pressure coefficient at the outlet of a cooling tower may be represented by the empirical relation:

$$\begin{aligned} C_{po} = & -0.405 + 1.07\left(\frac{v_7}{v_6}\right)^{-1} \\ & + 1.8\,log\left[\left(\frac{v_7}{2.7\,v_6}\right)\left(\frac{A_o}{A_t}\right)^{1.65}\right]\left[\left(\frac{v_7}{v_6}\right)\left(\frac{A_o}{A_t}\right)^{1.65}\right]^{-2} \\ & + \left[-1.04 + 1.702\left(\frac{A_o}{A_t}\right) - 0.662\left(\frac{A_o}{A_t}\right)^2\right]\left(\frac{v_7}{v_6}\right)^{-0.7} \end{aligned} \tag{3.21}$$

which is valid for $1.8 \leq (v_7/v_6) \leq 24$. The variables A_o and A_t represent the tower outlet and tower throat cross-sectional areas respectively.

It is assumed that the ratio of (A_o/A_t) for the tower of the solar tower power plant is unity.

3.3.6 Tower dynamic outlet loss

The air exiting the tower outlet experiences a loss in kinetic energy. This results in a dynamic pressure drop and is expressed as

$$\Delta p_{dyn} = \frac{1}{2}\alpha_e\,\rho_6 {v_6}^2 \tag{3.22}$$

where α_e is the kinetic energy correction factor and the subscript 6 once again represents the values at the tower outlet.

According to Du Preez *&* Kröger (1994), the velocity distribution at the outlet of a cooling tower is approximately uniform for $(1/Fr_D) \leq 3$, where Fr_D is given by equation (3.14). With the assumption that the outlet of the tower may be approximated as a cooling tower outlet and for typical Fr_D values greater than 2, α_e can be taken as unity.

Experimental results by Von Backström *et al.* (2003) indicate that α_e is greater than unity in cases where bracing wheels are located near the tower exit. However, α_e may be reduced by streamlining the bracing wheel structure.

This study assumes a streamlined bracing wheel structure and a kinetic energy correction factor of $\alpha_e = 1$.
Thus the dynamic tower outlet loss reduces to

$$\Delta p_{dyn} = \frac{1}{2}\,\rho_6 {v_6}^2 \tag{3.23}$$

3.4 Driving potential

The driving force or potential that causes air to flow through the solar tower power plant is due to a pressure difference between a column of cold air outside and a column of hot air inside the tower. From figure 3.1, the driving potential is given by

$$\Delta p = (p_1 - p_7) - (p_5 - p_6) \tag{3.24}$$

It is assumed that

$$p_6 \approx p_7 \tag{3.25}$$

Substituting equation (3.25) into equation (3.24) thus gives the drive potential as

$$\Delta p = (p_1 - p_5) \tag{3.26}$$

Assuming a dry adiabatic lapse rate (DALR) for the air outside and inside of the tower and assuming that the turbine is located at ground level, we find the following relations for pressure from Kröger (2004)

$$p_7 = p_1 \left(1 - 0.00975\,\frac{H_t}{T_1}\right)^{3.5} \tag{3.27}$$

and

$$p_6 = p_5 \left(1 - 0.00975\,\frac{H_t}{T_5}\right)^{3.5} \tag{3.28}$$

The paper by Von Backström (2003) confirms that the assumption of a dry adiabatic lapse rate for the solar tower power plant is reasonable. From equation (3.25), equating equations (3.27) and (3.28) and solving for p_5 gives

$$p_5 = \frac{p_1 \left(1 - 0.00975 \frac{H_t}{T_1}\right)^{3.5}}{\left(1 - 0.00975 \frac{H_t}{T_5}\right)^{3.5}} \tag{3.29}$$

When now substituting equation (3.29) into equation (3.26) and rearranging, we find

$$\Delta p = p_1 \left[1 - \left[\frac{\left(1 - 0.00975 \frac{H_t}{T_1}\right)}{\left(1 - 0.00975 \frac{H_t}{T_5}\right)}\right]^{3.5}\right] \tag{3.30}$$

3.5 Temperature drop across the turbine

The maximum power that may be extracted by the turbine is given by

$$P = \Delta p_{turb} V_{avg} \tag{3.31}$$

The maximum power extracted by the turbine can also be represented by

$$P = \dot{m}\, c_p\, \Delta T \tag{3.32}$$

By substituting equation (3.31) into equation (3.32), rearranging and assuming a constant mass flow rate and constant specific heat capacity over the turbine, the temperature drop across the turbine can be expressed as

$$\Delta T_{turb} = \frac{\Delta p_{turb} V_{avg}}{\dot{m}\, c_p} \tag{3.33}$$

Therefore, the turbine outlet temperature (from figure 3.1) is

$$T_5 = T_4 - \frac{\Delta p_{turb} V_{avg}}{\dot{m}\, c_p} \tag{3.34}$$

Pectora roborant cultus recti

Chapter 4

Implementation of the Numerical Model

A numerical model was developed to simulate the operation of a solar tower power plant. The main objective of the model is to ascertain the performance characteristics of such a plant.

The model was created in such a way as to accommodate varying plant specifications and global locations. This allows the user to investigate the effect of changing certain plant dimensions, variables or plant location on the performance of the solar tower power plant.

4.1 Model overview

The meteorological data for a specific location at a specific time step (as specified in Appendix C) is used as input to the numerical model. Then, starting from the collector perimeter and moving in towards the tower, the discretized collector conservation equations (given in chapter 2) are solved iteratively using the Gauss-Seidel method for each collector control volume. The various temperatures, pressure and air velocity are calculated at each node.

After taking the property changes caused by the turbine into account, we move up into the tower where the discretized tower conservation equations (given in chapter 2) are again solved iteratively using the Gauss-Seidel method for each tower control volume. The tower air temperature, pressure and air velocity are calculated at each node.

The power generated by the turbo-generator for the specific time step is calculated and if necessary, the collector inlet velocity (analogous to mass flow rate) updated.

4.2 Theoretical solution procedure

The code for the solar tower power plant computer simulation program was written in Visual Basic 6.0 and named "SolTowSim" (Solar Tower Simulation). This section describes in more detail the solution procedure employed in the "SolTowSim" code. Figure 4.1 gives an outline of the solution procedure followed.

4.2.1 File definition

Before running the actual simulation, the program loads all the specified input and output text files into the computer memory. Table 4.1 lists the various text files used by the program.

The input files include the files containing the meteorological data of the reference global location for each month, a file specifying the number of days of each month and a file containing all default (used for previous simulation) properties.

The simulation results are written to output text files at every (theoretical) hour. Some output files also serve as input files. At the end of every simulated day, all the calculated system properties are stored in a text file, "Daystore.txt". If a simulation is ended prematurely, "Daystore.txt" is used as an input file when resuming the unfinished simulation. The simulation is then started from the last day stored in "Daystore.txt".

Another output file, "Initial.txt" is created at the end of each simulated year. This file stores all calculated system properties on the last minute of the last day of the simulated year. As indicated by the name, "Initial.txt" is then used as input file for the first minute on the first day of the following simulation year.

The program simulates the solar tower power plant in monthly theoretical intervals, with a maximum of one year. Therefore, the user can select a simulation period of 1, 2, 3,...12 months. If the simulation is ended prematurely or finished, starting values for continuing the simulation from that point forward are saved in a text file named "SimStart.txt". These starting values include the

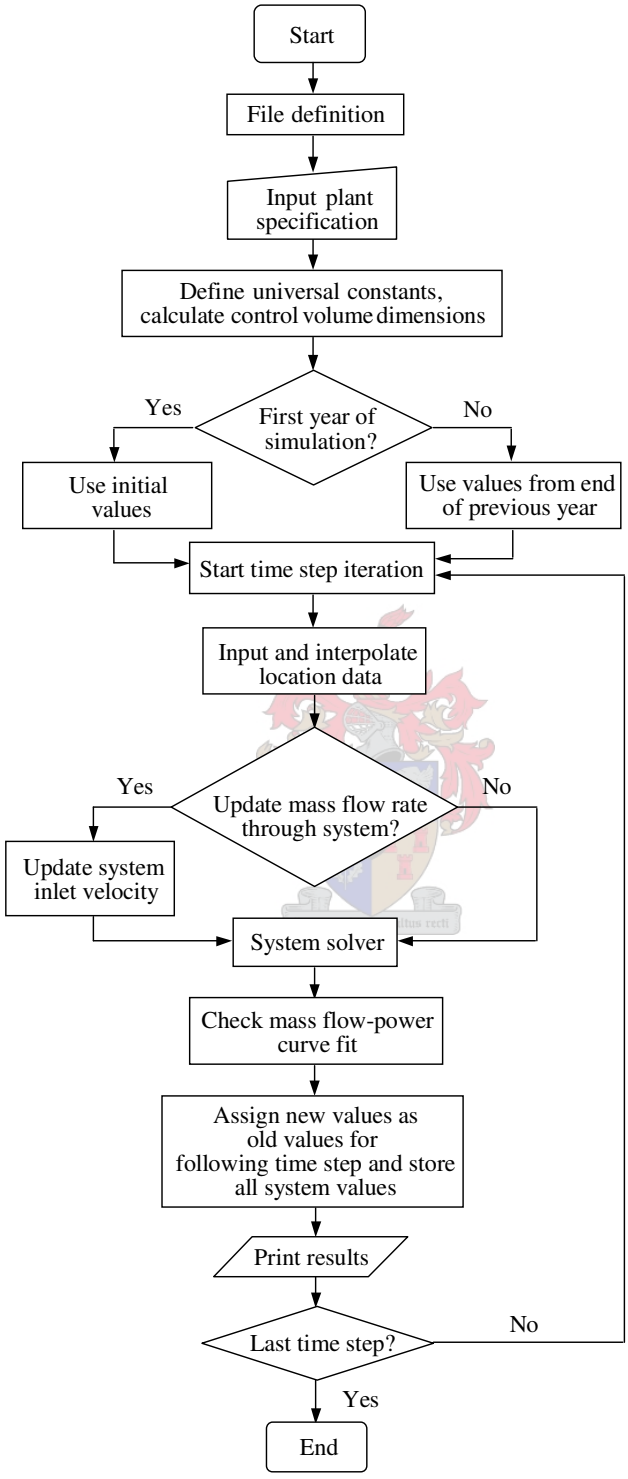

Figure 4.1: Basic flowchart for computer simulation model

Table 4.1: Input and output text files used in the "SolTowSim" code

Input files	Output files
SishenJan.txt	Checkfit.txt
SishenFeb.txt	CollectorOutput.txt
SishenMar.txt	TowerOutput.txt
SishenApr.txt	GroundOutput.txt
SishenMay.txt	Power.txt
SishenJun.txt	
SishenJul.txt	
SishenAug.txt	
SishenSep.txt	
SishenOct.txt	
SishenNov.txt	
SishenDec.txt	
Normalyear.txt	
Leapyear.txt	
Default.txt	
Daystore.txt	Daystore.txt
Initial.txt	Initial.txt
SimStart.txt	SimStart.txt

simulation year, the starting collector perimeter velocity (analogous to mass flow rate), the starting day of the year, the starting month and starting day of the specific month. These values have to be entered manually by the user.

4.2.2 Input of plant specification

When opening the program "SolarTower.exe", a box appears. This is called the form and is depicted in figure 4.2. The form allows the user to enter all the specified model variables used in the simulation and also provides easy access to changing these variables without physically changing the program code.

Before running the simulation, the user must enter the desired solar tower power plant specifications manually on the form. After starting the simulation, the program also stores the entered variables as the default variables in the text file "Default.txt". When re-opening the form, these default variables appear on the form.

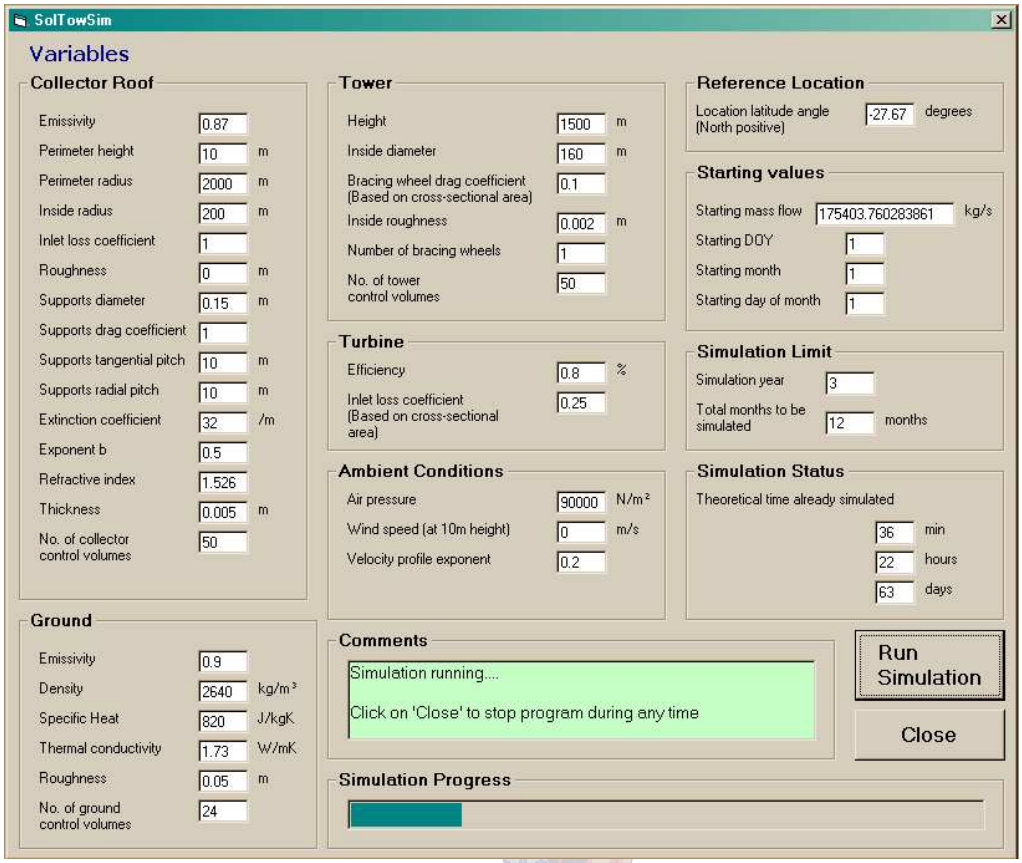

Figure 4.2: The "SolTowSim" form

4.2.3 Definition of constants and calculation of control volume dimensions

After the simulation has been started, the program defines universal constants such as gravity, Boltzmann's constant, the universal gas constant etc. Thereafter, the program calculates the collector and tower control volume dimensions according to the number of nodes specified by the user.

4.2.4 Initial value specification

In order for the program to approximate the conservation equations using finite differences, some initial temperature and pressure values are necessary. The code is written for two cases:

If it is the first year of simulation and the first day of the year, initially guessed temperature and pressure values (programmed into the code itself)

specified at each node are employed as starting point for the simulation.

If it is a second (third, fourth, etc.) year of simulation (following on a previous year), the system values determined at each node at the end of the previous simulation year are used as initial values. These values are retrieved from the file "Initial.txt" as discussed previously in this chapter.

4.2.5 Start of time step iteration

Before starting the simulation, the user enters the total months to be simulated (maximum of 12). The program now starts a loop where the calculations are to be repeated until the specified simulation period is reached. The smallest time increment is in minutes, followed by a loop for hours, days and months.

Also, headings are printed in the output files specified in table 4.1.

4.2.6 Input and interpolation of location data

The meteorological data from the reference location, given in Appendix C, is duplicated in the "Sishen(Month).txt" input files specified in table 4.1 for each particular month.

It has been found that using the input data directly from the tables in Appendix C as constant hourly values for a specific month results in a discontinuous solution. Therefore, the data read from the input files are firstly interpolated monthly and then for each minute in the hour. This results in a much smoother representation of the input data and also provides a more continuous solution.

It is assumed that the values given in the tables in Appendix C are the values on the particular solar time hour on the 15th day of each month. The program interpolates between months in the following way:

If the day of the month is before the 15th then the current month and the previous month's input files are opened and interpolated between the two months.

If the desired day is after the 15th of the month then the current and following month's input files are opened and the interpolation performed.

4.2.7 Mass flow optimization

The mass flow through the solar tower power plant system is optimized in order to produce a maximum plant power output. In actual fact, the collector inlet

velocity is optimized in the program code to give a maximum power output. Through inspection it has been found that similar results are obtained whether optimizing the mass flow or collector inlet velocity.

The optimization procedure employed in the code is illustrated by the flowchart in figure 4.3 and is described in more detail below.

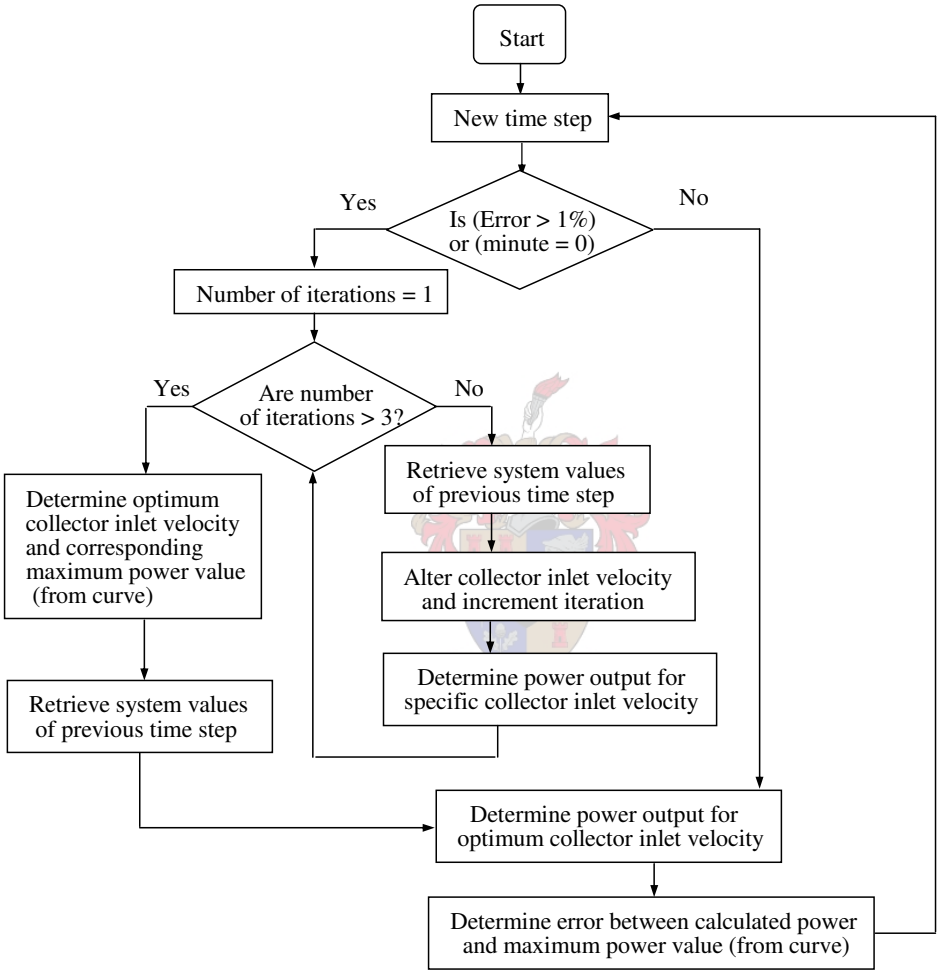

Figure 4.3: Flowchart describing the mass flow optimization procedure

If a simulation is run from the first day of the first simulation year, a guessed collector inlet velocity must be entered by the user. At the end of every (minute) time step, the program calculates the power delivered by the turbo-generator for the specified collector inlet velocity and input meteorological conditions.

At the beginning of the following time step, all the system values (temperatures, pressures, etc.) at the end of the previous time step are retrieved as a starting point. A slightly lower collector inlet velocity is employed and, using the retrieved values as a starting point, calculations are performed and the power output determined for the following time step.

This process is then repeated for a higher collector inlet velocity: The system values at the end of the previous time step are retrieved again, calculations performed and the power determined using the higher collector inlet velocity.

The process is then repeated for a final time using a still higher collector inlet velocity.

The result is that we are left with three collector inlet velocities and their corresponding plant power outputs. By using a three-point quadratic curve fit, the optimum collector inlet velocity is determined corresponding to a maximum plant power output on the curve. This maximum power given by the curve is stored as a reference value.

The system values at the end of the previous time step are once again retrieved as a starting point and the optimized value of the collector inlet velocity is employed for the following time step. The system values (temperatures, pressures, etc.) now calculated by the system solver (as in figure 4.1) and the power output obtained using the optimized velocity value are stored as the actual solar tower power plant conditions for the specific (new) time step.

At the end of each time step, the power calculated by the program is compared to the maximum power reference value given by the quadratic curve. The percentage error between the calculated power and the reference curve value is also determined (called "Error" in figure 4.3).

In following time steps, the collector inlet velocity is only updated (optimized) if the power calculated by the program differs by more that a percentage point from the reference value given by the curve. This causes the collector inlet velocity to be updated frequently during times of significant transient energy changes (e.g. during sunrise and sunset) and less frequently during times of small transient energy changes (e.g. during the middle of the day). As a further measure of assuring accuracy, the collector inlet velocity is also forced to be updated on the stroke of every hour (when minute = 0, as in figure 4.3).

4.2.8 System solver

If the input solar radiation is greater than zero, it indicates a sun position above the horizon. The program now calculates the beam radiation incidence angle on the collector roof for a specific global location for a specific day in the year at the specific time step during the day. This incidence angle is then used to determine the reflective, absorptive and transmissive characteristics of the collector roof for the beam radiation component on the particular time step. The roof characteristics for the diffuse radiation component is also obtained using the effective diffuse incidence angle.

Starting from the collector perimeter and moving in towards the tower, the discretized collector conservation equations (given in chapter 2) are solved using the Gauss-Seidel iterative method for each collector control volume. The collector continuity, momentum, air energy and roof energy equations are solved sequentially, while the ground energy equations (ground temperatures at different depths) are solved using the Thomas algorithm (TDMA matrix). The various temperatures, pressure and air velocity are calculated for each node in the collector.

After finding the collector solution, we move to the turbine. The program takes the property changes caused by the turbine into account and then moves up into the tower where the discretized tower conservation equations (given in chapter 2) are solved iteratively using the Gauss-Seidel method for each tower control volume. The tower air temperature, pressure and air velocity are calculated at each node.

The draught equation described in chapter 3 is solved and the power generated by the turbo-generator for the specific time step is calculated.

4.2.9 End of time step iteration

In order to continue the time step iteration, some of the newly calculated values are stored as old values for the following time step. These old values are employed in equations which contain transient energy terms. All the system values (temperatures, pressures, velocities, etc.) are stored at the end of the time step iteration to use as starting values for the next time step.

4.2.10 Printing of results

The system values are printed under the correct headings to the output text files discussed earlier in this chapter.

4.3 Decreasing computing time

As discussed in chapter 2, initially the simple backward difference method was employed for the discretization of the collector and tower air equations, while the Crank Nicholson (modified for variable ground control volume thicknesses) scheme was used for the discretization of the ground energy equations. Also, at first all the collector equations were solved using the Gauss-Seidel iterative method. Separate from the collector, the tower equations are solved using the Gauss-Seidel iterative method.

Together the discretized collector equations formed a system of first (air) and second order (ground) equations respectively. Solving this system proved to be very time consuming, due mainly to the fact that a high number of control volumes were necessary to ensure convergence of the solution.

After consulting Buys (2003-2004), it was decided to use different, more accurate discretization schemes. A second order backward difference scheme was introduced for the collector and tower air equations, while a higher order, modified Crank Nicholson (Mehrstellen) method was employed for the discretization of the ground energy equations. It was also decided to solve the ground energy equations using the Thomas algorithm, which provides a direct and faster ground temperature solution. For the collector, the solution of the TDMA matrix (ground equations) and the solutions of the air and roof equations are incorporated in an iterative Gauss-Seidel method. Separate from the collector, the tower equations are still solved using the Gauss-Seidel method.

The change to higher order discretization schemes allowed the use of fewer control volumes for achieving a converging solution. Fewer control volumes also means fewer calculations, effecting a considerably reduced computation time. By solving the ground energy equations separately using a TDMA matrix instead of an iterative method, the computing time was reduced even further.

Chapter 5

Plant Performance Characteristics

A numerical simulation was performed using the reference plant (from Appendix H) specifications. The simulation was performed repeatedly for a number (approximately 15) of years, taking the values at the end of each year as input values to the following year. This was done in order to ensure stabilized ground temperatures, due to the transient nature of the ground.

The following section discusses the results produced by this and other simulations and briefly investigates a way of maximizing the power output delivered by the plant. The effect that increased plant dimensions have on the power produced is presented. The influence of the tower shadow on the plant power output is also investigated (as discussed in Appendix F). Lastly, the performance of the solar tower power plant in the presence of the prevailing winds at the proposed location (Sishen) is evaluated (see Appendix G).

5.1 Results

The maximum power output of the reference plant for the 21st day of each month is shown in figures 5.1 and 5.2. The output varies considerably during the day with the peak output delivered approximately an hour after solar noon. Due to the energy storage capability of the ground, some power is also produced at night. There are significant differences in the output during the summer and winter months, where the power output during January is more than double than that of June.

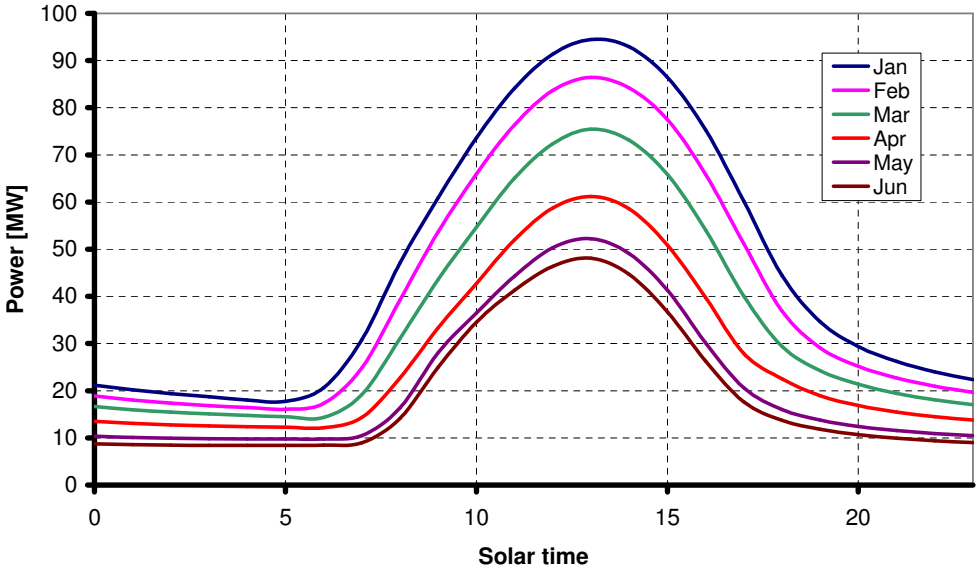

Figure 5.1: Maximum electrical power output for reference plant - first semester

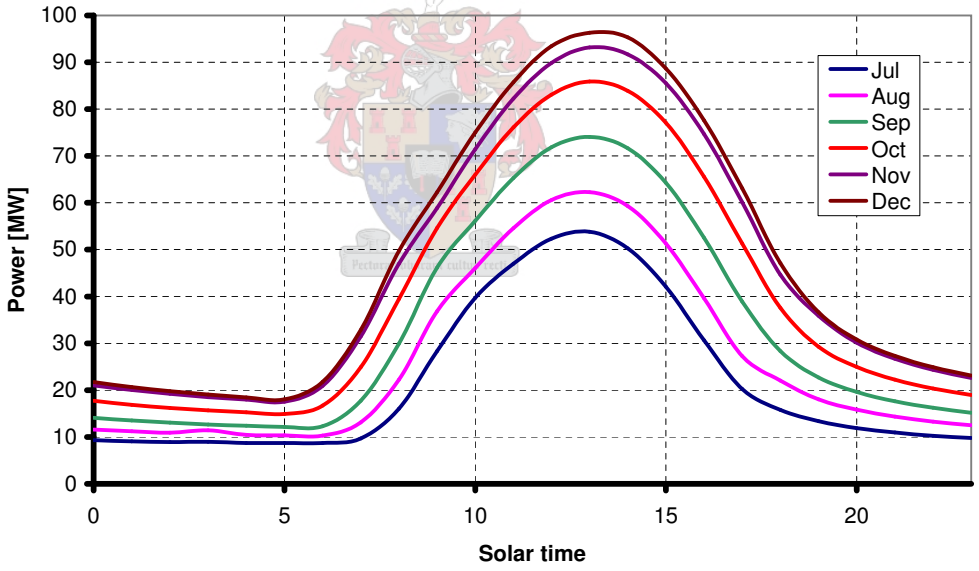

Figure 5.2: Maximum electrical power output for reference plant - second semester

Figure 5.3 shows the pressure drop across the turbine and the mass flow rate through the turbine on 21 December. It is clear that both of the curves follow the same trend as the power output curves illustrated in figures 5.1 and 5.2. The turbine pressure drop varies from its lowest point (at 05:00 solar time) of 167 N/m^2 to a peak (at 13:00 solar time) of 496 N/m^2. The mass

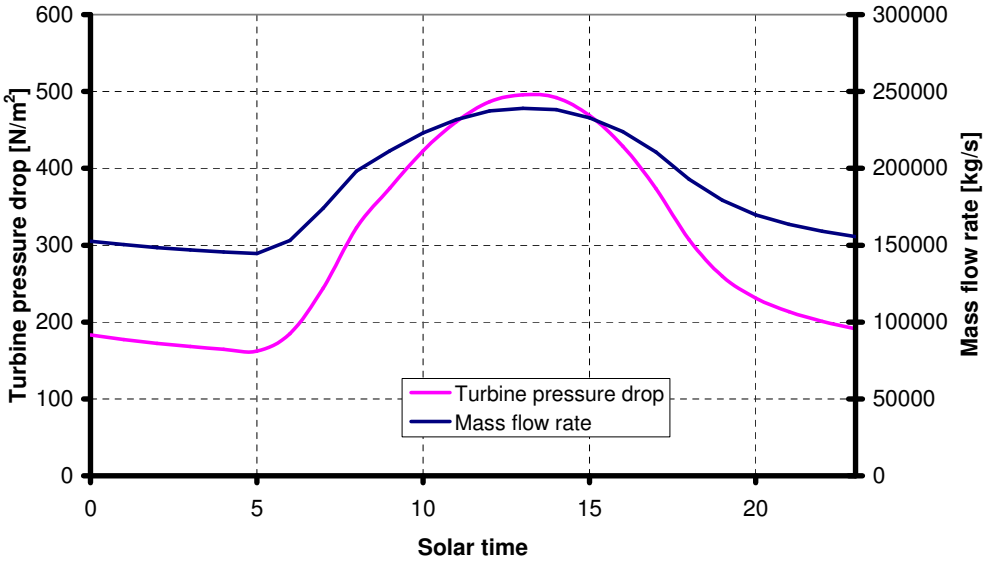

Figure 5.3: Turbine pressure drop and mass flow rate on 21 December

flow rate through the turbine varies between approximately 147000 kg/s (at 05:00 solar time) to nearly 240000 kg/s (at 13:00 solar time).

Figures 5.4 and 5.5 illustrate the temperature distributions in the ground at various times of the day. It is clear that the ground surface temperature is at its hottest during midday, while at night the temperatures deeper into the ground are higher than the surface temperatures. The higher ground temperatures deeper into the ground (at night) facilitate conduction to the surface, which causes a heat flux to the air in the collector and ultimately night power generation.

The shift in average ground temperature near the surface is also evident, where the average ground temperature at (for example) 0.5 m in December is much higher than in June.

The ground temperature deep in the ground (at 14 m below the ground surface) stabilizes at approximately 36 °C, as illustrated in figure 5.5.

5.2 Maximizing the power output

Multiple computer simulations were run for various combinations of collector roof shapes and inlet heights. The basic reference plant specifications (given in Appendix H) and varying values of b and H_2 (see figure 1.1) were employed.

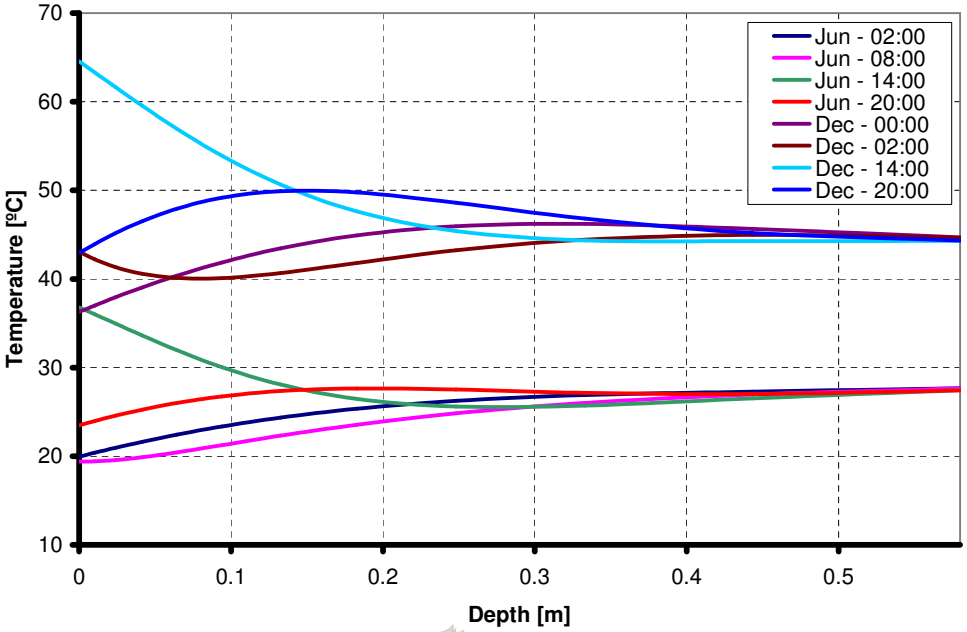

Figure 5.4: Temperature distribution in ground near the ground surface

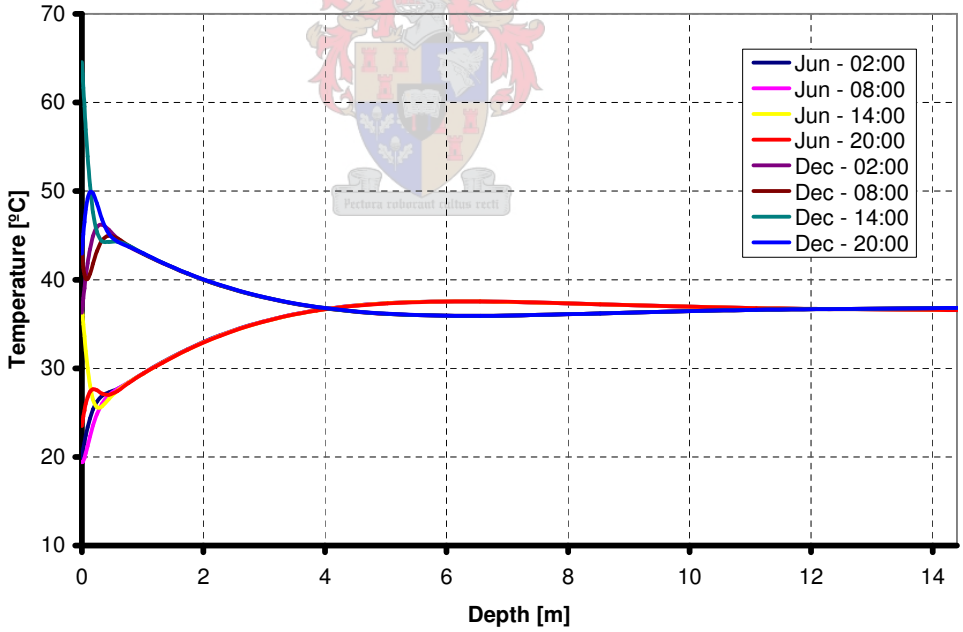

Figure 5.5: Temperature distribution in ground

Figure 5.6 gives the maximum annual power output for a solar tower power plant using these varying combinations.

Results show that the reference plant produces approximately 298 GWh/a, as is evident from figure 5.6. The results of a numerical model by Hedderwick (2001) predicts an annual power output of 367 GWh/a for the same reference plant as given in Appendix H. This can be attributed to the fact that Hedderwick (2001) assumes a turbo-generator efficiency of unity, while this study employs a turbo-generator efficiency of 80 %.

Kröger & Buys (2001) also present simulation results for the above mentioned reference plant. Their model gives an annual plant power output of 341 GWh/a. It is believed that the model by Kröger & Buys (2001) predicts a higher plant power output compared to this study, due mainly to the different approaches used to maximize the plant power output (by optimizing the mass flow rate through the plant). Another factor which contribute to the difference in predicted power output is the fact that Kröger & Buys (2001) do not take the temperature drop across the turbine into account. Also, the model by Kröger & Buys (2001) employs a developing and fully developed flow region in the collector, compared to this study's implementation of only a fully developed flow regime throughout the collector.

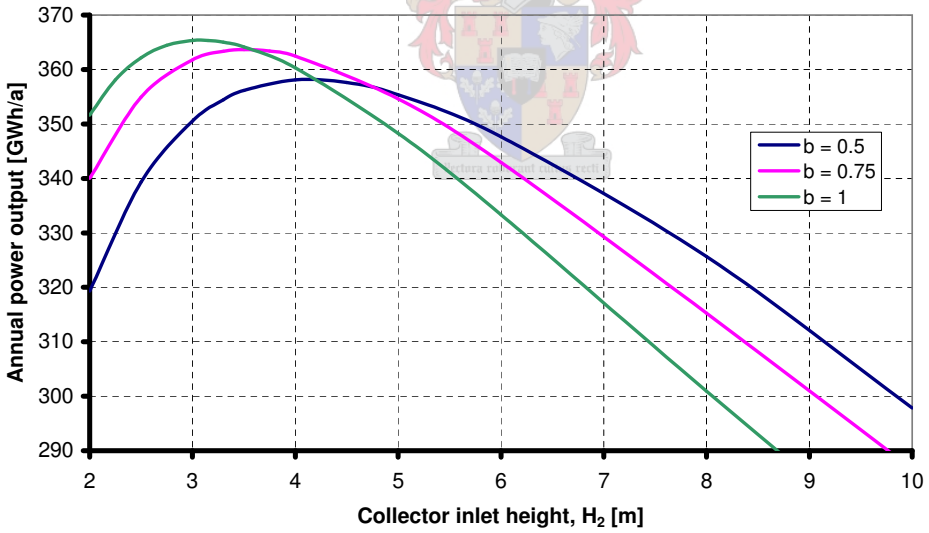

Figure 5.6: Annual power output for various roof shapes and collector inlet heights

The output can be increased by altering the shape and inlet height of the collector roof. A maximum power output is reached with a roof shape exponent of $b = 1$ and collector perimeter height of $H_2 = 3.1$ m.

5.3 The effect of plant dimensions on power delivered

Simulations were run in order to study the effect of increasing plant dimensions on plant power output. Specifically, the effect of the size of the collector diameter and tower height on the power produced were investigated. It is assumed from the results of the previous simulations that a roof shape exponent of $b = 1$ will produce a maximum power output.

Once again, the reference plant specifications were employed (with $b = 1$), with varying values of collector diameter d_c and tower height H_t. In each case, the optimum collector inlet height for each corresponding collector diameter was determined. Figures 5.7 to 5.9 show the maximum annual power output for a solar tower power plant with respective tower heights of $H_t = 500$ m, $H_t = 1000$ m and $H_t = 1500$ m and varying collector diameters.

From these figures it is clear that the annual plant output can be dramatically increased by enlarging the collector diameter or tower height.

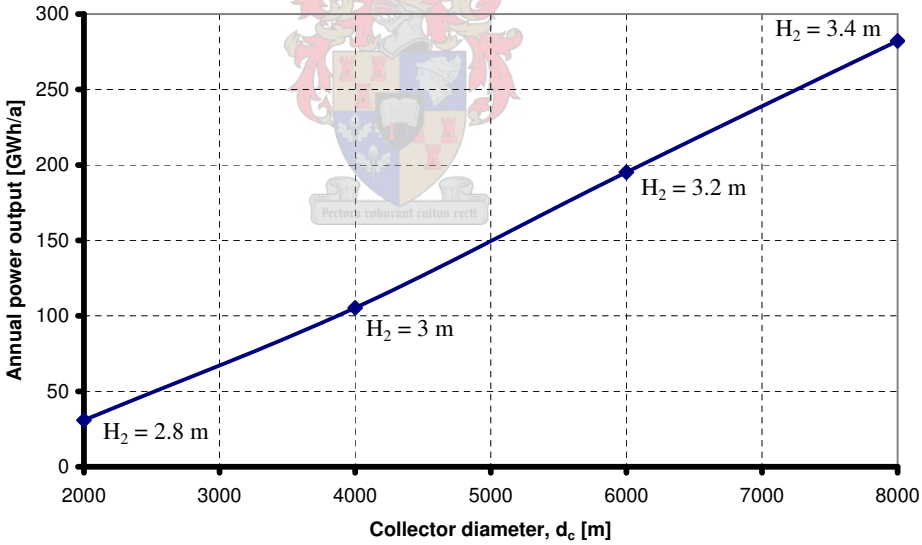

Figure 5.7: Annual power output as a function of collector diameter, with $H_t = 500$ m (b=1)

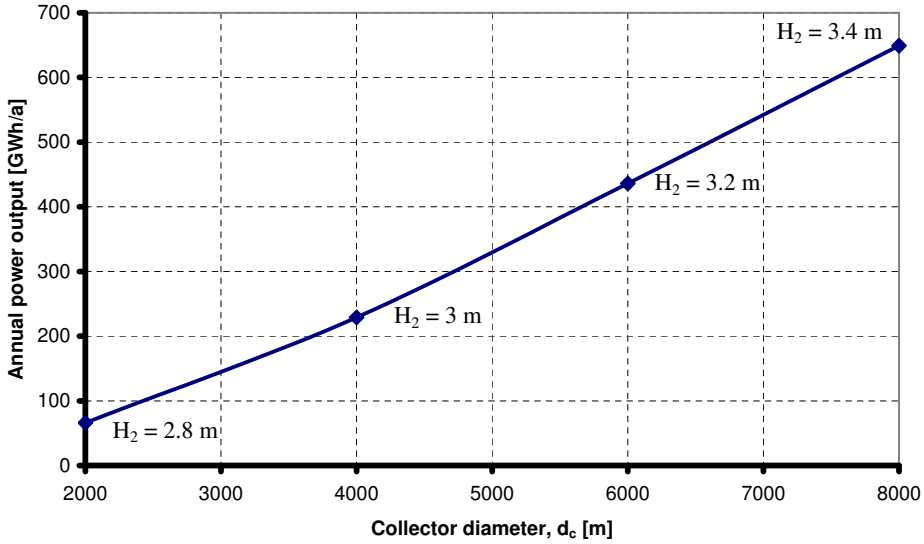

Figure 5.8: Annual power output as a function of collector diameter, with H_t = 1000 m (b=1)

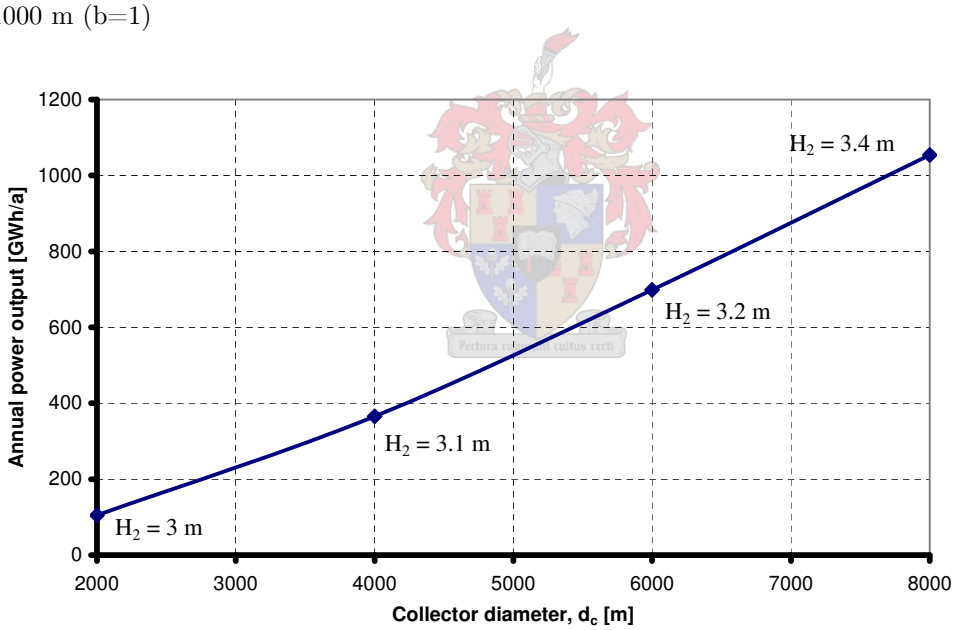

Figure 5.9: Annual power output as a function of collector diameter, with H_t = 1500 m (b=1)

5.4 The effect of the tower shadow on power delivered

During the day, the tower of the solar tower power plant casts a shadow on the collector. Simulations were run to determine the effect of the tower shadow

on the plant power output. Simulations are repeated for a number of years to ensure stabilized results. The strategy on how the tower shadow effect is taken into account when performing power output calculations is discussed in Appendix F.

Figure 5.10 compares the power output curves (on 21 June and 21 December) of the reference plant with that of the reference plant model which takes the tower shadow into account.

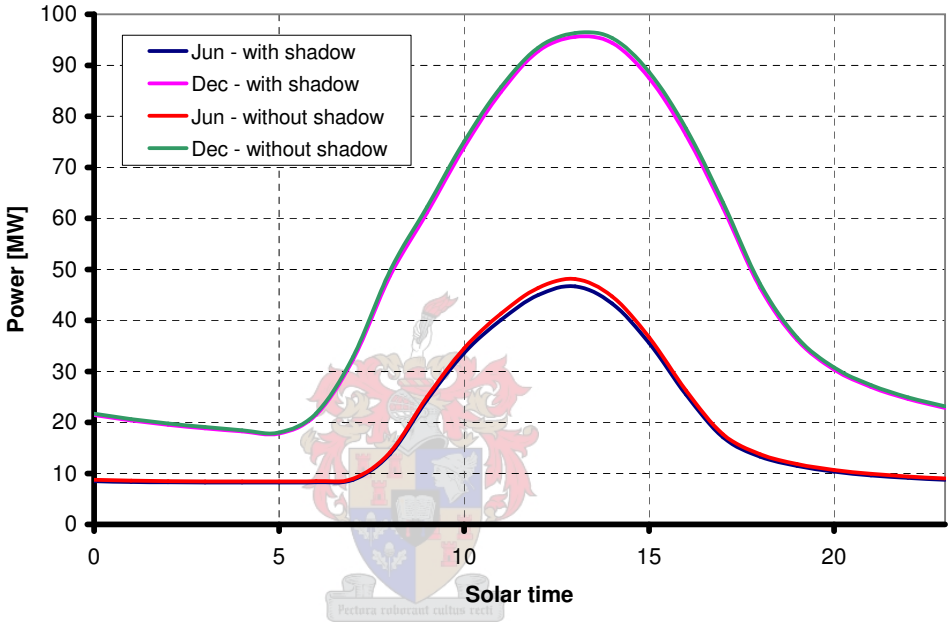

Figure 5.10: Effect of tower shadow on plant power output

It is evident from figure 5.10 that the tower shadow has little effect on the power delivered by the solar tower power plant. Closer inspection reveals that the power produced by the plant which takes the shadow into account is marginally less (throughout the day) than the power output of the plant not considering the tower shadow. Also, the effect of the tower shadow on power generation is more pronounced in winter than in summer months.

A better way of analyzing the influence of the tower shadow is by regarding its effect on the annual power output of the solar tower power plant. Table 5.1 compares the annual power output of the reference plant with the model of the reference plant which incorporates the tower shadow effect. The "Reference plant" in table 5.1 again refers to the plant specified in Appendix H.

Table 5.1: Annual power output comparison illustrating the tower shadow effect

Plant configuration	**Annual power output** [GWh]
Reference plant	297.85
Reference plant incorporating tower shadow effect	292.58

From table 5.1 it is clear that the shadow cast by the tower reduces the annual power output of the solar tower power plant by approximately 1.8 %. It should also be noted that for the same chimney height, an increased collector area gives a decreased tower shadow effect on the plant power output.

5.5 The effect of prevailing winds on power delivered

Previous studies have confirmed that windy ambient conditions affects the performance of cooling towers. It is therefore natural to investigate the performance of a solar tower power plant in the presence of wind. Simulations were run to determine the effect of ambient wind on the plant power output. Simulations are repeated for a number of years to ensure stabilized results. Appendix G discusses how the effect of ambient wind is incorporated into the numerical model.

Figure 5.11 compares the power output curves (on 21 June and 21 December) of the reference plant with that of the reference plant model which takes the effect of ambient cross-winds into account.

From figure 5.11 it is clear that the prevailing winds significantly decrease the plant power output. This is primarily due to the convective heat losses from the collector roof to the environment. The windy conditions result in an increased convective heat transfer coefficient, facilitating a greater heat flux to the environment.

Strong winds at the height of the tower outlet should boost the airflow through the plant, resulting in an increased plant power output. This is caused due to a pressure rise (Δp_{to}) at the tower outlet, discussed in section 3.3.5. However, the prevailing winds are not strong enough to effect a significant tower outlet pressure rise.

When regarding figure 5.11 more closely, one finds that during the early mornings and late evenings of June (winter), the plant generates a slightly higher power output in windy conditions than during no-wind conditions. This

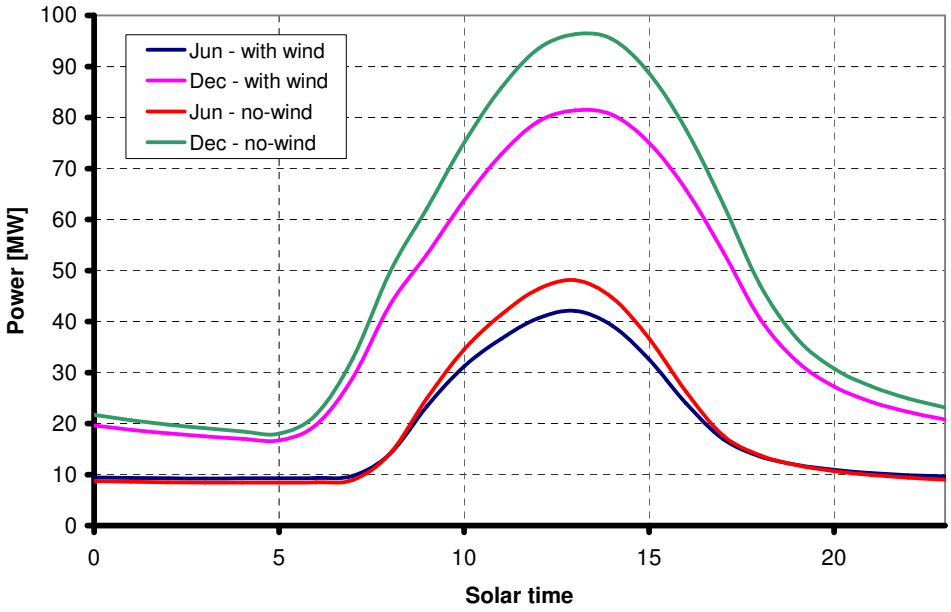

Figure 5.11: Effect of ambient wind on plant power output

is due to the fact that the ambient temperature at these times are marginally higher than the corresponding collector roof temperatures. Therefore, the windy conditions actually cause a minor convective heat flux from the environment to the collector roof, resulting in a slightly increased plant power output.

Again we can analyze the influence of ambient winds by regarding its effect on the annual power output of the solar tower power plant. Table 5.2 compares the annual power output of the reference plant with the model of the reference plant which incorporates wind effects. The "Reference plant" in table 5.2 again refers to the plant specified in Appendix H.

Table 5.2: Annual power output comparison illustrating the effect of ambient wind

Plant configuration	**Annual power output** [GWh]
Reference plant	297.85
Reference plant incorporating ambient wind effects	264.56

From table 5.2 it is clear that the prevailing winds at the proposed site reduce the annual power output of the plant by approximately 11.2 %.

Chapter 6

Conclusion

The main objective of this study was to develop a computer code with which the performance characteristics of large-scale solar tower power plants can be evaluated.

A mathematical model was developed for a solar tower power plant by deriving the relevant draught and conservation equations for an elementary control volume in the collector and tower of the plant. An extensive order of magnitude analysis was performed in order to simplify the derived equations. The equations were discretized using finite difference methods and implemented in a computer simulation model.

A complete numerical computer model was developed, taking into account the global site location, the position of the sun on the specific day of the year and all frictional, inlet, outlet, support and heat losses. Simulation results are based on a defined reference plant, using specified meteorological input data for a particular site in South Africa.

Comparative results to earlier studies are found and similar trends established. Numerical simulation results indicate that the plant power output varies considerably during a typical day and seasonal changes in output are significant. Peak plant output is achieved shortly after midday, while the ground's energy storage capacity facilitates power generation at night.

It is shown that the output of a plant can be increased by optimizing the collector roof shape and inlet height. The power produced by the plant can also generally be increased by increasing the collector diameter or tower height.

The influence of the tower shadow falling across the collector during the day is investigated. Results indicate the shadow only causes a minor effect on

the plant power output.

A preliminary study into the influence of ambient winds on the power output of the solar tower power plant finds that the plant experiences a significant reduction in the annual power generation in the presence of wind.

Although the work done in this study follows on previous studies, such as that of Hedderwick (2001), many factors contribute to the uniqueness of this study. Some of these factors include:

- The use of a quasi-steady state solution procedure,
- The simulation of the tower and tower losses using tower control volumes,
- The implementation of more accurate second and higher order discretization schemes for the ground energy equations,
- The development of a sound and user-friendly computer simulation model requiring less computation time than previous models,
- The ability of the simulation model to evaluate various solar tower power plant configurations at any global location,
- The ability of the simulation model to change the frequency of optimization as transient effects increase / decrease,
- The incorporation into the model of factors such as wind effects, tower shadow effects and property changes across the turbine.

Future studies into the solar tower power plant should consider further investigation into the effects of wind, inversions, material properties, plant dimensions, double glazing, controlled heat storage and turbine performance on the plant power output. It is also expected that the implementation of more accurate heat transfer correlations into the model will have a significant effect on plant performance.

The main area of research however should be the optimization of the plant, in order to ensure maximum annual power generation or to satisfy particular demand patterns.

List of References

Bernardes, M.A.d.S., Voß, A. and Weinrebe, G. (2003 December). Thermal and technical analyses of solar chimneys. *Solar Energy*, vol. 75, no. 6, pp. 511–524. (Cited on page 4.)

Burger, L.W. and Scorgie, Y. (1999 July). Meteorological investigation for the solar chimney project proposed for Sishen, Northern Cape. Tech. Rep., Environmental Management Services CC. (Cited on page 148.)

Buxmann, J. (1983). Strömungsverteiling und Wärmeübertragung bei unterschiedlichen Elementanordnugen im Trockenkühlturm. Tech. Rep. 61, Subproject E10, Report nr. 54, Universität Hannover. (Cited on pages 38 and 147.)

Buys, J.D. (2003-2004). Personal Communication, University of Stellenbosch, Stellenbosch, South Africa. (Cited on pages 10, 11, 16, 26, 27, 28, 30, 52, 119, 120, and 129.)

Du Preez, A.F. (1992 November). *The Influence of Cross-winds on the Performance of Natural Draft Dry-cooling Towers*. Ph.D. thesis, University of Stellenbosch, Stellenbosch, South Africa. (Cited on pages 39 and 147.)

Du Preez, A.F. and Kröger, D.G. (1994). The influence of a buoyant plume on the performance of a natural cooling tower. 9th IAHR Cooling Tower and Spraying Pond Symposium, Brussels. (Cited on page 39.)

Duffie, J.A. and Beckman, W.A. (1991). *Solar Engineering of Thermal Processes*. 2nd edn. John Wiley and Sons, Inc., New York. (Cited on pages 135, 136, 137, 138, 139, 140, 141, and 143.)

Gannon, A.J. (2002). *Solar Chimney Turbine Performance*. Ph.D. thesis, University of Stellenbosch, Stellenbosch, South Africa. (Cited on page 4.)

Gannon, A.J. and von Backström, T.W. (2000). Solar chimney cycle analysis with system loss and solar collector performance. *Journal of Solar Energy Engineering*, vol. 122, pp. 133–137. (Cited on page 34.)

Gannon, A.J. and Von Backström, T.W. (2003). Solar chimney turbine performance. *Journal of Solar Energy Engineering*, vol. 125, pp. 101–106. (Cited on pages 4 and 34.)

Günther, H. and de Haas, W. (1931). *Die künftige Energieversorgung der Welt.* Franck'sche Verlagshandlung, Stuttgart. (Cited on page 2.)

Haaf, W. (1984). Solar chimneys, part II: Preliminary test results from the Manzanares pilot plant. *International Journal of Solar Energy*, vol. 2, pp. 141–161. (Cited on page 2.)

Haaf, W., Friedrich, K., Mayr, G. and Schlaich, J. (1983). Solar chimneys, part I: Principle and construction of the pilot plant in Manzanares. *International Journal of Solar Energy*, vol. 2, pp. 3–20. (Cited on page 2.)

Haaland, S.E. (1983). Simple and explicit formulas for the friction factor in turbulent pipe flow. *Transactions of the ASME, Journal of Fluids Engineering*, vol. 185, no. 3, pp. 89–90. (Cited on pages 21 and 93.)

Hedderwick, R.A. (2001). *Performance Evaluation of a Solar Chimney Power Plant.* Master's thesis, University of Stellenbosch, Stellenbosch, South Africa. (Cited on pages xv, 4, 14, 15, 35, 57, 64, 81, 94, 95, 106, and 107.)

Kröger, D.G. (2001-2004). Personal Communication, University of Stellenbosch, Stellenbosch, South Africa. (Cited on pages 19 and 23.)

Kröger, D.G. (2004). *Air-cooled Heat Exchangers and Cooling Towers.* Pennwell Corp., Tulsa, Oklahoma. (Cited on pages xv, 13, 14, 21, 35, 37, 40, 89, 90, 96, 106, and 158.)

Kröger, D.G. and Blaine, D. (1999). Analysis of the driving potential of a solar chimney power plant. *South African Institution of Mechanical Engineering, R & D Journal*, vol. 15, pp. 85–94. (Cited on page 4.)

Kröger, D.G. and Buys, J.D. (1999). Radial flow boundary layer development analysis. *South African Institution of Mechanical Engineering, R & D Journal*, vol. 15, pp. 95–102. (Cited on pages 4, 12, 158, and 160.)

Kröger, D.G. and Buys, J.D. (2001). Performance evaluation of a solar chimney power plant. ISES 2001 Solar World Congress, Adelaide, South Australia. (Cited on pages 4, 13, 14, 15, 18, 24, 28, 29, 34, 35, 36, and 57.)

Lombaard, F. (2002). *Performance of a Solar Air Heater incorporating Thermal Storage.* Master's thesis, University of Stellenbosch, Stellenbosch, South Africa. (Cited on pages 136, 139, and 141.)

McAdams, W.H. (1954). *Heat Transmission*. 3rd edn. McGraw-Hill, New York. (Cited on page 19.)

Mills, A.F. (1995). *Heat and Mass Transfer*. Richard D. Irwin Inc. (Cited on pages xv, 17, 18, and 24.)

Modest, M.F. (1993). *Radiative Heat Transfer*. McGraw Hill Inc., New York. (Cited on pages xv, 18, 77, 133, and 135.)

Mullett, L.B. (1987). The solar chimney - overall efficiency, design and performance. *International Journal of Ambient Energy*, vol. 8, pp. 35–40. (Cited on page 2.)

Padki, M.M. and Sherif, S.A. (1988). Fluid dynamics of solar chimneys. *Proceedings of the ASME Winter Annual Meeting*, pp. 43–46. (Cited on page 3.)

Pasumarthi, N. and Sherif, S.A. (1998*a*). Experimental and theoretical performance of a demonstration solar chimney model - part I: Mathematical model development. *International Journal of Energy Research*, vol. 22, pp. 277–288. (Cited on page 3.)

Pasumarthi, N. and Sherif, S.A. (1998*b*). Experimental and theoretical performance of a demonstration solar chimney model - part II: Experimental and theoretical results and economic analysis. *International Journal of Energy Research*, vol. 22, pp. 443–461. (Cited on page 4.)

Schlaich, J. (1991). World energy demand, population explosion and pollution: could solar energy utilisation become a solution? *The Structural Engineer*, vol. 69, no. 10, pp. 189–192. (Cited on page 3.)

Schlaich, J. (1994). *The Solar Chimney: Electricity from the Sun*. Deutsche Verlags-Anstalt, Stuttgart. (Cited on page 3.)

Schlaich, J. (1999). Tension structures for solar electricity generation. *Engineering structures*, vol. 21, pp. 658–668. (Cited on pages 4 and 29.)

Simon, M. (1976). Konzept der atmosphärischen Nutzung. in AGS/ASA-study energiequellen für morgen? *Nichtfossile/nichtnukleare Energiequellen, Teil II: Nutzung der solaren Strahlungsenergie*, pp. 555–564. Umschau–Verlag. (Cited on page 2.)

Swinbank, W.C. (1963). *Long wave radiation from clear skies*, vol. 89. Quart J. Royal Met. Soc. (Cited on page 20.)

Von Backström, T.W. (2003). Calculation of pressure and density in solar power plant chimneys. *Transactions of the ASME, Journal of Solar Energy Engineering*, vol. 125, pp. 127–129. (Cited on page 41.)

Von Backström, T.W., Bernhardt, A. and Gannon, A.J. (2003). Pressure drop in solar power plant chimneys. *Transactions of the ASME, Journal of Solar Energy Engineering*, vol. 125, pp. 1–5. (Cited on pages 29, 40, and 93.)

Von Backström, T.W. and Gannon, A.J. (2000*a*). Compressible flow through solar power plant chimneys. *Transactions of the ASME, Journal of Solar Energy Engineering*, vol. 122, pp. 1–8. (Cited on page 36.)

Von Backström, T.W. and Gannon, A.J. (2000*b*). The solar chimney air standard thermodynamic cycle. *South African Institution of Mechanical Engineering, R & D Journal*, vol. 16, no. 1, pp. 16–24. (Cited on page 4.)

White, F.M. (1999). *Fluid Mechanics*. 4th edn. McGraw-Hill. (Cited on pages xv, 14, 28, and 29.)

Appendices

Pectora roborant cultus recti

Appendix A

Derivation of Conservation Equations

A.1 Collector

In the following section, the continuity, momentum and energy equations are derived for a defined elementary control volume in the collector of a solar tower power plant.

The roof of the collector is inclined from the outer boundary towards the tower. It will be assumed that the inclination is small enough such that a one-dimensional radial flow approximation is acceptable. The control volume in the collector is chosen at an arbitrary radial position between the collector inlet and the turbine inlet.

A.1.1 Continuity equation

Consider from figure A.1 the following mass conservation relation applicable to purely radial airflow through a defined elementary control volume with radial length Δr and subtended angle $\Delta\theta$ under the roof of the collector:

$$\rho v r \Delta\theta H = \rho v r \Delta\theta H + \frac{\partial}{\partial r}\left(\rho v r \Delta\theta H\right)\Delta r + \frac{\partial}{\partial t}\left(\rho r \Delta\theta \Delta r H\right) \tag{A.1}$$

where the density and radial velocity of the air moving through the defined control volume are respectively ρ and v, while H is the height of the collector roof at a specific radial position.

Equation (A.1) can be simplified as follows:

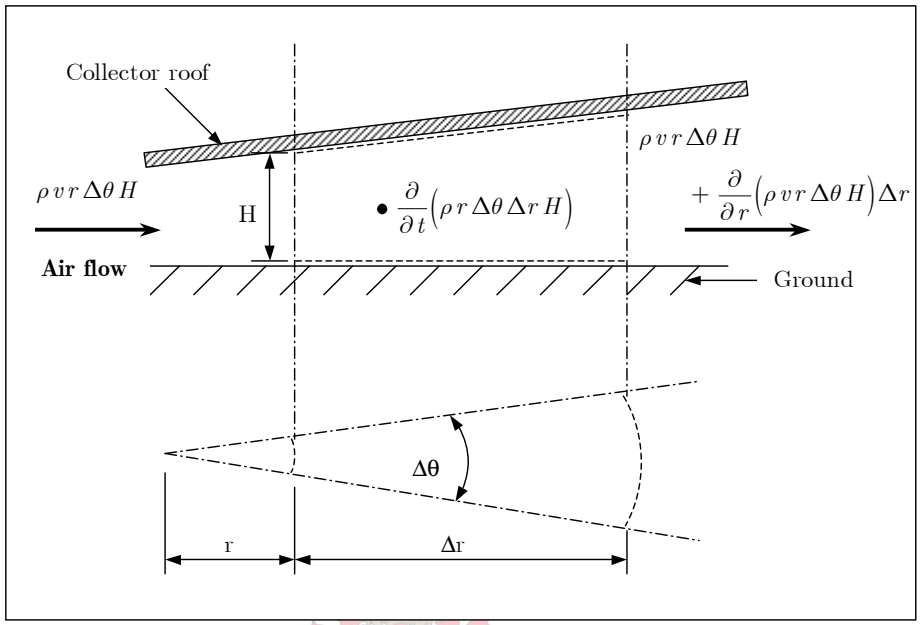

Figure A.1: Conservation of mass applied to a control volume in the collector

$$\frac{\partial}{\partial r}\left(\rho v r \Delta\theta H\right)\Delta r = -\frac{\partial}{\partial t}\left(\rho r \Delta\theta \Delta r H\right) \tag{A.2}$$

Divide equation (A.2) by $r\Delta\theta\Delta r$ and find

$$\frac{1}{r}\frac{\partial}{\partial r}\left(\rho v r H\right) = -H\frac{\partial \rho}{\partial t} \tag{A.3}$$

During steady state conditions or when transient effects are negligible, equation (A.3) becomes

$$\frac{1}{r}\frac{\partial}{\partial r}\left(\rho v r H\right) = 0 \tag{A.4}$$

A.1.2 Momentum equation

When regarding figure A.2 a momentum equation can be formulated for the radial flow of the air stream in the collector.

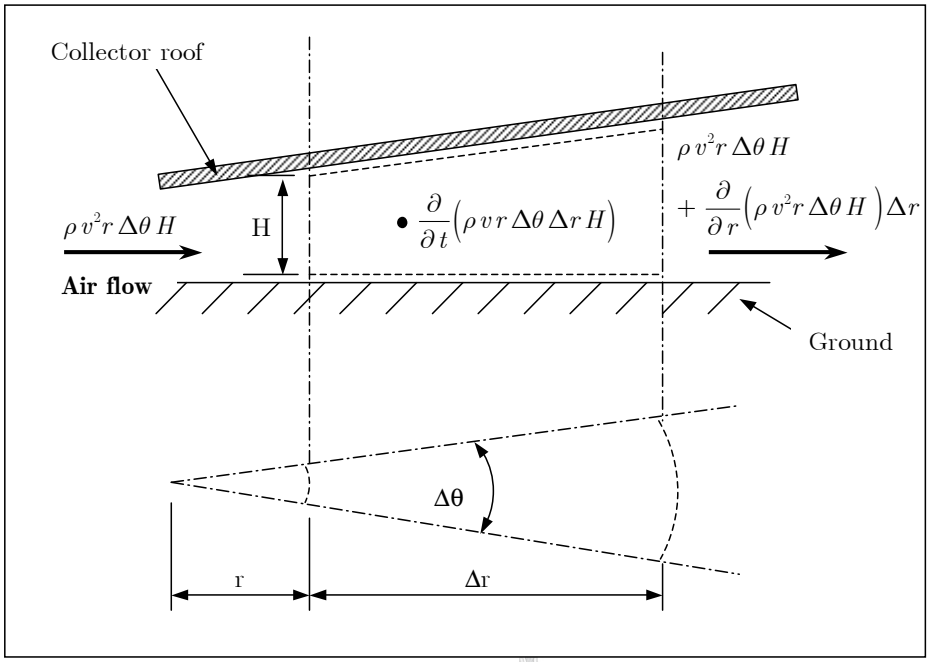

Figure A.2: Conservation of momentum applied to a control volume in the collector

$$\sum F = -\rho v^2 r \Delta\theta H + \rho v^2 r \Delta\theta H + \frac{\partial}{\partial r}\left(\rho v^2 r \Delta\theta H\right)\Delta r + \frac{\partial}{\partial t}\left(\rho v r \Delta\theta \Delta r H\right) \tag{A.5}$$

where ΣF represents the sum of the forces acting on the control volume.

Consider figure A.3 showing schematically the forces exerted on the control volume. The sum of the normal forces acting on the sides of the control volume is determined by taking the average pressure and height on each of the sides:

$$\begin{aligned} F_{\text{side,normal}} &= 2 p_{\text{avg}} A_{\text{side}} \\ &= 2\left[0.5\left(p + p + \frac{\partial p}{\partial r}\Delta r\right) 0.5\left(H + H + \frac{\partial H}{\partial r}\Delta r\right)\Delta r\right] \end{aligned} \tag{A.6}$$

The radial component of the full normal force is calculated by multiplying by $\sin(\Delta\theta/2)$. It is assumed that both $\Delta\theta$ and Δr are small, therefore $\sin(\Delta\theta/2) \approx (\Delta\theta/2)$ and higher orders of Δr are neglected, giving

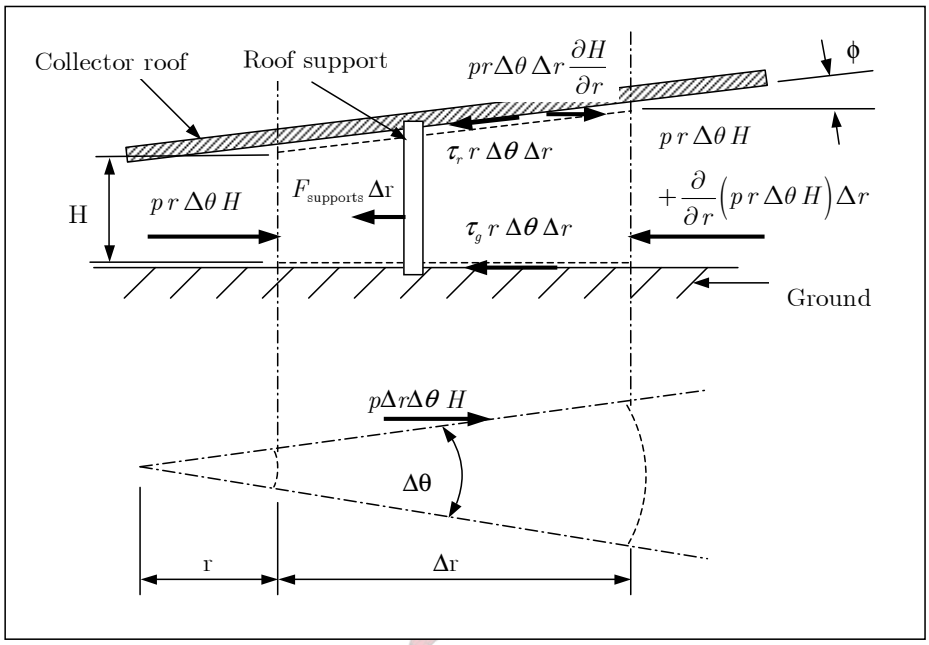

Figure A.3: Forces acting on an air stream control volume in the collector

$$\begin{aligned} F_{\text{side,radial}} &= 0.25\Delta r\Delta\theta\left[4pH + 2H\frac{\partial p}{\partial r}\Delta r + 2p\frac{\partial H}{\partial r}\Delta r + \left(\frac{\partial p}{\partial r}\right)\left(\frac{\partial H}{\partial r}\right)\Delta r^2\right] \\ &= p\Delta r\Delta\theta H \end{aligned} \tag{A.7}$$

The inclined roof exerts a normal force on the control volume. This force is calculated using the average pressure on the top of the control volume. Due to the assumption of a small incline, the control volume roof area is approximated as $r\Delta\theta\Delta r$ and $\sin\phi \approx \frac{\partial H}{\partial r}$. Thus, the normal force is

$$F_{\text{roof,normal}} = p_{\text{avg}}A_{\text{roof}} = 0.5\left(p + p + \frac{\partial p}{\partial r}\Delta r\right) r\Delta\theta\Delta r \tag{A.8}$$

The radial component is calculated by multiplying $\sin\phi$ with the normal force. Once again, higher order terms may be neglected giving the radial force

$$F_{\text{roof,radial}} = \left(pr\Delta\theta\Delta r + 0.5\frac{\partial p}{\partial r}r\Delta\theta\Delta r^2\right)\frac{\partial H}{\partial r} = pr\Delta\theta\Delta r\frac{\partial H}{\partial r} \tag{A.9}$$

When considering figure A.3, the left side of equation (A.5) may be expanded as follows:

$$-\frac{\partial}{\partial r}\left(pr\Delta\theta H\right)\Delta r + pr\Delta\theta\Delta r\frac{\partial H}{\partial r} + p\Delta r\Delta\theta H - \tau_r r\Delta\theta\Delta r - \tau_g r\Delta\theta\Delta r - F_{\text{supports}}\,\Delta r = \frac{\partial}{\partial r}\left(\rho v^2 r\Delta\theta H\right)\Delta r + \frac{\partial}{\partial t}\left(\rho v r\Delta\theta\Delta r H\right) \quad \text{(A.10)}$$

where p is the driving pressure causing the air under the roof of the collector to flow. Furthermore, τ_r and τ_g are the collector roof and ground surface shear stresses respectively acting on the air stream in the control volume. These viscous stresses are assumed to be constant over the radial distance Δr of the control volume. The term F_{supports} is the total drag force per unit radial distance that the roof supports (supporting the glass roof) enforce on the air stream in the specified control volume.

Applying the differential operator to the first term on the left-hand-side of equation (A.10):

$$-\frac{\partial}{\partial r}\left(pr\Delta\theta H\right)\Delta r = -pr\Delta\theta\Delta r\frac{\partial H}{\partial r} - p\Delta r\Delta\theta H - Hr\Delta\theta\Delta r\frac{\partial p}{\partial r} \quad \text{(A.11)}$$

Substitute equation (A.11) into equation (A.10), simplify, divide by $r\Delta\theta\Delta r$ and find

$$-H\frac{\partial p}{\partial r} - \tau_r - \tau_g - \frac{F_{\text{supports}}}{r\Delta\theta} = \frac{1}{r}\frac{\partial}{\partial r}\left(r\rho v^2 H\right) + H\frac{\partial}{\partial t}\left(\rho v\right) \quad \text{(A.12)}$$

By applying the differential operator to the first term on the right-hand-side of equation (A.12) and simplifying, find

$$\frac{1}{r}\frac{\partial}{\partial r}\left(r\rho v^2 H\right) = \frac{v}{r}\frac{\partial}{\partial r}\left(\rho v r H\right) + \rho v H\frac{\partial v}{\partial r} \quad \text{(A.13)}$$

Applying the differential operator to the second term on the right-hand-side of equation (A.12) gives

$$H\frac{\partial}{\partial t}\left(\rho v\right) = \rho H\frac{\partial v}{\partial t} + vH\frac{\partial \rho}{\partial t} \quad \text{(A.14)}$$

Substitute equation (A.3) into equation (A.14) and obtain

$$H\frac{\partial}{\partial t}(\rho v) = \rho H\frac{\partial v}{\partial t} - \frac{v}{r}\frac{\partial}{\partial r}(\rho v r H) \tag{A.15}$$

Substitute equations (A.13) and (A.15) into equation (A.12) and find

$$-\left(H\frac{\partial p}{\partial r} + \tau_r + \tau_g + \frac{F_{\text{supports}}}{r\Delta\theta}\right) = \rho H\left(v\frac{\partial v}{\partial r} + \frac{\partial v}{\partial t}\right) \tag{A.16}$$

During steady state conditions or when transient effects are negligible, equation (A.16) becomes

$$-\left(H\frac{\partial p}{\partial r} + \tau_r + \tau_g + \frac{F_{\text{supports}}}{r\Delta\theta}\right) = \rho v H\frac{\partial v}{\partial r} \tag{A.17}$$

A.1.3 Energy equations

Collector roof

Due to the assumption that the rise in collector height over the length of the radial control volume may be considered to be negligible, the area of the roof exposed to heat flows may be approximated as $r\Delta\theta\Delta r$.

Consider from figure A.4 the following energy balance for the radial control volume for the roof of the collector

$$\begin{aligned} I_h r\Delta\theta\Delta r + q_{gr} r\Delta\theta\Delta r = (\rho_e + \tau_e)\, I_h r\Delta\theta\Delta r + q_{ra} r\Delta\theta\Delta r + q_{rs} r\Delta\theta\Delta r \\ + q_{rh} r\Delta\theta\Delta r + \frac{\partial}{\partial t}(\rho_r r\Delta\theta\Delta r\, t_r c_{pr} T_r) \end{aligned} \tag{A.18}$$

where ρ_r, c_{pr}, and t_r are the density, specific heat capacity and thickness of the roof respectively while T_r is the temperature of the roof.

I_h is the effective solar radiation (beam and diffuse) striking the collector roof, while ρ_e and τ_e represent the effective reflectivity and transmittance of the roof respectively. The term q_{rh} is the convection heat flux from the collector roof to the air underneath it, while q_{gr} represents the radiation heat flux from the ground surface to the roof. Furthermore, q_{ra} and q_{rs} represent the convection heat flux from the roof to the ambient air and the radiation heat flux to the sky respectively. Any temperature gradient across the collector roof is neglected.

The effective solar radiation can be expanded into its beam and diffuse components, I_{hb} and I_{hd} respectively. Similarly, the effective reflectivity and

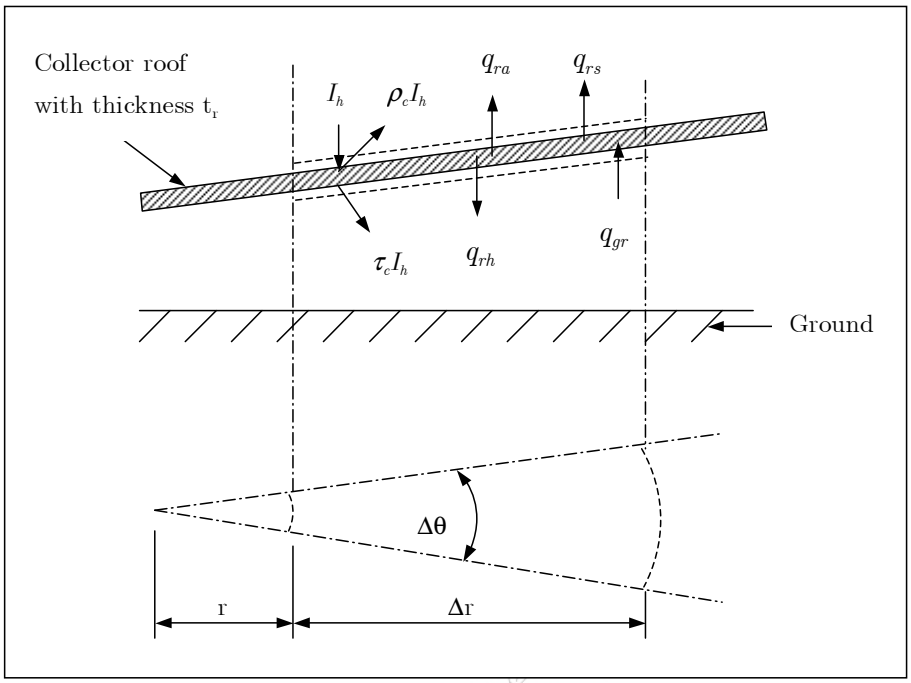

Figure A.4: Conservation of energy applied to a control volume for the roof of the collector

transmittance can also be expanded into the effective beam and effective diffuse components, ρ_{eb} and ρ_{ed} and τ_{eb} and τ_{ed} respectively. Introducing these components into equation (A.18) and dividing by $r\Delta\theta\Delta r$ find

$$I_{hb} + I_{hd} + q_{gr} = (\rho_{eb} + \tau_{eb})\, I_{hb} + (\rho_{ed} + \tau_{ed})\, I_{hd} + q_{ra} + q_{rs} + q_{rh} + \rho_r t_r c_{pr} \frac{\partial T_r}{\partial t} \quad \text{(A.19)}$$

According to Modest (1993), for a transparent medium $\rho_e + \tau_e + \alpha_e = 1$ where α_e is the effective absorptivity of the medium (in this case the collector roof). Therefore, when rearranging equation (A.19) we find

$$\alpha_{eb} I_{hb} + \alpha_{ed} I_{hd} + q_{gr} = q_{ra} + q_{rs} + q_{rh} + \rho_r t_r c_{pr} \frac{\partial T_r}{\partial t} \quad \text{(A.20)}$$

where α_{eb} and α_{ed} are the effective beam and effective diffuse absorptivity components respectively of the effective absorptivity α_e.

During steady state conditions or when transient effects are negligible, equation (A.20) becomes

$$\alpha_{eb} I_{hb} + \alpha_{ed} I_{hd} + q_{gr} = q_{ra} + q_{rs} + q_{rh} \tag{A.21}$$

Ground under collector

From figure A.5 the energy balance at the surface of the ground in the collector can be evaluated as follows

At z = 0 (Ground surface)

Apply an energy balance at the surface of the ground and find

$$\tau_e I_h r\Delta\theta\Delta r = (1-\alpha_g)\,\tau_e I_h r\Delta\theta\Delta r + q_{gr} r\Delta\theta\Delta r + q_g r\Delta\theta\Delta r + q_{gh} r\Delta\theta\Delta r \tag{A.22}$$

where α_g is the absorptivity of the ground in the collector, while q_g is the conduction heat flux from the surface deeper into the ground. The term q_{gh} denotes the convection heat flux from the ground to the air under the collector roof.

Once again, the effective solar radiation I_h and the effective transmittance τ_e can be expanded into their respective beam and diffuse components to give

$$\tau_{eb} I_{hb}\, r\Delta\theta\Delta r + \tau_{ed} I_{hd}\, r\Delta\theta\Delta r = (1-\alpha_g)\,\tau_{eb} I_{hb}\, r\Delta\theta\Delta r + (1-\alpha_g)\,\tau_{ed} I_{hd}\, r\Delta\theta\Delta r + q_{gr} r\Delta\theta\Delta r + q_g r\Delta\theta\Delta r + q_{gh} r\Delta\theta\Delta r \tag{A.23}$$

As seen in figure A.5, some of the radiation that passes through the collector roof and strikes the ground is reflected back to the roof. The reflected radiation is in turn reflected back to the ground. The multiple reflection of diffuse radiation continues, resulting in a slightly higher fraction of energy being absorbed by the ground. This higher fraction of energy is represented by the transmittance-absorptance product ($\tau\alpha$), as discussed in Appendix E.

Upon employing the transmittance-absorptance product, simplifying the equation and expanding the conduction term, we find at z = 0:

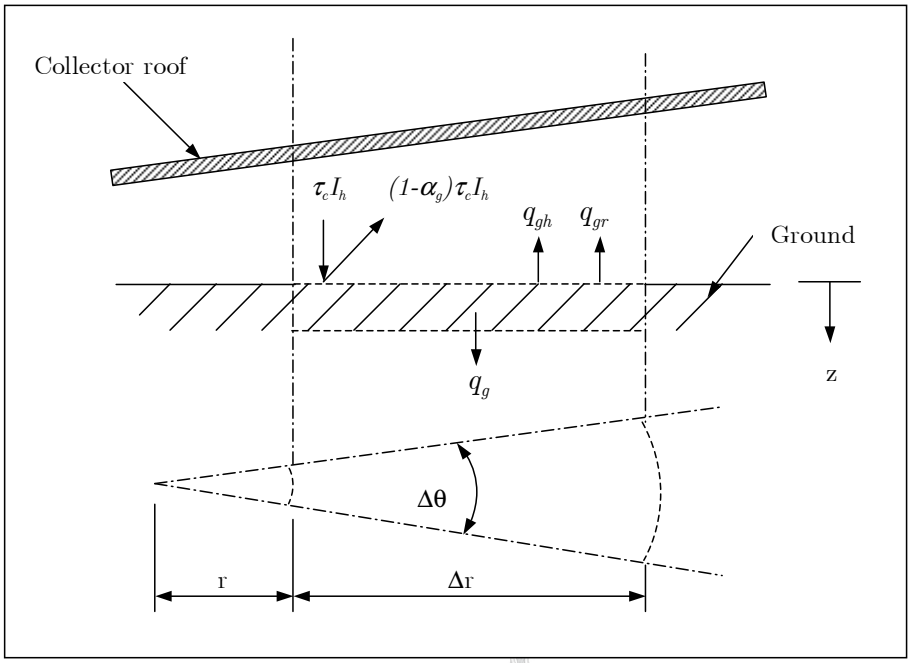

Figure A.5: Conservation of energy applied to a control volume for the ground surface in the collector

$$(\tau_e \alpha_g)_b \, I_{hb} + (\tau_e \alpha_g)_d \, I_{hd} = q_{gr} - k_g \left. \frac{\partial T_g}{\partial z} \right|_{z=0} + q_{gh} \tag{A.24}$$

where k_g and T_g are the thermal conductivity and temperature of the ground respectively.

At $z > 0$

Consider from figure A.6 an energy balance in the ground of the collector

$$q_{g,in} \, r \Delta\theta \Delta r = q_{g,out} \, r \Delta\theta \Delta r + \frac{\partial}{\partial t} \left(\rho_g r \Delta\theta \Delta r \, \Delta z \, c_{pg} T_g \right) \tag{A.25}$$

where ρ_g, c_{pg} and Δz are the ground density, specific heat capacity of the ground and depth of the control volume in the ground of the collector.

When expanding the conduction terms, this equation becomes

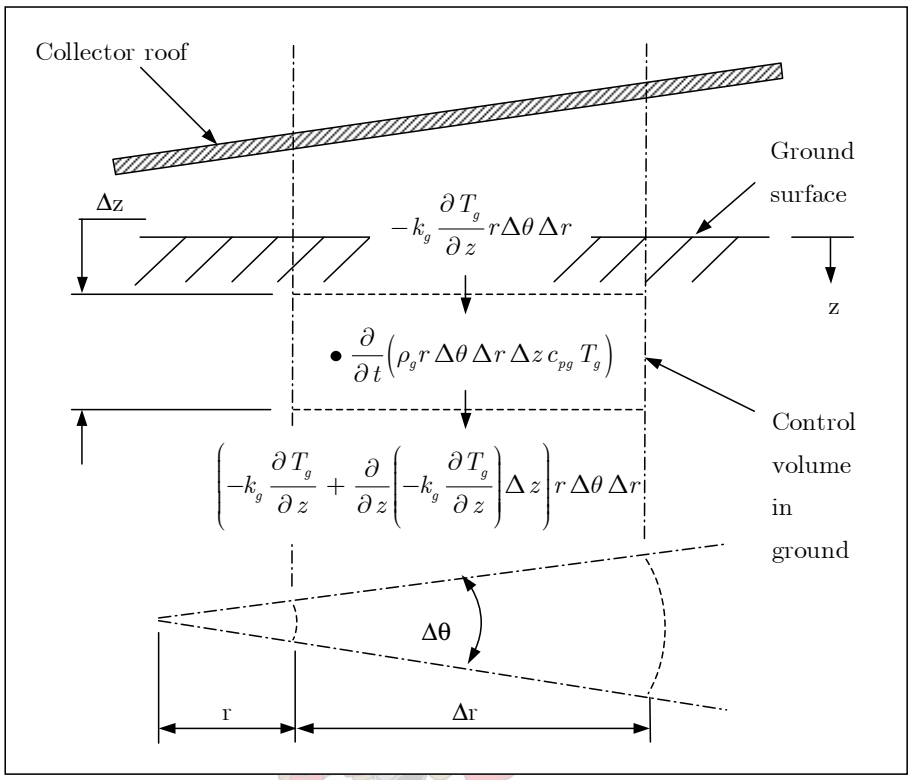

Figure A.6: Conservation of energy applied to a control volume for the ground in the collector

$$-k_g \frac{\partial T_g}{\partial z} r\Delta\theta\Delta r = \left[-k_g \frac{\partial T_g}{\partial z} + \frac{\partial}{\partial z}\left(-k_g \frac{\partial T_g}{\partial z}\right)\Delta z\right] r\Delta\theta\Delta r + \frac{\partial}{\partial t}\left(\rho_g r\Delta\theta\Delta r\,\Delta z\,c_{pg}T_g\right) \quad \text{(A.26)}$$

Dividing equation (A.26) by $r\Delta\theta\Delta r\Delta z$ and assuming the properties of the ground are constant gives

$$-k_g \frac{\partial^2 T_g}{\partial z^2} + \rho_g c_{pg} \frac{\partial T_g}{\partial t} = 0 \quad \text{(A.27)}$$

At $z = \infty$

At a certain depth in the ground the temperature gradient becomes zero and the following boundary condition is valid:

$$\frac{\partial T_g}{\partial z} = 0 \tag{A.28}$$

Air stream in the collector

When regarding the defined control volume in figure A.7, an energy balance relation can be formulated for the air stream between the collector roof and ground in the collector. An order of magnitude analysis performed by Hedderwick (2001) on the collector air stream energy equation concludes that the kinetic energy, radial conduction and transient kinetic energy terms are negligible in comparison with the other energy terms. Neglecting these terms, we find the energy balance

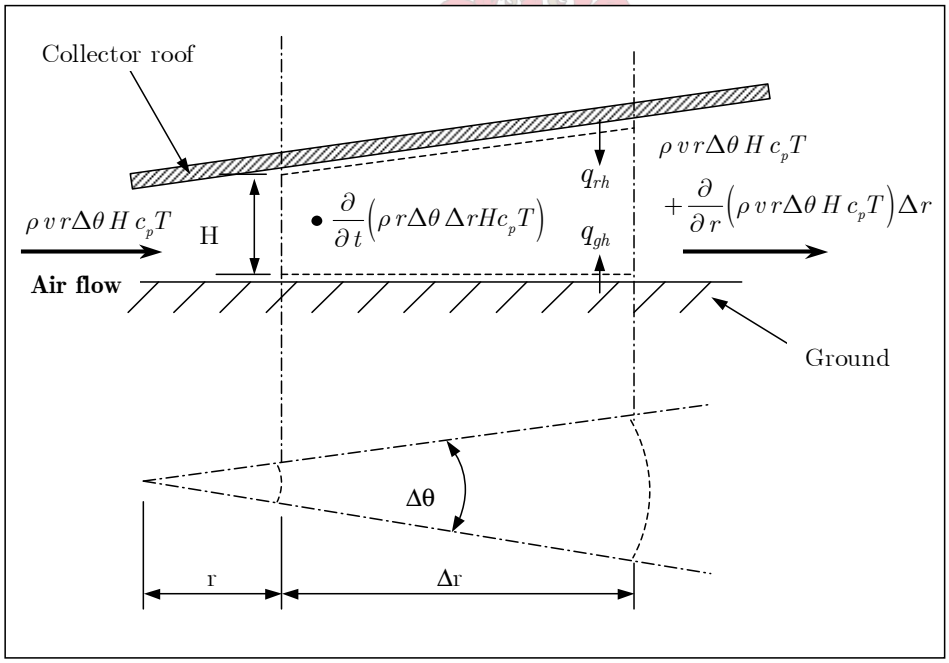

Figure A.7: Conservation of energy applied to a control volume for the air stream in the collector

$$q_{rh} r \Delta\theta \Delta r + q_{gh} r \Delta\theta \Delta r + \rho v r \Delta\theta H c_p T$$
$$= \rho v r \Delta\theta H c_p T + \frac{\partial}{\partial r}\left(\rho v r \Delta\theta H c_p T\right) \Delta r + \frac{\partial}{\partial t}\left(\rho\, r\, \Delta\theta\, \Delta r H c_p T\right) \quad \text{(A.29)}$$

where c_p and T are the specific heat capacity and temperature of the air stream in the collector respectively.

Simplifying equation (A.29) and dividing by $r\Delta\theta\Delta r$ gives

$$q_{rh} + q_{gh} = \frac{1}{r}\frac{\partial}{\partial r}\left(\rho v r H c_p T\right) + H\frac{\partial}{\partial t}\left(\rho c_p T\right) \quad \text{(A.30)}$$

By applying the differential operator to the first term on the right-hand-side of equation (A.30) and simplifying, find

$$\frac{1}{r}\frac{\partial}{\partial r}\left(\rho v r H c_p T\right) = \frac{c_p T}{r}\frac{\partial}{\partial r}\left(\rho v r H\right) + \rho v H \frac{\partial}{\partial r}\left(c_p T\right) \quad \text{(A.31)}$$

Apply the differential operator to the second term on the right-hand-side of equation (A.30) and obtain

$$H\frac{\partial}{\partial t}\left(\rho c_p T\right) = \rho H \frac{\partial}{\partial t}\left(c_p T\right) + c_p T H \frac{\partial \rho}{\partial t} \quad \text{(A.32)}$$

When substituting equation (A.3) into equation (A.32), we obtain the following

$$H\frac{\partial}{\partial t}\left(\rho c_p T\right) = \rho H \frac{\partial}{\partial t}\left(c_p T\right) - \frac{c_p T}{r}\frac{\partial}{\partial r}\left(\rho v r H\right) \quad \text{(A.33)}$$

Now, substituting equation (A.31) and equation (A.33) for the two terms on the right-hand-side of equation (A.30) and simplifying gives the energy equation for the airflow in the collector

$$q_{rh} + q_{gh} = \rho H \left[v\frac{\partial}{\partial r}\left(c_p T\right) + \frac{\partial}{\partial t}\left(c_p T\right)\right] \quad \text{(A.34)}$$

An order of magnitude analysis performed in Appendix B on the tower air stream energy equation concludes that certain terms may be neglected during steady state conditions or when transient effects are negligible. Similarly, equation (A.34) may be reduced to

$$q_{rh} + q_{gh} = \rho v H \frac{\partial}{\partial r}\left(c_p T\right) \quad \text{(A.35)}$$

A.2 Tower

In the following section, the continuity, momentum and energy equation is derived for a defined elementary control volume in the tower of the solar tower power plant. The control volume in the tower is chosen at an arbitrary axial position between the turbine outlet and the tower outlet.

A.2.1 Continuity equation

The continuity equation applicable for essentially one-dimensional flow of air through the elementary control volume shown in figure A.8 is

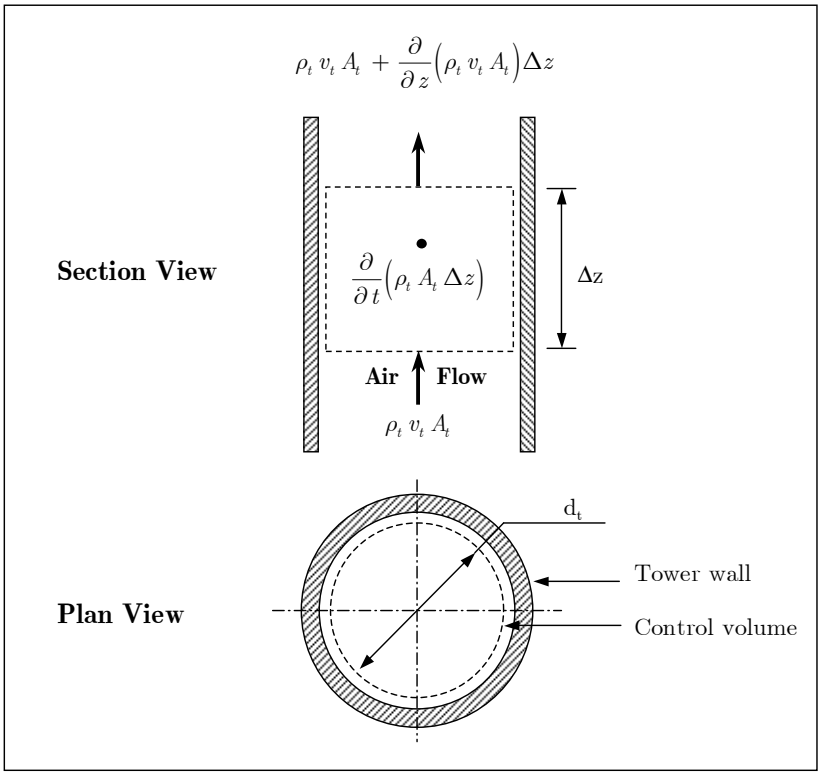

Figure A.8: Conservation of mass applied to a control volume in the tower

$$\rho_t v_t A_t = \rho_t v_t A_t + \frac{\partial}{\partial z}\left(\rho_t v_t A_t\right)\Delta z + \frac{\partial}{\partial t}\left(\rho_t A_t \Delta z\right) \tag{A.36}$$

where ρ_t is the density of the air stream moving through the tower control volume while A_t is the constant tower cross section through which the air

enters or exits the control volume. The variables v_t and Δz denote the axial velocity of the air stream and the axial height of the tower control volume respectively.
Equation (A.36) can be simplified as follows

$$\frac{\partial}{\partial z}\left(\rho_t v_t A_t\right)\Delta z = -\frac{\partial}{\partial t}\left(\rho_t A_t \Delta z\right) \tag{A.37}$$

and when dividing equation (A.37) by $A_t \Delta z$, we find

$$\frac{\partial}{\partial z}\left(\rho_t v_t\right) = -\frac{\partial \rho_t}{\partial t} \tag{A.38}$$

During steady state conditions or when transient effects are negligible, equation (A.38) becomes

$$\frac{\partial}{\partial z}\left(\rho_t v_t\right) = 0 \tag{A.39}$$

A.2.2 Momentum equation

When considering figure A.9 a momentum relation can be formulated for the airflow through a defined control volume in the tower of the solar power plant. When approximating the flow of the air stream through the tower as purely axial, the momentum equation may be expressed as

$$\sum F = -\rho_t {v_t}^2 A_t + \rho_t {v_t}^2 A_t + \frac{\partial}{\partial z}\left(\rho_t {v_t}^2 A_t\right)\Delta z + \frac{\partial}{\partial t}\left(\rho_t v_t A_t \Delta z\right) \tag{A.40}$$

where ΣF represents the sum of the forces acting on the tower control volume.

When regarding figure A.10, the left side of equation (A.40) may be expanded as follows

$$\begin{aligned} p_t A_t - p_t A_t - \frac{\partial}{\partial z}\left(p_t A_t\right)\Delta z - F_{bw}\Delta z - \tau_t\left(\pi d_t \Delta z\right) - \rho_t A_t \Delta z\, g \\ = -\rho_t {v_t}^2 A_t + \rho_t {v_t}^2 A_t + \frac{\partial}{\partial z}\left(\rho_t {v_t}^2 A_t\right)\Delta z + \frac{\partial}{\partial t}\left(\rho_t v_t A_t \Delta z\right) \end{aligned} \tag{A.41}$$

where p is the driving pressure causing the air to flow through the tower and d_t is the inner tower diameter. Furthermore, τ_t is the surface shear stress of the inner tower wall acting on the air column in the control volume. This surface

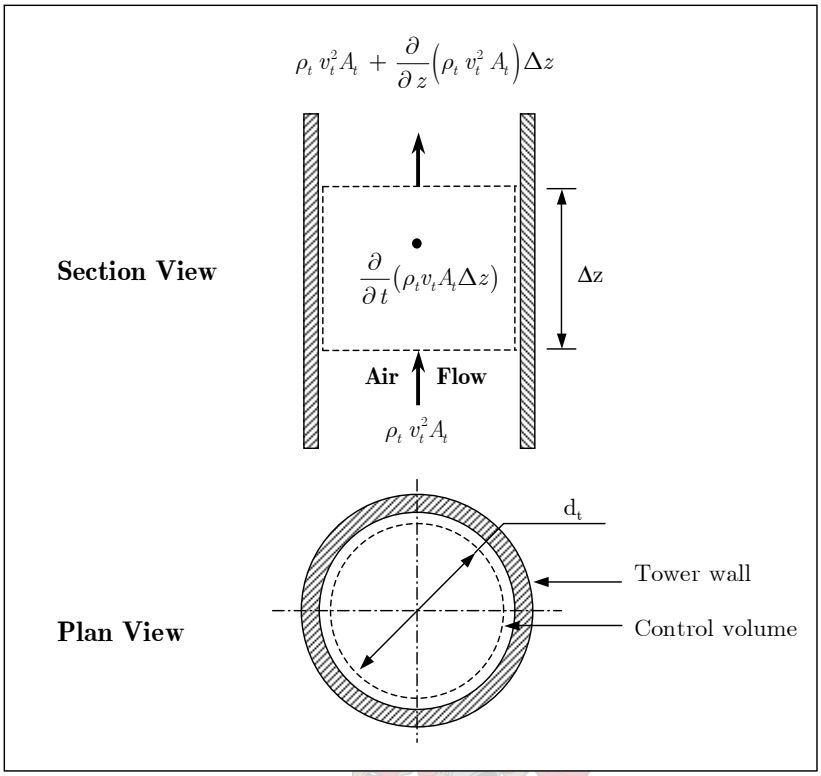

Figure A.9: Conservation of momentum applied to a control volume in the tower

stress is assumed to be constant over the axial distance Δz of the tower control volume. The gravitational constant is denoted by g.

The term F_{bw} is the drag force per unit height of tower that the reinforcements inside the tower, such as bracing rims and spokes, enforce on the air column in the specified control volume. It should be noted that the specific control volume illustrated in figure A.9 and figure A.10 is chosen at an arbitrary axial position inside the tower between the turbine outlet and the top outlet of the tower.

Upon dividing equation (A.41) by $A_t \Delta z$ and simplifying, we find

$$-\frac{\partial p_t}{\partial z} - \frac{\tau_t\, \pi\, d_t}{A_t} - \frac{F_{bw}}{A_t} - \rho_t g = \frac{\partial}{\partial z}\left(\rho_t {v_t}^2\right) + \frac{\partial}{\partial t}\left(\rho_t v_t\right) \tag{A.42}$$

Apply the differential operator to the first term on the right- hand-side of equation (A.42), simplify and find

$$\frac{\partial}{\partial z}\left(\rho_t {v_t}^2\right) = v_t \frac{\partial}{\partial z}\left(\rho_t v_t\right) + \rho_t v_t \frac{\partial v_t}{\partial z} \tag{A.43}$$

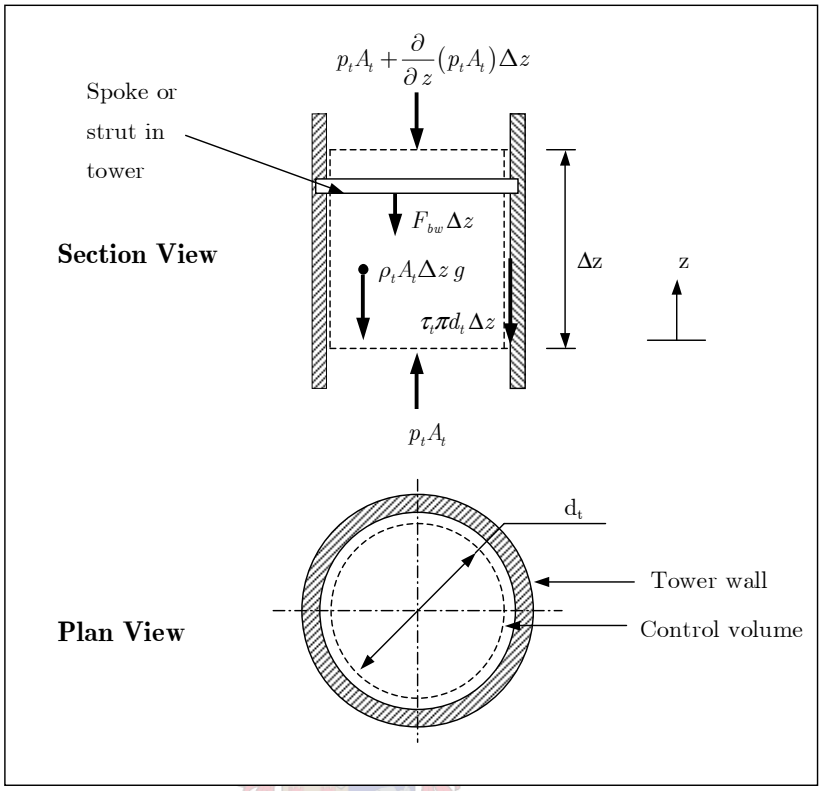

Figure A.10: Forces acting on an air stream control volume in the tower

Applying the differential operator to the second term on the right-hand-side of equation (A.42) gives the expression

$$\frac{\partial}{\partial t}(\rho_t v_t) = v_t \frac{\partial \rho_t}{\partial t} + \rho_t \frac{\partial v_t}{\partial t} \tag{A.44}$$

Substitute equation (A.38) into equation (A.44) and obtain

$$\frac{\partial}{\partial t}(\rho_t v_t) = -v_t \frac{\partial}{\partial z}(\rho_t v_t) + \rho_t \frac{\partial v_t}{\partial t} \tag{A.45}$$

Now, substituting equation (A.43) and equation (A.45) for the two terms on the right-hand-side of equation (A.42) and simplifying gives the momentum equation for the airflow in the tower

$$-\frac{\partial p_t}{\partial z} - \left(\frac{\tau_t\, \pi\, d_t + F_{bw}}{A_t}\right) = \rho_t \left(g + v_t \frac{\partial v_t}{\partial z} + \frac{\partial v_t}{\partial t}\right) \tag{A.46}$$

An order of magnitude analysis performed in Appendix B concludes that during steady state conditions or when transient effects are negligible, equation

(A.46) may be reduced to

$$-\frac{\partial p_t}{\partial z}-\left(\frac{\tau_t\,\pi\,d_t+F_{bw}}{A_t}\right)=\rho_t\left(g+v_t\frac{\partial v_t}{\partial z}\right) \tag{A.47}$$

A.2.3 Energy equation

When regarding the defined control volume in figure A.11, an energy balance relation can be formulated for the air stream in the tower of the power plant. An order of magnitude analysis performed in Appendix B on the tower energy equation concludes that the kinetic energy, radial conduction, friction energy and transient kinetic energy terms are negligible in comparison with the other energy terms. Neglecting these terms give

$$\begin{aligned}\rho_t v_t A_t\,c_{pt}T_t+\rho_t v_t A_t\,g\,z=\rho_t v_t A_t\,c_{pt}T_t+\frac{\partial}{\partial z}\left(\rho_t v_t A_t\,c_{pt}T_t\right)\Delta z\\ +\rho_t v_t A_t\,g\,z+\frac{\partial}{\partial z}\left(\rho_t v_t A_t\,g\,z\right)\Delta z+\frac{\partial}{\partial t}\left(\rho_t A_t\Delta z\,c_{pt}T_t\right)\end{aligned} \tag{A.48}$$

where c_{pt} and T_c are the specific heat capacity and temperature of the air stream in the tower respectively. The letter z now represents the axial height of the control volume in the tower.

Dividing equation (A.48) by $A_c\Delta z$ and simplifying gives

$$\frac{\partial}{\partial z}\left(\rho_t v_t\,c_{pt}T_t\right)+\frac{\partial}{\partial z}\left(\rho_t v_t\,g\,z\right)=-\frac{\partial}{\partial t}\left(\rho_t\,c_{pt}T_t\right) \tag{A.49}$$

Apply the differential operator to the first term on the left-hand-side of equation (A.49), simplify and find

$$\frac{\partial}{\partial z}\left(\rho_t v_t\,c_{pt}T_t\right)=c_{pt}T_t\frac{\partial}{\partial z}\left(\rho_t v_t\right)+\rho_t v_t\frac{\partial}{\partial z}\left(c_{pt}T_t\right) \tag{A.50}$$

When applying the differential operator to the term on the right-hand-side of equation (A.49) we obtain

$$-\frac{\partial}{\partial t}\left(\rho_t c_{pt}T_t\right)=-\rho_t\frac{\partial}{\partial t}\left(c_{pt}T_t\right)-c_{pt}T_t\frac{\partial\rho_t}{\partial t} \tag{A.51}$$

Substituting equation (A.38) into equation (A.51) gives the following relation

$$-\frac{\partial}{\partial t}\left(\rho_t c_{pt}T_t\right)=-\rho_t\frac{\partial}{\partial t}\left(c_{pt}T_t\right)+c_{pt}T_t\frac{\partial}{\partial z}\left(\rho_t v_t\right) \tag{A.52}$$

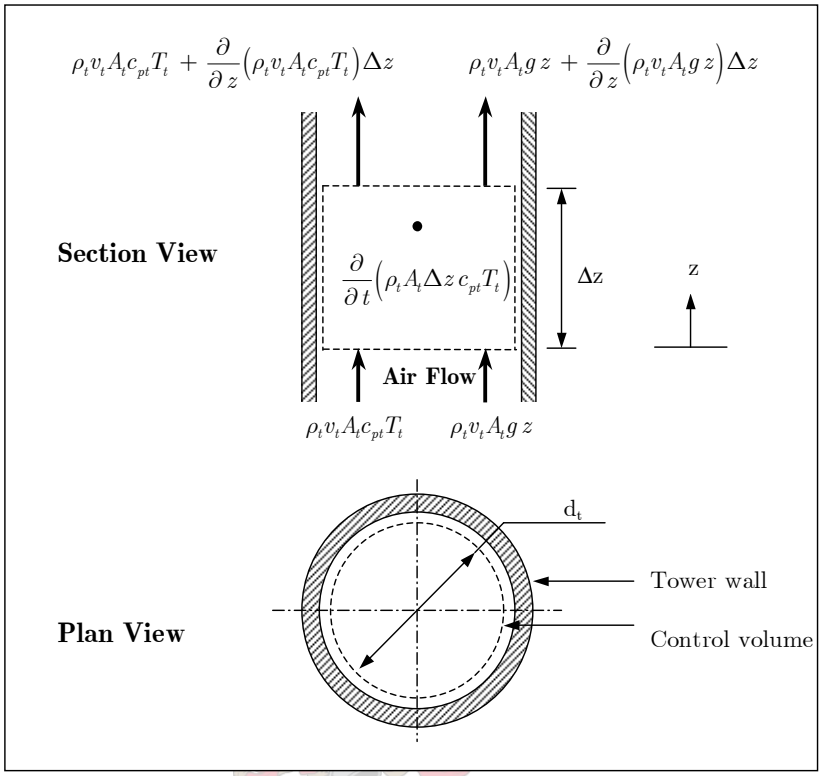

Figure A.11: Conservation of energy applied to a control volume in the tower

Now, when substituting equation (A.50) and equation (A.52) into equation (A.49) and simplifying, we find the energy equation for the airflow in the tower

$$\rho_t \left[v_t \frac{\partial}{\partial z}\left(c_{pt} T_t\right) + \frac{\partial}{\partial t}\left(c_{pt} T_t\right) \right] + \frac{\partial}{\partial z}\left(\rho_t v_t\, g\, z\right) = 0 \tag{A.53}$$

The order of magnitude analysis performed in Appendix B concludes that during steady state conditions or when transient effects are negligible, equation (A.53) reduces to

$$\rho_t v_t \frac{\partial}{\partial z}\left(c_{pt} T_t\right) + \frac{\partial}{\partial z}\left(\rho_t v_t\, g\, z\right) = 0 \tag{A.54}$$

Appendix B

Order of Magnitude Analysis

This section contains an order of magnitude analysis performed on the air stream momentum and energy equation in the tower of the solar power plant. The purpose of this evaluation is to determine which terms in these equations are negligible because of their small contribution to the respective total momentum and total energy flux.

The analysis is performed for two cases. Firstly, only the reaction of the solar tower power plant to the environmental conditions is evaluated. In a later section, the effects of a controlled flow through the solar tower power plant is also investigated. In an attempt to deal with fluctuating electricity demand, the second case simulates controlling the flow through the system to produce energy as dictated by demand.

It should be noted that the calculated figures given in the text are rounded off as appropriate for clarity.

In order to perform an order of magnitude analysis, certain conditions have to be assumed at the inlet and outlet of the control volume. The tower dimensions employed are those of the reference plant shown in figure 1.1.

Table B.1 displays the chosen dimensions and inlet conditions, where the subscripts ti or i represent the inlet and to or o refer to the outlet of the tower control volume, while d_t denotes the tower diameter.

The outlet temperature and pressure of the tower control volume is found using relations given in Kröger (2004), where z is defined as the elevation above a certain reference level. Assuming a dry adiabatic lapse rate (DALR) inside the tower, find

Table B.1: Dimensions and chosen inlet conditions

z_i	100 m
z_o	101 m
T_{ti}	323.15 K
v_{ti}	15 m/s
p_{ti}	90000 N/m^2
d_t	160 m

$$T_{to} = T_{ti} - 0.00975\,z = 323.15 - 0.00975(1) = 323.14025 \text{ K} \tag{B.1}$$

and

$$\begin{aligned} p_{to} = p_{ti}\left(1 - \frac{0.00975\,z}{T_{ti}}\right)^{3.5} &= 90000\left(1 - \frac{0.00975(1)}{323.15}\right)^{3.5} \\ &= 89990.49626 \text{ N/m}^2 \end{aligned} \tag{B.2}$$

The air density inside the tower is determined using the perfect gas law

$$\rho_{ti} = \frac{p_{ti}}{R\,T_{ti}} = \frac{90000}{(287.08)(323.15)} = 0.97014 \text{ kg/m}^3 \tag{B.3}$$

$$\rho_{to} = \frac{p_{to}}{R\,T_{to}} = \frac{89990.49626}{(287.08)(323.14025)} = 0.970069 \text{ kg/m}^3 \tag{B.4}$$

The specific heat capacity, dynamic viscosity and thermal conductivity at the inlet and outlet of the tower control volume is calculated using relations as specified in Kröger (2004)

$$\begin{aligned} c_{pti} &= 1.045356{\times}10^3 \ - 3.161783{\times}10^{-1}\ T_{ti} \\ &\quad + 7.083814{\times}10^{-4}\ {T_{ti}}^2 - 2.705209{\times}10^{-7}\ {T_{ti}}^3 \\ &= 1.045356{\times}10^3 \ - 3.161783{\times}10^{-1}\ (323.15) \\ &\quad + 7.083814{\times}10^{-4}\ (323.15)^2 - 2.705209{\times}10^{-7}\ (323.15)^3 \\ &= 1008.027572 \text{ J/kg·K} \end{aligned} \tag{B.5}$$

$$
\begin{aligned}
c_{pto} &= 1.045356\times10^{3} \; - 3.161783\times10^{-1}\; T_{to} \\
&\quad + 7.083814\times10^{-4}\; {T_{to}}^{2} - 2.705209\times10^{-7}\; {T_{to}}^{3} \\
&= 1.045356\times10^{3} \; - 3.161783\times10^{-1}\; (323.14025) \\
&\quad + 7.083814\times10^{-4}\; (323.14025)^{2} - 2.705209\times10^{-7}\; (323.14025)^{3} \\
&= 1008.027017 \text{ J/kg·K}
\end{aligned}
\tag{B.6}
$$

$$
\begin{aligned}
\mu_{ti} &= 2.287973\times10^{-6} \; + 6.259793\times10^{-8}\; T_{ti} \\
&\quad - 3.131956\times10^{-11}\; {T_{ti}}^{2} + 8.15038\times10^{-15}\; {T_{ti}}^{3} \\
&= 2.287973\times10^{-6} \; + 6.259793\times10^{-8}\; (323.15) \\
&\quad - 3.131956\times10^{-11}\; (323.15)^{2} + 8.15038\times10^{-15}\; (323.15)^{3} \\
&= 1.95209566\times10^{-5} \text{ kg/m·s}
\end{aligned}
\tag{B.7}
$$

$$
\begin{aligned}
\mu_{to} &= 2.287973\times10^{-6} \; + 6.259793\times10^{-8}\; T_{to} \\
&\quad - 3.131956\times10^{-11}\; {T_{to}}^{2} + 8.15038\times10^{-15}\; {T_{to}}^{3} \\
&= 2.287973\times10^{-6} \; + 6.259793\times10^{-8}\; (323.14025) \\
&\quad - 3.131956\times10^{-11}\; (323.14025)^{2} + 8.15038\times10^{-15}\; (323.14025)^{3} \\
&= 1.95205188\times10^{-5} \text{ kg/m·s}
\end{aligned}
\tag{B.8}
$$

$$
\begin{aligned}
k_{ti} &= -4.937787\times10^{-4} \; + 1.018087\times10^{-4}\; T_{ti} - 4.627937\times10^{-8}\; {T_{ti}}^{2} \\
&\quad + 1.250603\times10^{-11}\; {T_{ti}}^{3} \\
&= -4.937787\times10^{-4} \; + 1.018087\times10^{-4}\; (323.15) \\
&\quad - 4.627937\times10^{-8}\; (323.15)^{2} + 1.250603\times10^{-11}\; (323.15)^{3} \\
&= 0.027995 \text{ W/m·K}
\end{aligned}
\tag{B.9}
$$

$$\begin{aligned} k_{to} &= -4.937787\times10^{-4} + 1.018087\times10^{-4}\ T_{to} - 4.627937\times10^{-8}\ {T_{to}}^2 \\ &\quad + 1.250603\times10^{-11}\ {T_{to}}^3 \\ &= -4.937787\times10^{-4} + 1.018087\times10^{-4}\ (323.14025) \\ &\quad - 4.627937\times10^{-8}\ (323.14025)^2 + 1.250603\times10^{-11}\ (323.14025)^3 \\ &= 0.02799422\ \text{W/m·K} \end{aligned} \tag{B.10}$$

The mass flow at the inlet to the control volume is determined by

$$\dot{m}_{ti} = \rho_{ti}\, v_{ti}\, A_t = (0.97014)(15)(\pi(80)^2) = 292588.0048\ \text{kg/s} \tag{B.11}$$

By approximating the mass flow over the defined control volume as constant, the velocity at the outlet of the control volume may be calculated by

$$v_{to} = \frac{\dot{m}}{\rho_{to} A_t} = \frac{292588.0048}{(0.970069)(\pi(80)^2)} = 15.0011\ \text{m/s} \tag{B.12}$$

Average values for air stream density, velocity and dynamic viscosity in the tower control volume are approximated by

$$\rho_t = \frac{1}{2}(\rho_{ti} + \rho_{to}) = \frac{1}{2}(0.97014 + 0.970069) = 0.9701056\ \text{kg/m}^3 \tag{B.13}$$

$$v_t = \frac{1}{2}(v_{ti} + v_{to}) = \frac{1}{2}(15 + 15.0011) = 15.000566\ \text{m/s} \tag{B.14}$$

$$\begin{aligned} \mu_t = \frac{1}{2}(\mu_{ti} + \mu_{to}) &= \frac{1}{2}(1.95209566\times10^{-5} + 1.95205188\times10^{-5}) \\ &= 1.9520738\times10^{-5}\ \text{kg/m·s} \end{aligned} \tag{B.15}$$

Using these average values, find the average tower air stream Reynolds number

$$Re_t = \frac{\rho_t v_t d_t}{\mu_t} = \frac{(0.9701056)(15.000566)(160)}{1.9520738\times10^{-5}} = 119275275.4 \tag{B.16}$$

An article published by Von Backström *et al.* (2003) discusses the frictional losses and reinforcement structure losses inside the tower. Experiments conducted on a model tower, using bracing wheels as tower reinforcements, find experimental values for the Darcy friction factor and bracing wheel pressure loss coefficient.

Due to a developing flow in the tower, a higher value for the friction factor is found than when using the equation given by Haaland (1983) for fully developed flow. For this analysis, a surface roughness of $\varepsilon_t = 0.002$ m will be assumed for the inside of the concrete tower, (as in the article by Von Backström *et al.* (2003)) and the friction factor determined using the equation by Haaland (1983)

$$\begin{aligned} f_t &= 2.7778 \left[log \left(\left(\frac{7.7}{Re_t} \right)^3 + \left(\frac{\varepsilon_t}{3.75\, d_t} \right)^{3.33} \right) \right]^{-2} \\ &= 2.7778 \left[log \left(\left(\frac{7.7}{119275275.4} \right)^3 + \left(\frac{0.002}{(3.75)(160)} \right)^{3.33} \right) \right]^{-2} \\ &= 0.0083506 \end{aligned} \tag{B.17}$$

The wall shear stress can now be approximated as follows

$$\begin{aligned} \tau_t = \frac{1}{8} f_t \rho_t {v_t}^2 &= \frac{1}{8}(0.0083506)(0.9701056)(15.000566)^2 \\ &= 0.2278567 \text{ N/m}^2 \end{aligned} \tag{B.18}$$

In view of the experimental results found by Von Backström *et al.* (2003), a very conservative value of $K_{bw} = 0.1$ is assumed as first approximation for the bracing wheel pressure loss coefficient. Furthermore, it is assumed that 10 evenly spaced bracing wheels are used as internal tower reinforcements.

The total bracing wheel force per unit height on the tower air stream is then calculated, based on the inlet dynamic pressure

$$
\begin{aligned}
F_{bw} &= \frac{(A_t K_{bw} \frac{1}{2} \rho_{ti} {v_{ti}}^2)(n_{bw})}{H_t} \\
&= \frac{(\pi(80)^2)(0.1)(\frac{1}{2})(0.97014)(15)^2(10)}{1500} \\
&= 1462.94 \text{ N/m}
\end{aligned} \tag{B.19}
$$

where n_{bw} is the number of bracing wheels and H_t is the tower height.

The transient terms of the tower momentum and energy equation represent a change of conditions in the tower control volume itself over a period of time. When dealing with these transient terms, some additional assumptions have to be made.

The initial inlet conditions and the tower and control volume dimensions are assumed the same as before, while the transient terms are evaluated at the center of the tower control volume (at a height of 100.5 m) over a period of 1 minute.

Now, new inlet conditions have to be assumed for the next time step. From the results of a numerical model developed by Hedderwick (2001), average temperature and mass flow differences are determined, as shown in table B.2 and B.3.

Table B.2: Numerical temperature data of Hedderwick (2001) used for determining new inlet temperature

Time	*Air Temperature* [K]	*Absolute difference between hours* [K]
12:00	315.253	
		1.533
13:00	316.786	
		0.502
14:00	317.288	
		0.324
15:00	316.964	

The temperature and mass flow data taken from the numerical results of Hedderwick (2001) are specifically chosen to be of approximately the same magnitude as the assumed initial inlet conditions. It should also be noted that the numerical model of Hedderwick (2001) only considers the collector of the

Table B.3: Numerical mass flow data of Hedderwick (2001) used for determining new inlet mass flow

Time	*Mass Flow* [kg/s]	*Absolute difference between hours* [kg/s]
12:00	246098.7	
		3816.8
13:00	249915.5	
		973.9
14:00	250889.4	
		3881.4
15:00	247008	

solar tower power plant. Therefore, the numerical data used in this analysis is taken at the nearest collector radius to the tower.

From the data given in table B.2, the average temperature difference per minute is calculated as follows

$$\Delta T = \frac{(1.533 + 0.502 + 0.324)}{(3)(60)} = 0.0131056 \text{ K/min} \tag{B.20}$$

while from table B.3 the average mass flow difference per minute is determined similarly by

$$\Delta \dot{m} = \frac{(3816.8 + 973.9 + 3881.4)}{(3)(60)} = 48.1783 \text{ (kg/s)/min} \tag{B.21}$$

By adding these average differences to the initial inlet conditions, new inlet conditions are approximated. table B.4 displays the initial and new conditions assumed at the tower control volume inlet. The subscript ci, old indicates the initial tower inlet conditions while ci, new refers to the inlet conditions after a time step of 1 minute.

Table B.4: Initial and new inlet conditions for evaluating transient terms

$T_{ti,\,old}$	323.15 K
$\dot{m}_{ti,\,old}$	292588.0048 kg/s
$T_{ti,\,new}$	323.1631 K
$\dot{m}_{ti,\,new}$	292636.1831 kg/s
p_{ti}	90000 N/m^2

Employing the DALR assumption inside the tower and using the relations in Kröger (2004) yields

$$\begin{aligned} T_{cr,\,old} = T_{ti,\,old} - 0.00975\,z &= 323.15 - 0.00975(0.5) \\ &= 323.145125 \text{ K} \end{aligned} \tag{B.22}$$

$$\begin{aligned} T_{cr,\,new} = T_{ti,\,new} - 0.00975\,z &= 323.1631 - 0.00975(0.5) \\ &= 323.15823 \text{ K} \end{aligned} \tag{B.23}$$

$$\begin{aligned} p_{cr,\,old} = p_{ti}\left(1 - \frac{0.00975\,z}{T_{ti,\,old}}\right)^{3.5} &= 90000\left(1 - \frac{0.00975(0.5)}{323.15}\right)^{3.5} \\ &= 89995.24804 \text{ N/m}^2 \end{aligned} \tag{B.24}$$

$$\begin{aligned} p_{cr,\,new} = p_{ti}\left(1 - \frac{0.00975\,z}{T_{ti,\,new}}\right)^{3.5} &= 90000\left(1 - \frac{0.00975(0.5)}{323.1631}\right)^{3.5} \\ &= 89995.24823 \text{ N/m}^2 \end{aligned} \tag{B.25}$$

where the subscripts cr, old and cr, new represent the initial and new conditions at the center of the control volume.

The initial and new values for air density at the center of the tower control volume is determined using the perfect gas law

$$\rho_{cr,\,old} = \frac{p_{cr,\,old}}{R\,T_{cr,\,old}} = \frac{89995.24804}{(287.08)(323.145125)} = 0.9701056 \text{ kg/m}^3 \tag{B.26}$$

$$\rho_{cr,\,new} = \frac{p_{cr,\,new}}{R\,T_{cr,\,new}} = \frac{89995.24823}{(287.08)(323.15823)} = 0.9700663 \text{ kg/m}^3 \tag{B.27}$$

From the relations given in Kröger (2004), the initial and new specific heat capacity values at the center of the control volume are found as follows

$$\begin{aligned} c_{pcr,\,old} &= 1.045356{\times}10^{3} \; - 3.161783{\times}10^{-1}\; T_{cr,\,old} \\ &\quad + 7.083814{\times}10^{-4}\; {T_{cr,\,old}}^{2} - 2.705209{\times}10^{-7}\; {T_{cr,\,old}}^{3} \\ &= 1.045356{\times}10^{3} \; - 3.161783{\times}10^{-1}\; (323.145125) \\ &\quad + 7.083814{\times}10^{-4}\; (323.145125)^{2} - 2.705209{\times}10^{-7}\; (323.145125)^{3} \\ &= 1008.027294 \text{ J/kg·K} \end{aligned} \tag{B.28}$$

$$\begin{aligned} c_{pcr,\,new} &= 1.045356{\times}10^{3} \; - 3.161783{\times}10^{-1}\; T_{cr,\,new} \\ &\quad + 7.083814{\times}10^{-4}\; {T_{cr,\,new}}^{2} - 2.705209{\times}10^{-7}\; {T_{cr,\,new}}^{3} \\ &= 1.045356{\times}10^{3} \; - 3.161783{\times}10^{-1}\; (323.15823) \\ &\quad + 7.083814{\times}10^{-4}\; (323.15823)^{2} - 2.705209{\times}10^{-7}\; (323.15823)^{3} \\ &= 1008.02804 \text{ J/kg·K} \end{aligned} \tag{B.29}$$

Once again, by approximating the mass flow through the control volume as constant for a specific time step, the initial and new tower air stream velocities at the center of the tower control volume are calculated by

$$v_{cr,\,old} = \frac{\dot{m}_{old}}{\rho_{cr,\,old} A_t} = \frac{292588.0048}{(0.9701056)(\pi(80)^2)} = 15.000566 \text{ m/s} \tag{B.30}$$

$$v_{cr,\,new} = \frac{\dot{m}_{new}}{\rho_{cr,\,new} A_t} = \frac{292636.1831}{(0.9700663)(\pi(80)^2)} = 15.003644 \text{ m/s} \tag{B.31}$$

Tower momentum equation

Consider the momentum equation for the tower of the solar tower power plant as derived in Appendix A

$$-\frac{\partial p}{\partial z} - \left(\frac{\tau_t \, \pi \, d_t + F_{bw}}{A_t} \right) = \rho_t \left(g + v_t \frac{\partial v_t}{\partial z} + \frac{\partial v_t}{\partial t} \right) \tag{B.32}$$

Approximating the first (axial pressure difference) term of equation (B.32) gives

$$-\frac{(p_{to}-p_{ti})}{(z_o-z_i)} = -\frac{(89990.49626-90000)}{(101-100)} = 9.5037418 \text{ N/m}^3 \tag{B.33}$$

Regarding the second (wall friction) term on the left side of equation (B.32), we find

$$-\frac{\tau_t \pi d_t}{A_t} = -\frac{(0.2278567)(\pi)(160)}{(\pi(80)^2)} = -0.005696417 \text{ N/m}^3 \tag{B.34}$$

The third (bracing wheel force) term of equation (B.32) is evaluated as follows

$$-\frac{F_{bw}}{A_t} = -\frac{1462.94}{(\pi(80)^2)} = -0.072760668 \text{ N/m}^3 \tag{B.35}$$

Consider the fourth (gravity force) term of equation (B.32) and find

$$\rho_t g = (0.9701056)(9.8) = 9.507035336 \text{ N/m}^3 \tag{B.36}$$

The magnitude of the fifth (axial momentum) term of equation (B.32) is approximated by

$$\begin{aligned}\rho_t v_t \frac{(v_{to}-v_{ti})}{(z_o-z_i)} &= (0.9701056)(15.000566)\frac{(15.0011-15)}{(101-100)} \\ &= 0.016465743 \text{ N/m}^3\end{aligned} \tag{B.37}$$

Employing the assumptions for transient terms, the sixth (transient momentum) term of equation (B.32) can be approximated as follows

$$\begin{aligned}&\rho_{cr,\,avg}\frac{(v_{cr,\,new}-v_{cr,\,old})}{\Delta t} \\ &= \frac{(0.9701056+0.9700663)}{2}\left(\frac{(15.003644-15.000566)}{60}\right) \\ &= 0.000049773 \text{ N/m}^3\end{aligned} \tag{B.38}$$

where $\rho_{cr,\,avg}$ is the average air density of the two time steps at the center of the tower control volume.

When comparing the various terms of the tower momentum equation, it is clear (from equation (B.36)) that the gravity force term is the greatest in magnitude. In order to determine which terms of the momentum equation can be considered negligible, compare the absolute values of the other terms with the gravity force term, as shown in table B.5.

Table B.5: Comparison between the magnitude of the various terms in the tower momentum equation

Term	*Absolute Magnitude* [N/m^3]	*Percentage of Gravity Force term* [%]
Gravity Force	9.507035336	100
Axial Pressure Difference	9.5037418	99.965
Wall Friction	0.005696417	0.0599
Bracing Wheel Force	0.072760668	0.765
Axial Momentum	0.016465743	0.173
Transient Momentum	0.000049773	0.000523

When considering table B.5, we find that the gravity force and axial pressure difference terms are of the same order. The right-hand column gives an indication of the extremely small contribution made by the transient momentum term to the total momentum flux, at less than 0.0006 % of the magnitude of the gravity force term. The wall friction and axial momentum terms are also small in magnitude, having respective magnitudes of approximately 0.06 % and 0.2 % of the gravity force term. The bracing wheel force term has a slightly larger magnitude at almost 0.8 % of the gravity force term.

It is, however, very important to note that the magnitude of these terms should in actual fact be compared as terms in the tower draught equation. The driving potential causing the air to flow through the plant is given by the pressure difference due to a column of cold air outside the tower and a column of hot air inside the tower. This means that the axial pressure difference and gravity force terms of the tower momentum equation will be approximately an order smaller, due to now evaluating these terms as difference terms between the air inside and outside the tower. The magnitude of the other terms

of the tower momentum equation stay the same, and thus, compared to the smaller magnitude of the gravity force term, will now be an order larger. This causes the bracing wheel force and axial momentum terms to have magnitudes greater than 1 % of the gravity force term, and thus are not considered negligible. Due to some uncertainty concerning an assumed roughness value for the inside surface of the tower, the wall friction term will not be considered to be negligible.

Therefore, it is assumed that only the transient momentum term may be neglected when evaluating the tower air stream momentum equation.

Tower energy equation

When regarding the defined control volume in figure B.1, the following energy balance can be formulated for the air stream in the tower of the power plant:

$$\begin{aligned}
&\rho_t v_t A_t\, c_{pt} T_t + \rho_t v_t A_t\, g\, z + \frac{1}{2}\,\rho_t {v_t}^3 A_t - k_t A_t \frac{\partial T_t}{\partial z} \\
&= \rho_t v_t A_t\, c_{pt} T_t + \frac{\partial}{\partial z}\left(\rho_t v_t A_t\, c_{pt} T_t\right)\Delta z + \rho_t v_t A_t\, g\, z + \frac{\partial}{\partial z}\left(\rho_t v_t A_t\, g\, z\right)\Delta z \\
&+ \frac{1}{2}\,\rho_t {v_t}^3 A_t + \frac{\partial}{\partial z}\left(\frac{1}{2}\,\rho_t {v_t}^3 A_t\right)\Delta z - k_t A_t \frac{\partial T_t}{\partial z} + \frac{\partial}{\partial z}\left(-k_t A_t \frac{\partial T_t}{\partial z}\right)\Delta z \\
&- F_{drag}\Delta z\, v_t + \frac{\partial}{\partial t}\left(\rho_t A_t \Delta z\, c_{pt} T_t + \frac{1}{2}\,\rho_t A_t \Delta z\, {v_t}^2\right)
\end{aligned} \tag{B.39}$$

where ρ_t, v_t, T_t, c_{pt} and k_t are the density, velocity, temperature, specific heat capacity and thermal conductivity of the air steam in the tower respectively, while the cross-sectional area and axial height of the tower control volume are represented respectively by A_t and z. The term $F_{drag}\Delta z\, v_t$ of equation (B.39) represents the energy loss due to friction in the tower, where F_{drag} is the combined wall friction and bracing wheel drag force per unit tower height and v_t is the average air stream velocity in the tower control volume.

Simplifying equation (B.39) gives

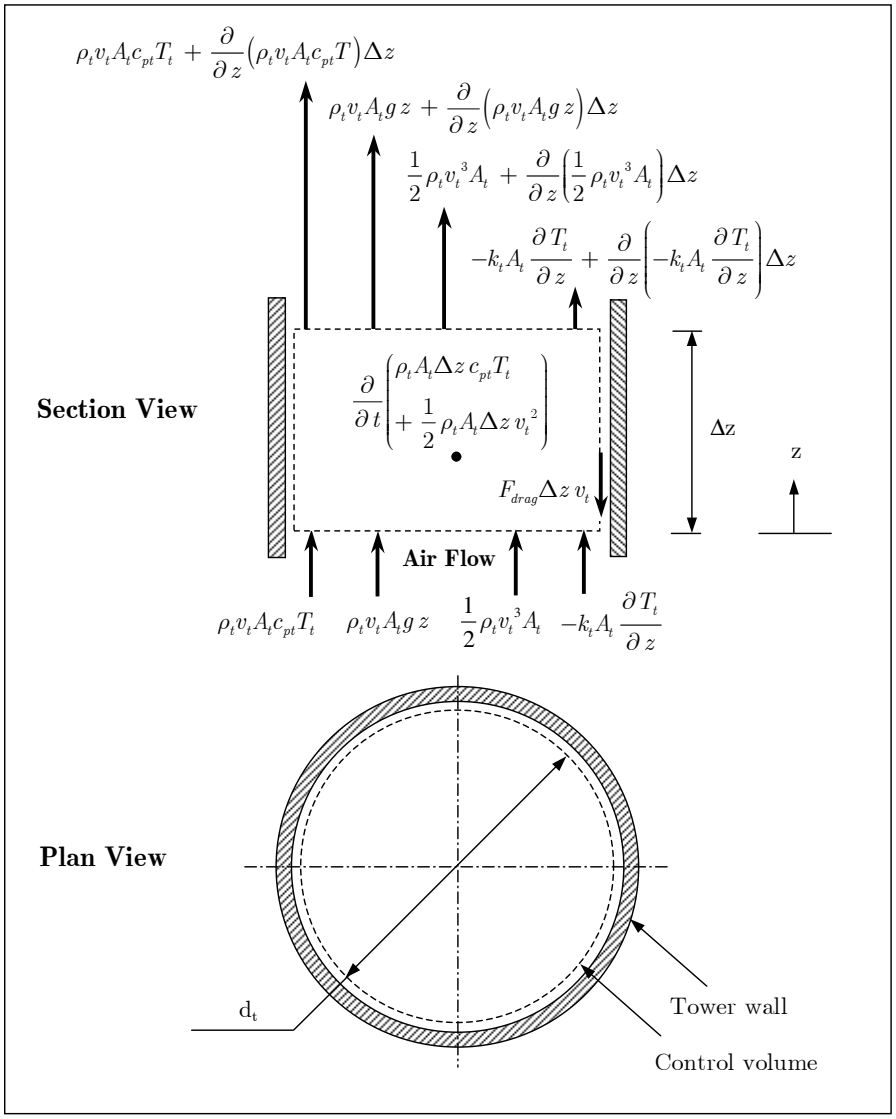

Figure B.1: Conservation of energy applied to a control volume in the tower

$$\frac{\partial}{\partial z}\left(\rho_t v_t A_t\, c_{pt} T_t\right)\Delta z + \frac{\partial}{\partial z}\left(\rho_t v_t A_t\, g\, z\right)\Delta z + \frac{\partial}{\partial z}\left(\frac{1}{2}\,\rho_t {v_t}^3 A_t\right)\Delta z + \frac{\partial}{\partial z}\left(-k_t A_t \frac{\partial T_t}{\partial z}\right)\Delta z - F_{drag}\Delta z\, v_t + \frac{\partial}{\partial t}\left(\rho_t A_t \Delta z\, c_{pt} T_t + \frac{1}{2}\,\rho_t A_t \Delta z\, {v_t}^2\right) = 0 \quad \text{(B.40)}$$

When considering the magnitude of the first five terms of equation (B.40), the same assumptions, inlet and outlet conditions apply as those enforced for the evaluation of the non-transient terms of the tower momentum equation.

The first (enthalpy) term of equation (B.40) can be approximated as follows

$$\begin{aligned}
&\left[\frac{(\rho_t v_t A_t c_{pt} T_t)_o - (\rho_t v_t A_t c_{pt} T_t)_i}{z_o - z_i}\right]\Delta z \\
&= \left[\frac{(\rho_t v_t A_t c_{pt} T_t)_o}{z_o - z_i}\right]\Delta z - \left[\frac{(\rho_t v_t A_t c_{pt} T_t)_i}{z_o - z_i}\right]\Delta z \\
&= \left[\frac{(0.970069)(15.0011)(\pi(80)^2)(1008.027017)(323.14025)}{101-100}\right](1) \\
&\quad - \left[\frac{(0.97014)(15)(\pi(80)^2)(1008.027572)(323.15)}{101-100}\right](1) \\
&= -2928082.23 \text{ W}
\end{aligned} \tag{B.41}$$

where the negative sign indicates a decrease in enthalpy over the control volume.

The magnitude of the second (potential energy) term of equation (B.40) is evaluated as follows

$$\begin{aligned}
&\left[\frac{(\rho_t v_t A_t\, g\, z)_o - (\rho_t v_t A_t\, g\, z)_i}{z_o - z_i}\right]\Delta z \\
&= \left[\frac{(\rho_t v_t A_t\, g\, z)_o}{z_o - z_i}\right]\Delta z - \left[\frac{(\rho_t v_t A_t\, g\, z)_i}{z_o - z_i}\right]\Delta z \\
&= \left[\frac{(0.970069)(15.0011)(\pi(80)^2)(9.8)(101)}{101-100}\right](1) \\
&\quad - \left[\frac{(0.97014)(15)(\pi(80)^2)(9.8)(100)}{101-100}\right](1) \\
&= 2867362.45 \text{ W}
\end{aligned} \tag{B.42}$$

which indicates an increase in potential energy as the air rises through the tower control volume.

Regarding the third (kinetic energy) term of equation (B.40), we find

$$
\begin{aligned}
&\left[\frac{(\frac{1}{2}\rho_t {v_t}^3 A_t)_o - (\frac{1}{2}\rho_t {v_t}^3 A_t)_i}{z_o - z_i}\right]\Delta z \\
&= \left[\frac{\left(\frac{1}{2}\rho_t {v_t}^3 A_t\right)_o}{z_o - z_i}\right]\Delta z - \left[\frac{\left(\frac{1}{2}\rho_t {v_t}^3 A_t\right)_i}{z_o - z_i}\right]\Delta z \\
&= \left[\frac{\frac{1}{2}(0.970069)(15.0011)^3(\pi(80)^2)}{101-100}\right](1) - \left[\frac{\frac{1}{2}(0.97014)(15)^3(\pi(80)^2)}{101-100}\right](1) \\
&= 4966.138 \text{ W}
\end{aligned}
\tag{B.43}
$$

where the positive sign signifies a kinetic energy increase over the defined control volume.

Taking into account that the DALR assumption implies a constant axial temperature gradient in the tower, we consider the fourth (axial conduction) term of equation (B.40) and find

$$
\begin{aligned}
&\left[\frac{(-k_t A_t \frac{\partial T_t}{\partial z})_o - (-k_t A_t \frac{\partial T_t}{\partial z})_i}{z_o - z_i}\right]\Delta z \\
&= \left[\frac{\left(-k_t A_t \frac{\partial T_t}{\partial z}\right)_o}{z_o - z_i}\right]\Delta z - \left[\frac{\left(-k_t A_t \frac{\partial T_t}{\partial z}\right)_i}{z_o - z_i}\right]\Delta z \\
&= \left[\frac{-(0.02799422)(\pi(80)^2)(-0.00975)}{101-100}\right](1) \\
&\quad - \left[\frac{-(0.027995)(\pi(80)^2)(-0.00975)}{101-100}\right](1) \\
&= -0.000144912 \text{ W}
\end{aligned}
\tag{B.44}
$$

The fifth (friction energy) term is evaluated as follows

$$
\begin{aligned}
-F_{drag}\Delta z\, v_t &= -\left(F_{bw} + \tau_t \pi d_t\right)\Delta z\, v_t \\
&= -\left[(1462.94) + (0.227856677)(\pi)(160)\right](1)(15.000566) \\
&= -23662.9917 \text{ W}
\end{aligned}
\tag{B.45}
$$

where the negative sign indicates a loss of energy over the tower control volume.

When dealing with the transient terms of equation (B.40), the same as-

sumptions and properties apply as those used for the evaluation of the transient term of the tower momentum equation.

The magnitude of the first part of the sixth (transient enthalpy) term of equation (B.40) can now be evaluated as follows

$$\begin{aligned}
&\left[\frac{(\rho_{cr} A_t \Delta z\, c_{pcr} T_{cr})_{new} - (\rho_{cr} A_t \Delta z\, c_{pcr} T_{cr})_{old}}{\Delta t}\right] \\
&= \left[\frac{(\rho_{cr} A_t \Delta z c_{pcr} T_{cr})_{new}}{\Delta t}\right] - \left[\frac{(\rho_{cr} A_t \Delta z c_{pcr} T_{cr})_{old}}{\Delta t}\right] \\
&= \left[\frac{(0.9700663)(\pi(80)^2)(1)(1008.02804)(323.15823)}{60}\right] \\
&\quad - \left[\frac{(0.9701056)(\pi(80)^2)(1)(1008.027294)(323.145125)}{60}\right] \\
&= 78.566 \text{ W}
\end{aligned} \tag{B.46}$$

Regard the second part of the sixth (transient kinetic energy) term of equation (B.40) and find

$$\begin{aligned}
&\left[\frac{(\frac{1}{2}\rho_{cr} A_t \Delta z\, {v_{cr}}^2)_{new} - (\frac{1}{2}\rho_{cr} A_t \Delta z\, {v_{cr}}^2)_{old}}{\Delta t}\right] \\
&= \left[\frac{\left(\frac{1}{2}\rho_{cr} A_t \Delta z\, {v_{cr}}^2\right)_{new}}{\Delta t}\right] - \left[\frac{\left(\frac{1}{2}\rho_{cr} A_t \Delta z\, {v_{cr}}^2\right)_{old}}{\Delta t}\right] \\
&= \left[\frac{\frac{1}{2}(0.9700663)(\pi(80)^2)(1)(15.003644)^2}{60}\right] \\
&\quad - \left[\frac{\frac{1}{2}(0.9701056)(\pi(80)^2)(1)(15.000566)^2}{60}\right] \\
&= 13.53 \text{ W}
\end{aligned} \tag{B.47}$$

Comparing the various terms of the tower energy equation, it is clear (from equation (B.41)) that the absolute value of the enthalpy term is the greatest in magnitude. In order to determine which terms of the energy equation can be considered negligible, compare the absolute values of the other terms with the enthalpy term, as shown in table B.6.

When considering table B.6, we find that the enthalpy and potential energy terms are of the same order. The right-hand column gives an indication of the

Table B.6: Comparison between the magnitude of the various energy terms in the tower energy equation

Term	*Absolute Magnitude* [W]	*Percentage of Enthalpy term* [%]
Enthalpy	2928082.23	100
Potential Energy	2867362.45	97.926
Kinetic Energy	4966.138	0.17
Axial Conduction	0.000144912	0.00000
Friction Energy	23662.9917	0.80814
Transient Enthalpy	78.566	0.00268
Transient Kinetic Energy	13.53	0.000462

extremely small contributions made by the axial conduction, transient enthalpy and transient kinetic energy terms to the total energy flux. All three of these terms have magnitudes smaller than 0.003 % of the magnitude of the enthalpy term. The kinetic energy and friction loss terms are larger in scale, but both are still less than 1 % of the size of the enthalpy term.

Therefore, it is assumed that the kinetic energy, axial conduction, friction energy, transient enthalpy and transient kinetic energy terms may be neglected when evaluating the tower air stream energy equation.

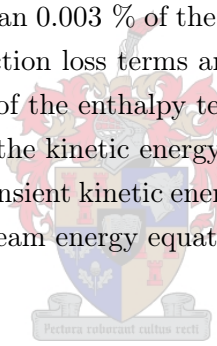

B.1 Controlled flow

We now consider the magnitude of the terms of the tower momentum and energy equation when assuming a controlled flow through the solar tower power plant.

The main aim of this section is to evaluate the magnitude of the various terms that significantly change the conditions inside the solar tower over a relatively short period of time. This simulates controlling the output of the solar tower power plant to cope with electricity demand fluctuations.

Once again certain conditions have to be assumed at the inlet and outlet of the tower control volume. Different inlet conditions to those used previously are assumed, to allow for condition changes when evaluating the magnitude of the transient terms.

The tower dimensions, control volume dimensions, DALR assumption inside the tower and inlet pressure of the control volume remain the same as

before.

Table B.7 exhibits the dimensions and inlet conditions chosen, where the temperature and mass flow values are obtained from the results of a numerical model developed by Hedderwick (2001). The data extracted from Hedderwick (2001) is taken on a summer's day at the nearest collector node to the tower as before, and at a time when the modelled solar tower plant produces a low energy output.

Table B.7: Dimensions and chosen inlet conditions for a controlled flow assumption

z_i	100 m
z_o	101 m
T_{ti}	300.95 K
$\dot{m}_{ti}$	154710.3 kg/s
p_{ti}	90000 N/m^2
d_t	160 m

By employing the DALR assumption and using the relations for thermophysical properties in Kröger (2004), the temperature and pressure at the outlet of the control volume is calculated in exactly the same way as shown in equations (B.1) and (B.2).

The air density at the inlet and outlet of the tower control volume is determined using the perfect gas law, analogous to equations (B.3) and (B.4).

Utilizing equations (B.5) to (B.10), as given in Kröger (2004), the inlet and outlet specific heat capacity, dynamic viscosity and thermal conductivity values are found.

Approximating the mass flow through the control volume as constant, the inlet and outlet air stream velocity may be determined in likewise fashion to equation (B.12).

The average density, velocity, dynamic viscosity and tower Reynolds number are determined analogously to equations (B.13) to (B.16), while the friction factor (with $\varepsilon_t = 0.002$ m), wall shear stress and total bracing wheel force per unit height (with $K_{bw} = 0.1$) are calculated likewise to equations (B.17) to (B.19).

Table B.8 summarizes the calculated properties of the tower control volume, as described above.

Table B.8: Summary of calculated tower control volume properties for a controlled flow assumption

T_{to}	300.94025 K
p_{to}	89989.79523 N/m^2
ρ_{ti}	1.041706 kg/m^3
ρ_{to}	1.041622 kg/m^3
c_{pti}	1006.98721 J/kg·K
c_{pto}	1006.986853 J/kg·K
μ_{ti}	1.85123367×10^{-5} kg/m·s
μ_{to}	1.85118886×10^{-5} kg/m·s
k_{ti}	0.026294866 W/m·K
k_{to}	0.026294112 W/m·K
v_{ti}	7.38659 m/s
v_{to}	7.38719 m/s
ρ_t	1.04166396 kg/m^3
v_t	7.3868919 m/s
μ_t	1.85121126×10^{-5} kg/m·s
Re_t	66504859.66
f_t	0.008351478
τ_t	0.05933685 N/m^2
F_{bw}	380.927 N/m

Again, when dealing with the transient terms of the tower momentum and energy equation, certain additional assumptions have to be made.

The initial inlet conditions are assumed to be as specified above, while the tower and control volume dimensions also remain the same. The transient terms are once again evaluated at the center of the tower control volume (at a height of 100.5 m), although now they are evaluated over a period of 15 minutes.

Thus, inlet conditions must once again be assumed for the next time step. From the results of the numerical model by Hedderwick (2001), temperature and mass flow values are taken at the nearest collector node to the tower. The values are extracted from the model's results at a time when the modelled solar tower plant produces a peak energy output.

Table B.9 displays the initial and new conditions assumed at the tower control volume inlet.

Table B.9: Initial and new inlet conditions for evaluating transient terms for a controlled flow assumption

$T_{ti,\,old}$	300.95 K
$\dot{m}_{ti,\,old}$	154710.3 kg/s
$T_{ti,\,new}$	317.25 K
$\dot{m}_{ti,\,new}$	250889.4 kg/s
p_{ti}	90000 N/m^2

By utilizing equations (B.22) to (B.31), we find the initial and new values for temperature, pressure, density, specific heat capacity and air stream velocity at the center of the control volume. These calculated properties are presented in table B.10.

Table B.10: Summary of calculated initial and new properties at the center of the tower control volume for a controlled flow assumption

$T_{cr,\,old}$	300.945 K
$T_{cr,\,new}$	317.245 K
$p_{cr,\,old}$	89994.89751 N/m^2
$p_{cr,\,new}$	89995.15967 N/m^2
$\rho_{cr,\,old}$	1.041664 kg/m^3
$\rho_{cr,\,new}$	0.988146 kg/m^3
$c_{pcr,\,old}$	1006.987032 J/kg·K
$c_{pcr,\,new}$	1007.707193 J/kg·K
$v_{cr,\,old}$	7.38689 m/s
$v_{cr,\,new}$	12.6279 m/s

Tower momentum equation

The scale of the first five terms of equation (B.32) are determined analogously to equations (B.33) to (B.37) and are summarized later in table B.11.

The transient momentum term of equation (B.32) is determined by employing the transient term assumptions as before and utilizing equation (B.38). The magnitude of this transient term is compared with the other terms of equation (B.32) in table B.11.

Table B.11: Comparison between the magnitude of the various terms in the tower momentum equation for a controlled flow assumption

Term	*Absolute Magnitude* [N/m^3]	*Percentage of Gravity Force term* [%]
Gravity Force	10.20830677	100
Axial Pressure Difference	10.20477032	99.965
Wall Friction	0.001483421	0.01453
Bracing Wheel Force	0.01894577	0.18559
Axial Momentum	0.0046037	0.0451
Transient Momentum	0.0059101	0.0579

When regarding table B.11, we find that the gravity force and axial pressure difference terms are once again of the same order. The wall friction, bracing wheel force and axial momentum terms are smaller when employing a controlled flow assumption, and all three have magnitudes of less than 0.2 % of the gravity force term. The transient momentum term is much larger for a controlled flow assumption, but is still smaller than 0.06 % of the magnitude of the gravity force term.

Once again, when comparing these terms as terms in the tower draught equation, the wall friction, bracing wheel force, axial momentum and transient momentum terms will be an order larger than shown in table B.11. The result is a bracing wheel force term with a magnitude close to 2 % of the gravity force term. The bracing wheel force term will accordingly not be assumed to be negligible. Due to some uncertainty concerning an assumed roughness value for the inside surface of the tower, the wall friction term will not be considered negligible.

It is therefore assumed that for a controlled flow situation, the axial momentum and transient momentum terms may be considered negligible when evaluating the tower momentum equation.

Tower energy equation

When considering the magnitude of the first five terms of equation (B.40), the same assumptions, inlet and outlet conditions apply as those enforced for the evaluation of the non-transient terms of the tower momentum equation when

for a controlled flow assumption.

The magnitude of the these terms are calculated using once again equations (B.41) to (B.45) and are summarized in table B.12.

When dealing with the transient terms of equation (B.40), the same assumptions and properties apply as those used for the evaluation of the transient terms of the tower momentum equation for a controlled flow assumption.

The transient enthalpy and transient kinetic energy terms of equation (B.40) may now be determined in likewise fashion to the natural flow situation by employing equations (B.46) and (B.47). The size of the transient terms are compared with the other energy terms of equation (B.40) in table B.12.

It is important to note that the size of the (change in axial) enthalpy term increases significantly during the time step of 15 minutes. However, the initial and smaller enthalpy value (during time of low plant output) is selected as reference value for comparing the scale of the various energy terms.

Table B.12: Comparison between the magnitude of the various energy terms in the tower energy equation for a controlled flow assumption

Term	*Absolute Magnitude* [W]	*Percentage of Enthalpy term* [%]
Enthalpy	1535619.467	100
Potential Energy	1516160.94	98.733
Kinetic Energy	683.754	0.04453
Axial Conduction	0.00014785	0.00000
Friction Energy	220.461	0.014357
Transient Enthalpy	5064.058	0.3298
Transient Kinetic Energy	1125.213	0.07327

When regarding table B.12, we find that the enthalpy and potential energy terms are once again of the same order. It is clear that the contribution made by the axial conduction term to the total energy flux can be considered to be negligible. The kinetic energy and friction energy terms are smaller in scale when employing the controlled flow assumption, both being less than 0.05 % of the enthalpy term.

The transient enthalpy and transient kinetic energy terms are greater for a controlled flow environment, but with the larger term still only having a magnitude smaller than 0.4 % of the magnitude of the specified enthalpy term.

Therefore, it is assumed that, when employing a controlled flow assumption in the solar tower power plant, the kinetic energy, axial conduction, friction energy, transient enthalpy and transient kinetic energy terms may be neglected when evaluating the tower air stream energy equation.

Pectora roborant cultus recti

Appendix C

Meteorological Data of Reference Location

When modelling the solar tower power plant, environmental conditions must be specified over a period of one year. Due to the fact that the plant generates electricity by harnessing the sun's energy, solar radiation will obviously be a crucial input. Another important influence on the power plant's performance will be the ambient temperature. Other influencing factors include the wind conditions and humidity.

The reference location selected is near Sishen, South Africa. This particular location is dry and hot and experiences predominantly clear sky days and nights. The specific location co-ordinates are:

Table C.1: Reference Location co-ordinates and Standard Time Zone

Latitude	27.67° South
Longitude	23.00° East
Standard Time Zone	30° East

C.1 Solar radiation input data

Solar radiation consists of two components, namely beam and diffuse radiation. The sum of these two gives the total solar radiation. The solar radiation input data used is given in table C.2 in the format of total and diffuse solar radiation (in W/m^2) on a horizontal surface for a specific solar time (sunshine) hour.

These are average hourly values for an average day in that specific month. Negligible solar radiation is assumed for the hours not shown in the table.

C.2 Ambient temperature

The ambient air temperatures shown in table C.3 are those air temperatures which occur at approximately 1.5 m above ground level at the specific location. The table displays ambient air temperatures (in ℃) for a specific solar time hour. These temperatures are average hourly values for an average day in that specific month.

C.3 Ambient wind speed

The ambient wind speeds are shown in table C.4 and are those wind speeds measured at 10 m above ground level at the specific location. The table displays ambient wind speeds (in m/s) for a specific solar time hour. These speeds are average hourly values for an average day in that specific month.

C.4 Interpretation of input data

In order to find a smoother representation of the input data for its use in the numerical model, the input solar radiation, ambient air temperature and ambient wind speed data is interpreted in the following way.

It is assumed that the values given in table C.2, C.3 and C.4 are the specific values which occur on the stroke of the given solar time hour on the 15th of that particular month. The data is then interpolated between months to find values for specific days and then interpolated between hours to give specific minutely input values. Thus the input data to the numerical model are approximated values which occur at a specific minute of a particular day of the year.

Table C.2: Total (I_h) and diffuse (I_{hd}) solar radiation on a horizontal surface, W/m^2

Solar Time	**6**		**7**		**8**		**9**		**10**		**11**		**12**	
	I_h	I_{hd}	I_h	I_{hd}	I_h	I_{hd}	I_h	I_{hd}	I_h	I_{hd}	I_h	I_{hd}	I_h	I_{hd}
Jan	138	52	357	89	572	108	762	126	909	136	1003	140	1035	135
Feb	68	46	279	86	496	109	691	124	845	144	942	151	976	156
Mar	0	0	190	72	406	102	604	121	763	130	865	138	900	144
Apr	0	0	100	50	299	84	489	112	644	129	745	134	780	148
May	0	0	35	18	220	66	407	85	562	101	664	106	700	105
Jun	0	0	19	10	190	63	368	88	517	109	616	117	650	111
Jul	0	0	35	17	220	66	407	90	562	107	664	113	700	112
Aug	0	0	99	50	295	91	483	106	636	127	735	125	770	123
Sep	0	0	182	78	388	109	578	127	730	139	827	149	861	155
Oct	66	45	272	95	483	121	673	141	822	156	917	165	950	181
Nov	135	62	348	90	558	112	743	126	887	133	979	137	1010	131
Dec	157	58	375	83	587	103	773	108	917	119	1009	121	1040	114

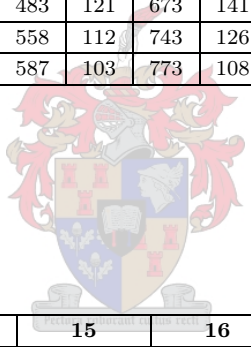

Solar Time	**13**		**14**		**15**		**16**		**17**		**18**	
	I_h	I_{hd}	I_h	I_{hd}	I_h	I_{hd}	I_h	I_{hd}	I_h	I_{hd}	I_h	I_{hd}
Jan	1003	140	909	136	762	130	572	114	357	82	138	40
Feb	942	160	845	161	691	145	496	114	279	75	68	24
Mar	865	138	763	145	604	133	406	102	180	54	0	0
Apr	745	142	644	129	489	108	299	78	110	31	0	0
May	664	100	562	96	407	77	220	48	35	11	0	0
Jun	616	105	517	93	368	70	190	44	19	6	0	0
Jul	664	106	562	96	407	77	220	48	35	12	0	0
Aug	735	125	636	114	483	101	295	71	99	32	0	0
Sep	827	149	730	146	578	121	388	97	182	58	0	0
Oct	917	183	822	173	673	155	483	135	272	90	66	28
Nov	979	137	887	142	743	134	558	117	348	87	135	45
Dec	1009	131	917	128	773	124	587	116	375	86	157	49

Table C.3: Ambient air temperature, ℃

Solar Time	1	2	3	4	5	6	7	8	9	10	11	12
Jan	25.52	25.09	24.66	24.33	23.8	23.37	22.94	22.51	24.1	25.9	27.6	29
Feb	24.89	24.46	24.03	23.6	23.17	22.72	22.31	21.88	22.7	24.5	26.2	27.6
Mar	22.59	22.16	21.73	21.3	20.87	20.44	20.01	19.58	20.7	22.8	24.5	25.9
Apr	18.19	17.76	17.33	16.9	16.47	16.04	15.61	15.18	16.5	18.8	20.6	22
May	15.96	15.53	15.1	14.67	14.24	13.81	13.38	12.95	12.52	14.8	16.9	18.4
Jun	13.16	12.73	12.3	11.87	11.44	11.01	10.58	10.15	9.72	11.3	13.6	15.4
Jul	14.06	13.63	13.2	12.77	12.34	11.91	11.48	11.05	10.62	11.4	13.8	15.7
Aug	14.79	14.36	13.93	13.5	13.07	12.64	12.21	11.78	11.35	13.7	15.9	17.7
Sep	19.59	19.16	18.73	18.3	17.87	17.44	17.01	16.58	16.15	18.5	20.6	22.2
Oct	22.09	21.66	21.23	20.8	20.37	19.94	19.51	19.08	19.4	21.5	23.3	24.8
Nov	22.52	22.09	21.66	21.23	20.8	20.37	19.94	20	22.2	24.1	25.7	27
Dec	24.92	24.49	24.06	23.63	23.2	22.77	22.34	21.91	24	25.8	27.4	28.6

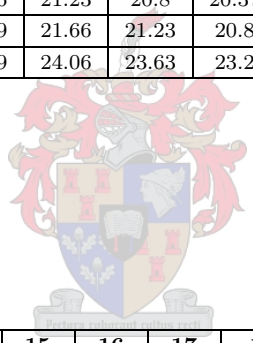

Solar Time	13	14	15	16	17	18	19	20	21	22	23	24
Jan	30	30.5	30.7	30.5	30.1	29.3	28.1	27.67	27.24	26.81	26.38	25.95
Feb	28.7	29.4	29.5	29.3	28.7	27.9	27.47	27.04	26.61	26.18	25.75	25.32
Mar	26.8	27.4	27.5	27.3	26.5	25.6	25.17	24.74	24.31	23.88	23.45	23.02
Apr	23	23.6	23.9	23.6	23	21.2	20.77	20.34	19.91	19.48	19.05	18.62
May	19.5	20.2	20.4	20.3	19.4	18.97	18.54	18.11	17.68	17.25	16.82	16.39
Jun	16.5	17.3	17.7	17.5	16.6	16.17	15.74	15.31	14.88	14.45	14.02	13.59
Jul	17	17.9	18.3	18.2	17.5	17.07	16.64	16.21	15.78	15.35	14.92	14.49
Aug	19.1	20	20.5	20.5	19.9	17.8	17.37	16.94	16.51	16.08	15.65	15.22
Sep	23.5	24.3	24.7	24.7	24.1	22.6	22.17	21.74	21.31	20.88	20.45	20.02
Oct	25.9	26.6	26.9	26.9	26.3	25.1	24.67	24.24	23.81	23.38	22.95	22.52
Nov	27.9	28.5	28.6	28.4	27.9	27	25.1	24.67	24.24	23.81	23.38	22.95
Dec	29.7	30.1	30.4	30.3	29.7	28.9	27.5	27.07	26.64	26.21	25.78	25.35

Table C.4: Ambient wind speed, in m/s, at 10 m above ground level

Solar Time	1	2	3	4	5	6	7	8	9	10	11	12
Jan	2.68	2.70	2.66	2.68	2.70	2.61	2.71	3.03	3.64	3.44	3.00	2.97
Feb	2.56	2.46	2.25	2.17	2.09	2.11	2.46	2.77	3.13	3.28	3.35	3.28
Mar	2.26	2.31	2.34	2.40	2.40	2.42	2.38	2.64	3.00	3.20	3.31	3.34
Apr	3.04	2.93	2.84	2.75	2.71	2.65	2.67	2.82	3.22	3.63	3.82	3.89
May	2.93	2.93	2.94	2.99	3.02	2.99	2.89	2.76	2.83	3.16	3.32	3.42
Jun	3.40	3.29	3.24	3.19	3.05	2.91	2.79	2.75	3.00	3.37	3.63	3.81
Jul	3.54	3.62	3.50	3.28	3.12	3.05	3.06	3.01	3.31	3.80	4.01	4.02
Aug	3.47	3.60	3.71	3.75	3.82	3.79	3.48	3.33	3.52	3.72	3.90	4.03
Sep	3.65	3.66	3.62	3.47	3.41	3.38	3.50	3.87	4.38	4.58	4.72	4.79
Oct	3.43	3.52	3.35	3.14	3.15	3.16	3.29	3.70	3.96	4.04	4.19	4.21
Nov	3.45	3.47	3.51	3.31	3.22	3.24	3.54	4.18	4.21	4.30	4.33	4.47
Dec	2.69	2.67	2.59	2.72	2.83	2.82	3.04	3.53	4.01	4.27	4.33	4.39

Solar Time	13	14	15	16	17	18	19	20	21	22	23	24
Jan	3.15	3.23	3.15	3.24	3.40	3.26	2.71	2.60	2.63	2.75	2.93	2.69
Feb	3.21	3.33	3.59	3.69	3.54	3.29	2.94	2.68	2.61	2.53	2.57	2.38
Mar	3.42	3.54	3.61	3.56	3.30	2.88	2.54	2.58	2.67	2.52	2.50	2.36
Apr	3.87	3.85	3.69	3.56	3.33	2.94	2.79	2.90	3.03	3.05	3.03	3.11
May	3.46	3.45	3.46	3.41	2.99	2.49	2.54	2.73	2.73	2.88	3.02	2.99
Jun	3.86	3.84	3.77	3.62	3.12	2.69	2.82	3.00	3.14	3.29	3.44	3.44
Jul	4.01	3.95	3.89	3.75	3.32	2.95	2.93	3.05	3.19	3.33	3.46	3.46
Aug	3.99	3.98	4.01	3.88	3.50	2.96	2.75	2.98	3.11	3.23	3.41	3.45
Sep	4.81	4.77	4.78	4.64	4.38	3.84	3.44	3.43	3.42	3.47	3.71	3.68
Oct	4.41	4.51	4.64	4.50	4.38	4.11	3.36	2.95	3.11	3.18	3.23	3.27
Nov	4.53	4.58	4.53	4.51	4.50	4.38	3.88	3.38	3.26	3.18	3.32	3.30
Dec	4.44	4.38	4.22	4.11	4.06	4.01	3.63	3.19	3.27	3.13	2.92	2.78

Pectora roborant cultus recti

Appendix D

Derivation of the Discretization Schemes

D.1 Collector air discretization scheme

Through personal communication, Buys (2003-2004) suggested employing a more accurate discretization scheme for the air control volumes in the collector than the general backward difference scheme, as was done initially. This scheme approximates the gradient at a node by taking the finite difference between the specific node and the two previous upwind nodes. The scheme, given in chapter 2 by equation (2.12), is derived for the collector as follows:

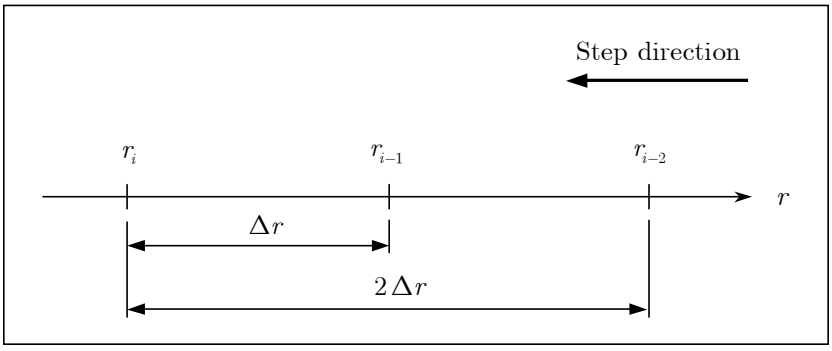

Figure D.1: Collector finite difference grid for the air control volumes

Let

$$\frac{\partial \phi}{\partial r} \approx a\phi_i + b\phi_{i-1} + c\phi_{i-2} \tag{D.1}$$

Then, from figure D.1, the local truncation error is found from

$$\begin{aligned} T_i &= \frac{\partial \phi}{\partial r}(r_i) - a\phi(r_i) - b\phi(r_i + \Delta r) - c\phi(r_i + 2\Delta r) \\ &= \phi' - a\phi - b\left[\phi + \Delta r\phi' + \frac{(\Delta r)^2}{2}\phi'' + O(\Delta r^3)\right] \\ &\quad - c\left[\phi + 2\Delta r\phi' + \frac{(2\Delta r)^2}{2}\phi'' + O(\Delta r^3)\right] \\ &= -\phi_i(a+b+c) + \phi_i'(1 - b\Delta r - 2c\Delta r) - \phi_i''\left(\frac{1}{2}b(\Delta r)^2 + 2c(\Delta r)^2\right) \\ &\quad + b\,O(\Delta r^3) + c\,O(\Delta r^3) \end{aligned} \tag{D.2}$$

Now, we choose

$$a + b + c = 0 \tag{D.3}$$

$$1 - b\Delta r - 2c\Delta r = 0 \tag{D.4}$$

$$\frac{1}{2}b\,(\Delta r)^2 + 2c\,(\Delta r)^2 = 0 \tag{D.5}$$

and find for the constants a, b and c

$$a = -\frac{3}{2\Delta r} \qquad b = \frac{2}{\Delta r} \qquad c = -\frac{1}{2\Delta r}$$

When substituting the constants into equation (D.1), we find

$$\left(\frac{\partial \phi}{\partial r}\right)\Big|_i = \frac{-3\phi_i + 4\phi_{i-1} - \phi_{i-2}}{2\Delta r} + O(\Delta r^2) \tag{D.6}$$

D.2 Collector ground discretization scheme

This section derives an accurate implicit difference method for the ground control volumes in the collector of the solar tower power plant, as derived by Buys (2003-2004) and discussed in chapter 2 of this document.

The finite difference grid for the ground control volumes is constructed as in figure D.2, with two "fictitious" nodes above the ground surface and below

the deepest node in the ground. These "fictitious" nodes have no real value in the sense of evaluating the ground temperatures in the ground, but are used in conjunction with the nodes from $z_{g,1}$ to $z_{g,N}$ to determine the actual ground temperature values.

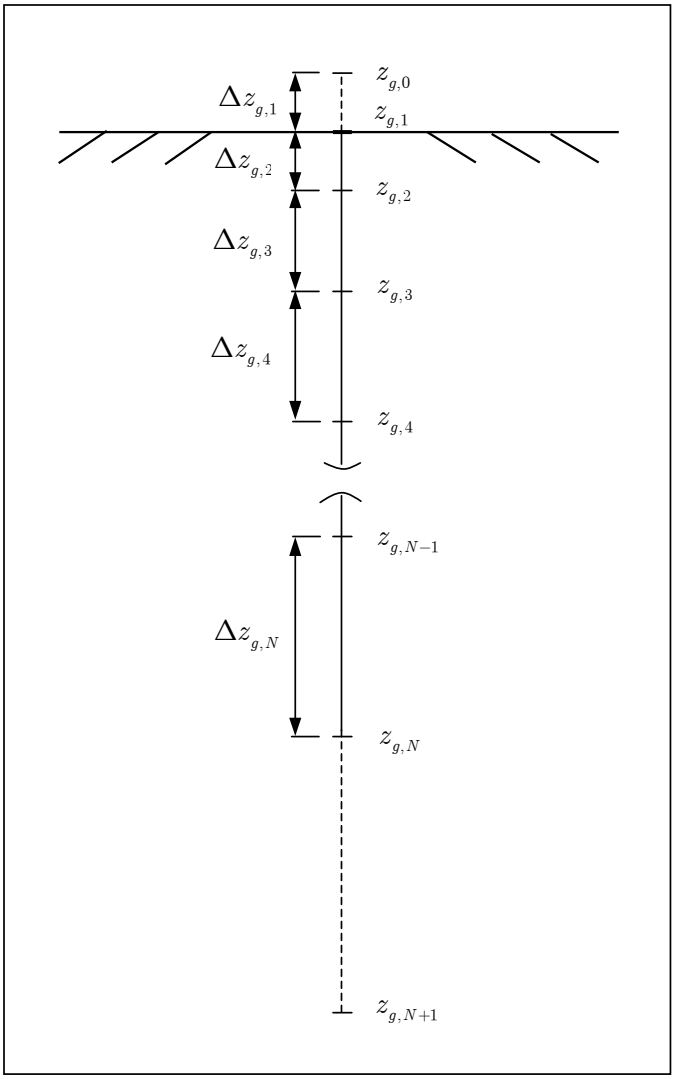

Figure D.2: Collector finite difference grid for the ground control volumes

The thickness (depth) of each control volume below the ground is calculated by multiplying a factor (which must be chosen) with the previous control volume thickness, i.e.

$$\Delta z_{g,\,k+1} = \theta\, \Delta z_{g,\,k} \qquad \textit{for } k = 1, 2, ...N \tag{D.7}$$

where θ is the chosen multiplying factor. The value for $\Delta z_{g,\,1}$ must also be chosen. The position of each node below the ground surface is then obtained using

$$z_{g,\,k+1} = z_{g,\,k} + \Delta z_{g,\,k+1} \qquad \textit{for } k = 1, 2, ...N \tag{D.8}$$

where $z_{g,\,1}$ is the ground surface node and is thus located at a depth of 0 m.

D.2.1 Derivation

Figure D.3 shows the spacing convention employed between the nodes of the ground control volumes for varying control volume thicknesses.

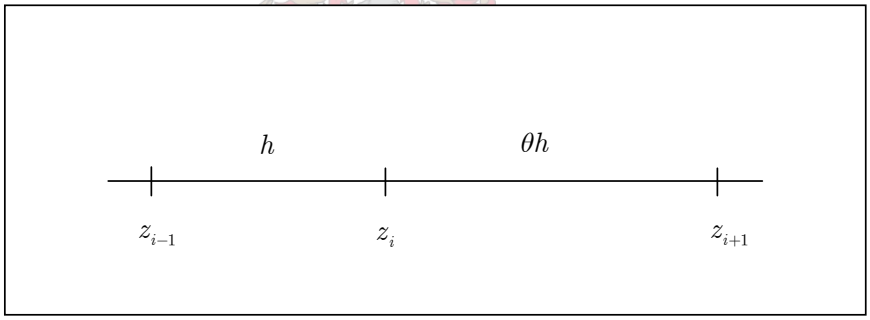

Figure D.3: Spacing convention between the ground control volumes

Let us approximate the equation

$$\frac{\partial \phi}{\partial t} = a_g \frac{\partial^2 \phi}{\partial z^2} \tag{D.9}$$

by

$$\begin{aligned}
&\beta_{-1}\left.\frac{\partial\phi}{\partial t}\right|_{i-1}^{m+\frac{1}{2}} + \beta_0\left.\frac{\partial\phi}{\partial t}\right|_{i}^{m+\frac{1}{2}} + \beta_1\left.\frac{\partial\phi}{\partial t}\right|_{i+1}^{m+\frac{1}{2}} \\
&= a_g\left[\beta_{-1}\left.\frac{\partial^2\phi}{\partial z^2}\right|_{i-1}^{m+\frac{1}{2}} + \beta_0\left.\frac{\partial^2\phi}{\partial z^2}\right|_{i}^{m+\frac{1}{2}} + \beta_1\left.\frac{\partial^2\phi}{\partial z^2}\right|_{i+1}^{m+\frac{1}{2}}\right] \\
&= a_g\left[\alpha_{-1}{\phi_{i-1}}^{m+\frac{1}{2}} + \alpha_0{\phi_i}^{m+\frac{1}{2}} + \alpha_1{\phi_{i+1}}^{m+\frac{1}{2}}\right]
\end{aligned} \tag{D.10}$$

where the superscript m indicates the time step. Therefore, $m+\frac{1}{2}$ represents the average value between the value at the current and old time step. The zero subscript of the α and β coefficients indicate that it is the coefficient at the specific node i, while the subscripts -1 and 1 represent the coefficients at the previous $(i-1)$ and following $(i+1)$ nodes respectively.

If we now discretize equation (D.10), we find

$$\begin{aligned}
&\beta_{-1}\left(\frac{\phi_{i-1}-{\phi_{i-1}}^{old}}{\Delta t}\right) + \beta_0\left(\frac{\phi_i-{\phi_i}^{old}}{\Delta t}\right) + \beta_1\left(\frac{\phi_{i+1}-{\phi_{i+1}}^{old}}{\Delta t}\right) \\
&= \frac{a_g}{2}\left[\alpha_{-1}\phi_{i-1}+\alpha_0\phi_i+\alpha_1\phi_{i+1}+\alpha_{-1}{\phi_{i-1}}^{old}+\alpha_0{\phi_i}^{old}+\alpha_1{\phi_{i+1}}^{old}\right]
\end{aligned} \tag{D.11}$$

Rearrange equation (D.11) and find

$$\begin{aligned}
&\left(\beta_{-1}-\frac{a_g\Delta t}{2}\alpha_{-1}\right)\phi_{i-1} + \left(\beta_0-\frac{a_g\Delta t}{2}\alpha_0\right)\phi_i + \left(\beta_1-\frac{a_g\Delta t}{2}\alpha_1\right)\phi_{i+1} \\
&= \left(\beta_{-1}+\frac{a_g\Delta t}{2}\alpha_{-1}\right){\phi_{i-1}}^{old} + \left(\beta_0+\frac{a_g\Delta t}{2}\alpha_0\right){\phi_i}^{old} + \left(\beta_1+\frac{a_g\Delta t}{2}\alpha_1\right){\phi_{i+1}}^{old}
\end{aligned} \tag{D.12}$$

Equation (D.12) can be further simplified by defining the following constants for $k = 1, 2, ...N$

$$\begin{aligned}
a_k &= \beta_{-1}-\frac{a_g\Delta t}{2}{\alpha_{-1}}^k & b_k &= \beta_0-\frac{a_g\Delta t}{2}{\alpha_0}^k & c_k &= \beta_1-\frac{a_g\Delta t}{2}{\alpha_1}^k \\
{a_k}^* &= \beta_{-1}+\frac{a_g\Delta t}{2}{\alpha_{-1}}^k & {b_k}^* &= \beta_0+\frac{a_g\Delta t}{2}{\alpha_0}^k & {c_k}^* &= \beta_1+\frac{a_g\Delta t}{2}{\alpha_1}^k
\end{aligned}$$

When substituting these constants into equation (D.12), we find

$$a_k\,\phi_{k-1} + b_k\,\phi_k + c_k\,\phi_{k+1} = {a_k}^*{\phi_{k-1}}^{old} + {b_k}^*{\phi_k}^{old} + {c_k}^*{\phi_{k+1}}^{old} \qquad \text{(D.13)}$$

which is the same as equation (2.15) in chapter 2 of this document.

However, the various α and β constants have yet to be defined. Therefore, suppose the right-hand-side of equation (D.9) may be approximated (for the case where i = 0 in figure D.3) by

$$\begin{aligned}\alpha_{-1}\,\phi(z_0 - h) + \alpha_0\,\phi(z_0) + \alpha_1\,\phi(z_0 + \theta h)& \\ \approx \beta_{-1}\,\frac{\partial^2\phi}{\partial z^2}\bigg|_{z_{-1}} + \beta_0\,\frac{\partial^2\phi}{\partial z^2}\bigg|_{z_0} + \beta_1\,\frac{\partial^2\phi}{\partial z^2}\bigg|_{z_1}& \qquad \text{(D.14)}\end{aligned}$$

The local truncation error is now found from

$$\begin{aligned}T = {}& \alpha_{-1}\left[\phi - h\phi' + \frac{h^2}{2}\phi'' - \frac{h^3}{6}\phi''' + \frac{h^4}{24}\phi^{(4)} - \frac{h^5}{120}\phi^{(5)} + \frac{h^6}{720}\phi^{(6)}\right] \\ & + \alpha_0\,\phi \\ & + \alpha_1\left[\phi + \theta h\phi' + \frac{(\theta h)^2}{2}\phi'' + \frac{(\theta h)^3}{6}\phi''' + \frac{(\theta h)^4}{24}\phi^{(4)} + \frac{(\theta h)^5}{120}\phi^{(5)} + \frac{(\theta h)^6}{720}\phi^{(6)}\right] \\ & - \beta_{-1}\left[\phi'' - h\phi''' + \frac{h^2}{2}\phi^{(4)} - \frac{h^3}{6}\phi^{(5)} + \frac{h^4}{24}\phi^{(6)}\right] \\ & - \beta_0\,\phi'' \\ & - \beta_1\left[\phi'' + \theta h\phi''' + \frac{(\theta h)^2}{2}\phi^{(4)} + \frac{(\theta h)^3}{6}\phi^{(5)} + \frac{(\theta h)^4}{24}\phi^{(6)}\right]\end{aligned}$$

$$
\begin{aligned}
&= \phi\left(\alpha_{-1}+\alpha_0+\alpha_1\right)+\phi'\left(-h\alpha_{-1}+\theta h\alpha_1\right)\\
&\quad+\phi''\left(\frac{1}{2}h^2\alpha_{-1}+\frac{1}{2}\theta^2h^2\alpha_1-\beta_{-1}-\beta_0-\beta_1\right)\\
&\quad+\phi'''\left(-\frac{1}{6}h^3\alpha_{-1}+\frac{1}{6}\theta^3h^3\alpha_1+h\beta_{-1}-\theta h\beta_1\right)\\
&\quad+\phi^{(4)}\left(\frac{1}{24}h^4\alpha_{-1}+\frac{1}{24}\theta^4h^4\alpha_1-\frac{1}{2}h^2\beta_{-1}-\frac{1}{2}\theta^2h^2\beta_1\right)\\
&\quad+\phi^{(5)}\left(-\frac{1}{120}h^5\alpha_{-1}+\frac{1}{120}\theta^5h^5\alpha_1+\frac{1}{6}h^3\beta_{-1}-\frac{1}{6}\theta^3h^3\beta_1\right)\\
&\quad+\phi^{(6)}\left(\frac{1}{720}h^6\alpha_{-1}+\frac{1}{720}\theta^6h^6\alpha_1-\frac{1}{24}h^4\beta_{-1}-\frac{1}{24}\theta^4h^4\beta_1\right)+O(h^5)
\end{aligned}
\tag{D.15}
$$

Now we choose

$$\alpha_{-1}+\alpha_0+\alpha_1=0 \tag{D.16}$$

$$-h\alpha_{-1}+\theta h\alpha_1=0 \tag{D.17}$$

$$\frac{1}{2}h^2\alpha_{-1}+\frac{1}{2}\theta^2h^2\alpha_1-\beta_{-1}-\beta_0-\beta_1=0 \tag{D.18}$$

$$-\frac{1}{6}h^3\alpha_{-1}+\frac{1}{6}\theta^3h^3\alpha_1+h\beta_{-1}-\theta h\beta_1=0 \tag{D.19}$$

$$\frac{1}{24}h^4\alpha_{-1}+\frac{1}{24}\theta^4h^4\alpha_1-\frac{1}{2}h^2\beta_{-1}-\frac{1}{2}\theta^2h^2\beta_1=0 \tag{D.20}$$

$$-\frac{1}{120}h^5\alpha_{-1}+\frac{1}{120}\theta^5h^5\alpha_1+\frac{1}{6}h^3\beta_{-1}-\frac{1}{6}\theta^3h^3\beta_1=0 \tag{D.21}$$

$$\frac{1}{720}h^6\alpha_{-1}+\frac{1}{720}\theta^6h^6\alpha_1-\frac{1}{24}h^4\beta_{-1}-\frac{1}{24}\theta^4h^4\beta_1=0 \tag{D.22}$$

When solving equations (D.16) to (D.20) simultaneously together with the normalizing condition $\beta_{-1}+\beta_0+\beta_1=1$, we find for the constants α_{-1}, α_0, α_1, β_{-1}, β_0 and β_1

$$\alpha_{-1} = \frac{2}{h^2(1+\theta)} \qquad \alpha_0 = -\frac{2}{h^2\theta} \qquad \alpha_1 = \frac{2}{h^2\theta(1+\theta)}$$

$$\beta_{-1} = \frac{1+\theta-\theta^2}{6(1+\theta)} \qquad \beta_0 = \frac{\theta^2+3\,\theta+1}{6\,\theta} \qquad \beta_1 = \frac{\theta^2+\theta-1}{6\,\theta(1+\theta)}$$

The β coefficients remain constant for all the ground control volumes for a constant θ value. However, the α coefficients will vary as the ground control volume thicknesses vary into the ground. Thus, for a constant θ value, the α coefficients are determined for $k = 1, 2, ...N$ using

$${\alpha_{-1}}^k = \frac{2}{(\Delta z_{g,\,k})^2(1+\theta)} \qquad {\alpha_0}^k = -\frac{2}{(\Delta z_{g,\,k})^2\theta} \qquad {\alpha_1}^k = \frac{2}{(\Delta z_{g,\,k})^2\theta(1+\theta)}$$

D.2.2 Boundary values

Upper boundary

For the ground surface energy equation, the temperature gradient is approximated by the following relation (from figure D.4, where z_0 is the ground surface node)

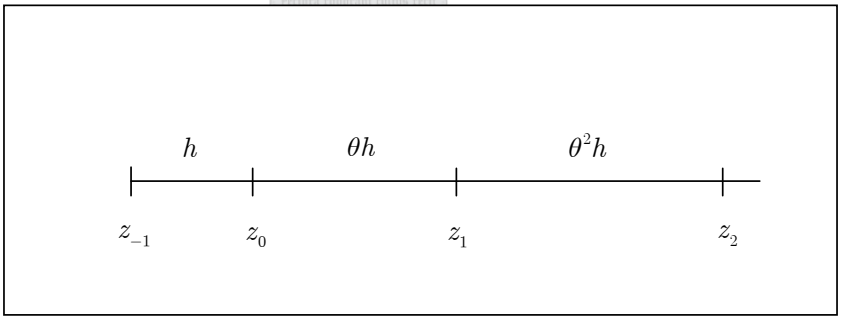

Figure D.4: Upper boundary grid nodes

$$\left.\frac{\partial\phi}{\partial z}\right|_0 \approx \alpha_{-1}\phi_{-1} + \alpha_0\phi_0 + \alpha_1\phi_1 + \alpha_2\phi_2 \tag{D.23}$$

The local truncation error is

$$
\begin{aligned}
T &= \alpha_{-1}\phi_{-1} + \alpha_0\phi_0 + \alpha_1\phi_1 + \alpha_2\phi_2 - \phi_0' \\
&= \alpha_{-1}\left[\phi - h\phi' + \frac{h^2}{2}\phi'' - \frac{h^3}{6}\phi''' + O(h^4)\right] + \alpha_0\phi_0 - \phi_0' \\
&\quad + \alpha_1\left[\phi + \theta h\phi' + \frac{(\theta h)^2}{2}\phi'' + \frac{(\theta h)^3}{6}\phi''' + O(h^4)\right] \\
&\quad + \alpha_2\left[\phi + \theta(1+\theta)h\phi' + \frac{1}{2}(\theta(1+\theta)h)^2\phi'' + \frac{1}{6}(\theta(1+\theta)h)^3\phi''' + O(h^4)\right] \\
&= \phi_0(\alpha_{-1} + \alpha_0 + \alpha_1 + \alpha_2) \\
&\quad + \phi_0'(-h\alpha_{-1} - 1 + \theta h\alpha_1 + \theta(1+\theta)h\alpha_2) \\
&\quad + \phi_0''\left(\frac{1}{2}h^2\alpha_{-1} + \frac{1}{2}\theta^2h^2\alpha_1 + \frac{1}{2}\theta^2(1+\theta)^2h^2\alpha_2\right) \\
&\quad + \phi_0'''\left(-\frac{1}{6}h^3\alpha_{-1} + \frac{1}{6}\theta^3h^3\alpha_1 + \frac{1}{6}\theta^3(1+\theta)^3h^3\alpha_2\right) + O(h^4)
\end{aligned}
\tag{D.24}
$$

Now we choose

$$\alpha_{-1} + \alpha_0 + \alpha_1 + \alpha_2 = 0 \tag{D.25}$$

$$-h\alpha_{-1} - 1 + \theta h\alpha_1 + \theta(1+\theta)h\alpha_2 = 0 \tag{D.26}$$

$$\frac{1}{2}h^2\alpha_{-1} + \frac{1}{2}\theta^2h^2\alpha_1 + \frac{1}{2}\theta^2(1+\theta)^2h^2\alpha_2 = 0 \tag{D.27}$$

$$-\frac{1}{6}h^3\alpha_{-1} + \frac{1}{6}\theta^3h^3\alpha_1 + \frac{1}{6}\theta^3(1+\theta)^3h^3\alpha_2 = 0 \tag{D.28}$$

Solving equations (D.25) to (D.28) simultaneously gives the specific α coefficients for the upper boundary, which are (with $h = \Delta z_{g,1}$):

$$\alpha_1{}^0 = \frac{1}{(\theta^2\Delta z_{g,1})} \qquad \alpha_2{}^0 = -\frac{\alpha_1{}^0}{(1+\theta)(1+\theta+\theta^2)}$$

$$\alpha_{-1}{}^0 = \theta\left[\alpha_1{}^0 + (1+\theta)\alpha_2{}^0 - \frac{1}{(\theta\Delta z_{g,1})}\right] \qquad \alpha_0{}^0 = -\left(\alpha_{-1}{}^0 + \alpha_1{}^0 + \alpha_2{}^0\right)$$

Lower boundary

For the deepest control volume in the ground, the temperature gradient is approximated by the following relation (from figure D.5, where z_N is the deepest ground node)

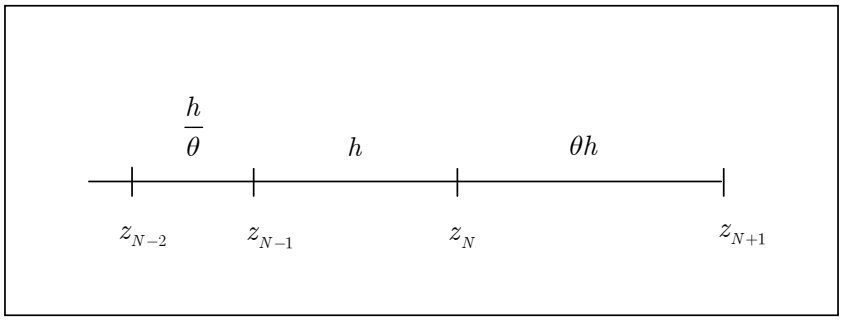

Figure D.5: Lower boundary grid nodes

$$\left.\frac{\partial \phi}{\partial z}\right|_N \approx \alpha_{-2}\phi_{N-2} + \alpha_{-1}\phi_{N-1} + \alpha_0\phi_N + \alpha_1\phi_{N+1} \tag{D.29}$$

The local truncation error is

$$\begin{aligned}
T &= \alpha_{-2}\phi_{N-2} + \alpha_{-1}\phi_{N-1} + \alpha_0\phi_N + \alpha_1\phi_{N+1} - \phi'_N \\
&= \alpha_{-2}\left[\phi - h\left(1+\frac{1}{\theta}\right)\phi' + \frac{h^2}{2}\left(1+\frac{1}{\theta}\right)^2\phi'' - \frac{h^3}{6}\left(1+\frac{1}{\theta}\right)^3\phi''' + O(h^4)\right] \\
&\quad + \alpha_0\phi_N - \phi'_N + \alpha_{-1}\left[\phi - h\phi' + \frac{h^2}{2}\phi'' - \frac{h^3}{6}\phi''' + O(h^4)\right] \\
&\quad + \alpha_1\left[\phi + \theta h\phi' + \frac{(\theta h)^2}{2}\phi'' + \frac{(\theta h)^3}{6}\phi''' + O(h^4)\right] \\
&= \phi_N(\alpha_{-2} + \alpha_{-1} + \alpha_0 + \alpha_1) \\
&\quad + h\phi'_N\left[-\left(1+\frac{1}{\theta}\right)\alpha_{-2} - \alpha_{-1} - \frac{1}{h} + \theta\alpha_1\right] \\
&\quad + \frac{h^2}{2}\phi''_N\left[\left(1+\frac{1}{\theta}\right)^2\alpha_{-2} + \alpha_{-1} + \theta^2\alpha_1\right] \\
&\quad + \frac{h^3}{6}\phi'''_N\left[-\left(1+\frac{1}{\theta}\right)^3\alpha_{-2} - \alpha_{-1} + \theta^3\alpha_1\right] + O(h^4)
\end{aligned} \tag{D.30}$$

Now we choose

$$\alpha_{-2} + \alpha_{-1} + \alpha_0 + \alpha_1 = 0 \tag{D.31}$$

$$-\left(1 + \frac{1}{\theta}\right)\alpha_{-2} - \alpha_{-1} - \frac{1}{h} + \theta\alpha_1 = 0 \tag{D.32}$$

$$\left(1 + \frac{1}{\theta}\right)^2 \alpha_{-2} + \alpha_{-1} + \theta^2\alpha_1 = 0 \tag{D.33}$$

$$-\left(1 + \frac{1}{\theta}\right)^3 \alpha_{-2} - \alpha_{-1} + \theta^3\alpha_1 = 0 \tag{D.34}$$

Solving equations (D.31) to (D.34) simultaneously gives the specific α coefficients for the lower boundary, which are (with $h = \Delta z_{g,\,N}$):

$$\begin{aligned}
{\alpha_{-1}}^{N+1} &= -\frac{\theta}{\Delta z_{g,\,N}} \\
{\alpha_{-2}}^{N+1} &= -\frac{{\alpha_{-1}}^{N+1}}{\left(1 + \frac{1}{\theta}\right)\left(1 + \frac{1}{\theta} + \frac{1}{\theta^2}\right)} \\
{\alpha_1}^{N+1} &= \frac{1}{\theta}\left[{\alpha_{-1}}^{N+1} + \left(1 + \frac{1}{\theta}\right){\alpha_{-2}}^{N+1} + \frac{1}{\Delta z_{g,\,N}}\right] \\
{\alpha_0}^{N+1} &= -\left({\alpha_{-2}}^{N+1} + {\alpha_{-1}}^{N+1} + {\alpha_1}^{N+1}\right)
\end{aligned}$$

D.3 Tower discretization scheme

Buys (2003-2004) also suggested using the same discretization scheme as in section D.1 for the tower of the solar tower power plant. The scheme, given in chapter 2 by equation (2.67), is derived for the tower as follows.

Let

$$\frac{\partial\phi}{\partial z} \approx a\phi_i + b\phi_{i-1} + c\phi_{i-2} \tag{D.35}$$

Then, from figure D.6, the local truncation error is found by

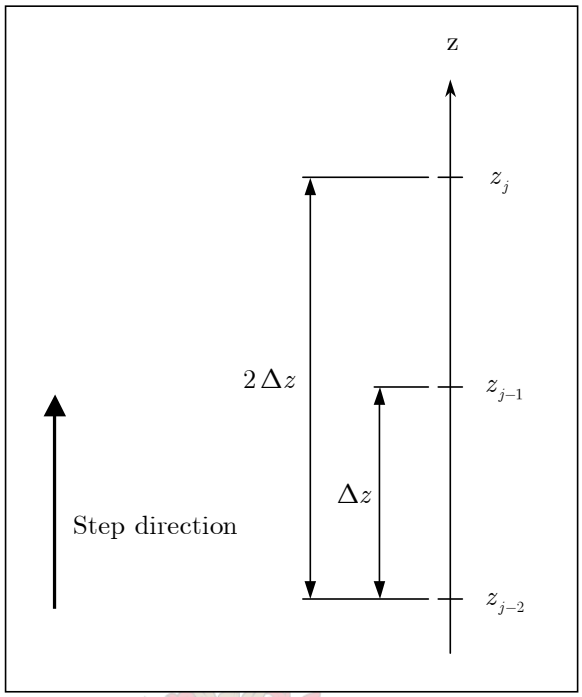

Figure D.6: Tower finite difference grid

$$
\begin{aligned}
T_j &= \frac{\partial \phi}{\partial z}(z_j) - a\phi(z_j) - b\phi(z_j - \Delta z) - c\phi(z_j - 2\Delta z) \\
&= \phi' - a\phi - b\left[\phi - \Delta z\phi' + \frac{(\Delta z)^2}{2}\,\phi'' + O(\Delta z^3)\right] \\
&\quad - c\left[\phi - 2\Delta z\phi' + \frac{(2\Delta z)^2}{2}\,\phi'' + O(\Delta z^3)\right] \\
&= -\phi_j(a+b+c) + \phi'_j(1 + b\Delta z + 2c\Delta z) - \phi''_j\left(\frac{1}{2}\,b(\Delta z)^2 + 2c(\Delta z)^2\right) \\
&\quad + b\,O(\Delta z^3) + c\,O(\Delta z^3)
\end{aligned}
\tag{D.36}
$$

Now, we choose

$$a + b + c = 0 \tag{D.37}$$

$$1 + b\Delta z + 2c\Delta z = 0 \tag{D.38}$$

$$\frac{1}{2}\,b\,(\Delta z)^2 + 2c\,(\Delta z)^2 = 0 \tag{D.39}$$

and find for the constants a, b and c

$$a = \frac{3}{2\Delta z} \qquad b = -\frac{2}{\Delta z} \qquad c = \frac{1}{2\Delta z}$$

When substituting the constants into equation (D.35), we find

$$\left(\frac{\partial \phi}{\partial z}\right)\Big|_j = \frac{3\phi_j - 4\phi_{j-1} + \phi_{j-2}}{2\,\Delta z} + O(\Delta z^2) \tag{D.40}$$

Pectora roborant cultus recti

Appendix E

Determination of Solar Radiative Properties

E.1 Collector roof radiative properties

This section describes the determination of solar radiative properties of a surface, in our case the collector roof. These properties include the effective transmissivity and absorptivity of the collector roof.

Figure E.1 below shows the path that the solar radiation rays follow as they are reflected and transmitted through a semitransparent sheet.

In the figure, ρ_{12} depicts the reflectivity of the upper surface of the sheet, while ρ_{23} represents the reflectivity of the lower surface. The refractive indices of the sheet and surrounding media are given as n_1, n_2 and n_3, while the incident solar radiation on the horizontal surface and the transmissivity due to the absorptance of the sheet are given by I_h and τ_α respectively. The incidence angle is depicted as θ_1 while θ_2 represents the reflective radiation angle.

From figure E.1 it is clear that a fraction of reflected solar radiation keeps bouncing back and forth between the interfaces, until all incident solar energy is depleted by reflection, absorption and transmittance.

In the case of the solar tower power plant, the collector roof will be surrounded by the same media, air. For the special case where the same media surrounds the sheet, $\rho_{12} = \rho_{23} = \rho$.

Also, solar radiation is unpolarized, and consists of a parallel and perpendicular polarization component. From Fresnel's equation in Modest (1993), we

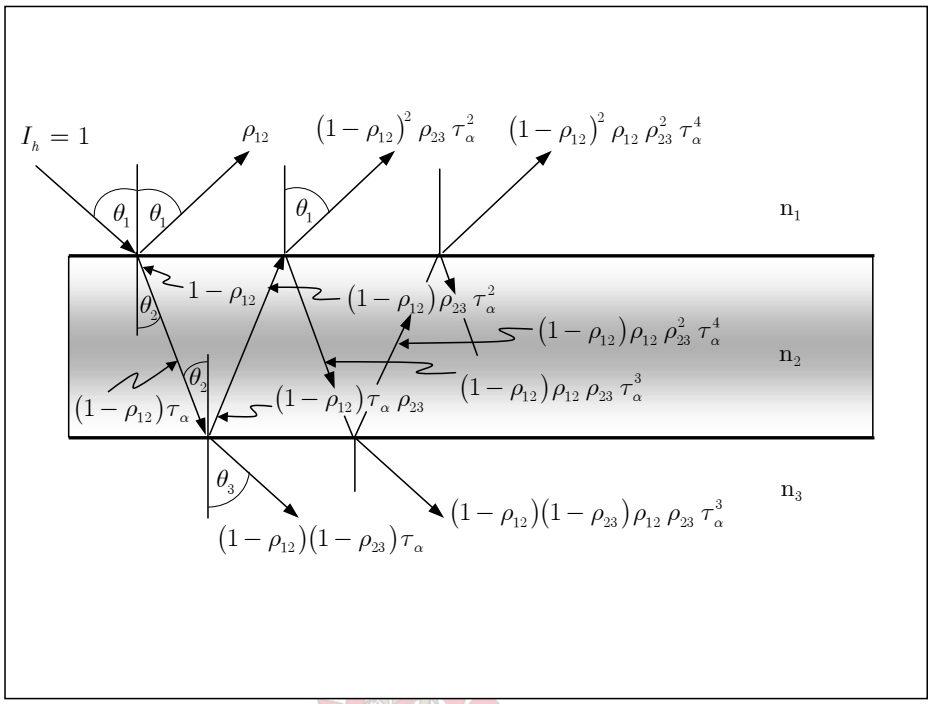

Figure E.1: Reflectivity and transmissivity of a thick semitransparent sheet

find the following relations

$$\rho_{\parallel} = \left[\frac{\tan^2(\theta_1 - \theta_2)}{\tan^2(\theta_1 + \theta_2)}\right] \tag{E.1}$$

for the parallel polarization component of the interface reflectivity, and

$$\rho_{\perp} = \left[\frac{\sin^2(\theta_1 - \theta_2)}{\sin^2(\theta_1 + \theta_2)}\right] \tag{E.2}$$

for the perpendicular polarization component of the interface reflectivity.

For the special case where the same media surrounds the sheet, the transmissivity for the parallel polarization component is given by

$$\tau_{\parallel} = \frac{(1-\rho_{\parallel})^2\tau_\alpha}{1-{\rho_{\parallel}}^2{\tau_\alpha}^2} \tag{E.3}$$

while the absorptivity for the parallel polarization component is described by

$$\alpha_{\parallel} = \frac{(1-\rho_{\parallel})(1-\tau_\alpha)}{1-\rho_{\parallel}\,\tau_\alpha} \tag{E.4}$$

The transmissivity and absorptivity for the perpendicular polarization components can be found analogous to equations (E.3) and (E.4).

The effective sheet radiative properties are determined by the average of the two polarization components, as follows

$$\tau_e = \frac{1}{2}\left(\tau_{\parallel} + \tau_{\perp}\right) \tag{E.5}$$

for the effective transmissivity and

$$\alpha_e = \frac{1}{2}\left(\alpha_{\parallel} + \alpha_{\perp}\right) \tag{E.6}$$

for the effective absorptivity.

Snell's law defines the relation between the incident and refractive angles to the refractive indices of the media as the following

$$\theta_2 = \arcsin\left(\frac{n_1 \sin\theta_1}{n_2}\right) \tag{E.7}$$

Duffie & Beckman (1991) lists some refractive indices for a number of cover materials (see table E.1) while the refractive index of air is approximated as unity.

Table E.1: Average refractive indices for some cover materials

Cover Material	*Refractive Index, n*
Glass	1.526
Polymethyl methacrylate	1.49
Polyvinylfluoride	1.45
Polyfluorinated ethylene propylene	1.34
Polytetrafluoroethylene	1.37
Polycarbonate	1.6

The cover sheet absorbs some of the solar radiation that passes through it. This is known as the transmissivity due to the absorptance of the sheet τ_α. Modest (1993) gives the relation for the transmissivity due to the absorptance for a semitransparent medium as

$$\tau_\alpha = e^{-C_e\, t_r/\cos\theta_2} \tag{E.8}$$

where C_e is the extinction coefficient and t_r is the sheet (collector roof) thickness.

According to Duffie & Beckman (1991), the value of the extinction coefficient C_e varies from approximately 4 m^{-1} for "water white" glass (glass having a whitish colour when viewed on the edge) to approximately 32 m^{-1} for "greenish cast of edge" (having a greenish edge colour) glass. Experiments conducted by Lombaard (2002) found that $C_e = 13\ m^{-1}$ for window pane glass.

In order to determine the interface reflectivity components $\rho_{\parallel}$ and $\rho_{\perp}$ and the transmissivity due to the absorptance τ_{α}, the refractive angle θ_2 and the solar radiation incidence angle θ_1 need to be known.

The calculation of the incidence angle is explained in section E.3.

E.2 Collector ground radiative properties

It is assumed that the ground is a gray and diffuse surface. Therefore, the ground absorptivity is independent of the incident solar radiation direction and is assumed to have the same value as the ground emissivity ($\alpha_g = \epsilon_g$).

E.2.1 The ground transmittance-absorptance product

As illustrated in figure E.2, some of the solar radiation that passes through the transparent collector roof and strikes the ground surface is reflected back to the roof. In turn, some of this reflected radiation is reflected back to the ground. The multiple reflection of diffuse radiation continues, resulting in a higher fraction of energy absorbed by the ground.

From Duffie & Beckman (1991), by summing all the absorbed (reflected) radiation contributions, the fraction of energy ultimately absorbed is

$$(\tau_e \alpha_g) = \tau_e \alpha_g \sum_{n=0}^{\infty} [(1-\alpha_g)\rho_d]^n = \frac{\tau_e \alpha_g}{1-(1-\alpha_g)\rho_d} \tag{E.9}$$

where τ_e is the effective transmissivity of the collector roof, α_g is the ground absorptivity and n is the number of reflections. The variable ρ_d refers to the roof reflectivity for diffuse radiation incident on the bottom side of the roof, and may be estimated using the equation by Duffie & Beckman (1991)

$$\rho_d = \tau_{\alpha d} - \tau_{ed} \tag{E.10}$$

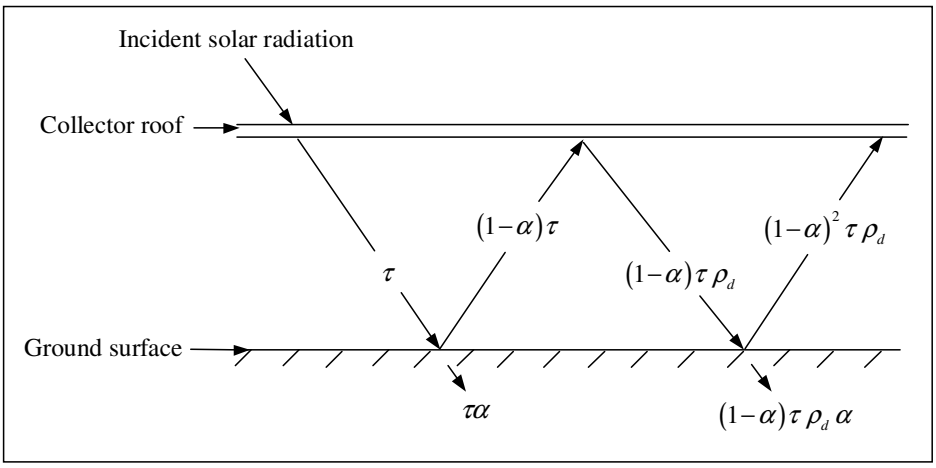

Figure E.2: Absorption of solar radiation by the ground under the collector roof

where $\tau_{\alpha d}$ and τ_{ed} should be evaluated at the equivalent diffuse incidence angle of 60°, as explained in section E.3.1.

E.3 Determination of solar radiation incidence angle

Solar radiation incident on the earth's surface consists of two components, namely beam and diffuse radiation. Beam radiation is that component which falls directly on an object, while diffuse radiation is that part of solar radiation which is received after being scattered in the earth's atmosphere.

E.3.1 Diffuse radiation incidence angle

Diffuse solar radiation is incident from all directions due to scattering in the earth's atmosphere. According to Duffie & Beckman (1991), an equivalent incidence angle of $\theta_1 = \theta_d = 60°$ should be used in calculations regarding the diffuse solar radiative properties of a surface or sheet.

E.3.2 Beam radiation incidence angle

When dealing with beam radiation, the position of the sun relative to a specific plane or point needs to be known. The position of the sun relative to a certain plane can be described in terms of several angles. Some of these angles are indicated in figure E.3.

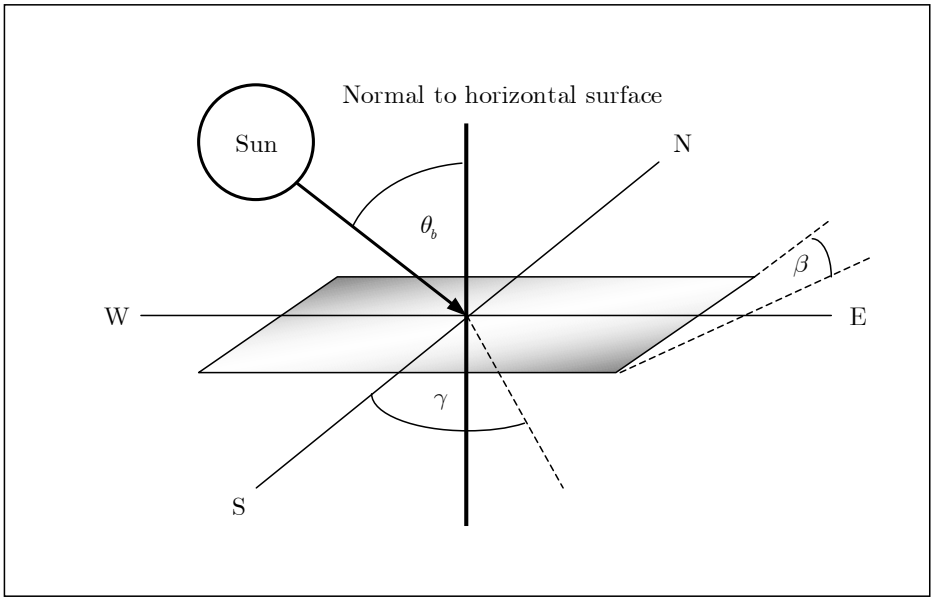

Figure E.3: Some angles describing the position of the sun relative to a plane

From figure E.3, θ_b is the beam solar radiation incidence angle, defined as the angle between the vertical and the line to the sun. The slope angle, β, is the angle between the plane of the surface and the horizontal ($0° \leq \beta \leq 180°$). A perfectly horizontal surface will have a slope angle of $\beta = 0°$. The angle γ is the surface azimuth angle and is defined as the deviation of the projection on a horizontal plane of the normal to the surface (the projection on the horizontal plane of the normal to the surface is given by the direction south in figure E.3), with zero due south, east negative and west positive ($-180° \leq \gamma \leq 180°$).

Duffie & Beckman (1991) give the following equation for calculating the beam radiation incidence angle

$$\begin{aligned}\cos\theta_b = {} & \sin\delta\sin\phi\cos\beta - \sin\delta\cos\phi\sin\beta\cos\gamma + \cos\delta\cos\phi\cos\beta\cos\omega \\ & + \cos\delta\sin\phi\sin\beta\cos\omega\cos\gamma + \cos\delta\sin\beta\sin\omega\sin\gamma\end{aligned} \tag{E.11}$$

where δ is the declination angle, ϕ is the latitude angle and ω represents the hour angle.

The declination angle is defined as the angular position of the sun at solar noon with respect to the plane of the equator, where north is positive ($-23.45° \leq \delta \leq 23.45°$). The latitude angle is the angular position of the spe-

cific location north or south of the equator, where north is defined as positive ($-90° \leq \phi \leq 90°$). The hour angle ω is the angle of the sun east or west of the local meridian, calculated at 15° per hour, with morning angles negative and afternoons positive.

For a slope angle of $\beta = 0°$, as is the assumption for the collector roof of the solar tower power plant, equation (E.11) reduces to

$$\cos\theta_b = \sin\delta\sin\phi + \cos\delta\cos\phi\cos\omega \tag{E.12}$$

Duffie & Beckman (1991) states that the declination angle may be found in degrees using equation (E.13)

$$\delta = 23.45\sin\left(360\,\frac{284 + DOY}{365}\right) \tag{E.13}$$

where DOY is the specific day of the year. The DOY is determined by taking the 1st of January as the first day of the year.

According to Lombaard (2002), the South African Weather Bureau (SAWB) suggests that the following alternative equation be used when calculating the declination angle

$$\begin{aligned}\delta = {} & 0.00661 + 0.40602\sin(P - 1.4075) + 0.00665\sin(2P - 1.4789) \\ & + 0.00298\sin(3P - 1.0996)\end{aligned} \tag{E.14}$$

where δ is in radians and P is the annual phase angle on the specific day of the year, in radians.
P in turn is evaluated by the following equation:

$$P = 0.0172028(DOY + YADJ) \tag{E.15}$$

where YADJ represents the leap year adjustment. According to Lombaard (2002), the SAWB suggests the DOY be increased by 0.417 day in order to determine the annual phase angle at noon South African standard time. Thus equation (E.15) changes to

$$P = 0.0172028(DOY + 0.417 + YADJ) \tag{E.16}$$

for calculations under South African solar conditions.
The leap year adjustment is evaluated according to equation (E.17)

$$YADJ = 0.25\,[2.5 - (Y - 4(integer((Y-1)/4)))] \tag{E.17}$$

where Y indicates the specific year.

The declination angle relations given by equation (E.13) and equation (E.14) are compared with each other for the year 2000 in figure E.4. The slight deviation by the SAWB relation from that of Duffie & Beckman (1991) after day 240 to the end of the year can be ascribed to the fact that the equation by Duffie & Beckman (1991) does not consider any leap year adjustments.

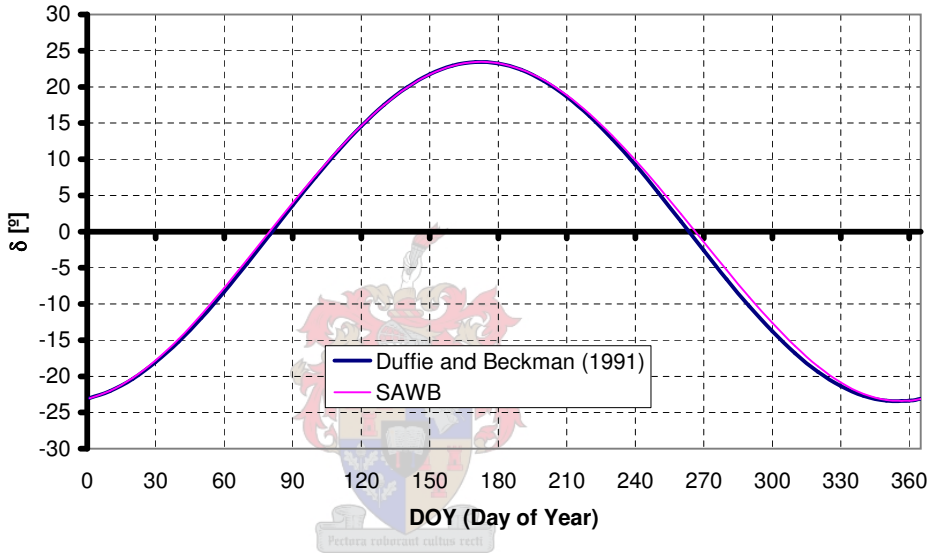

Figure E.4: Declination angle comparison vs. specific day of the year

The numerical model of the solar tower power plant should be able to accommodate any global power plant location. Therefore, due to the fact that there is only such a slight deviation between the declination angle equations of Duffie & Beckman (1991) and the SAWB, equation (E.13) is used for all declination angle calculations at any global location.

The standard time at any location is the commonly used specific time at the particular location, while solar time is based on the sun's position in the sky. Solar noon is when the sun's position is directly overhead.
The hour angle is calculated in degrees using equation (E.18)

$$\omega = 15\,(Solar\ Time - Solar\ Noon) \tag{E.18}$$

where solar noon is 12.

The input data used for the numerical model is given relative to solar time and the output is also generated in this format. Therefore, it was not necessary to convert the standard time at the specific location to solar time. However, for completeness sake, the relations necessary to convert standard time to solar time are also discussed in this section.

In order to convert standard time to solar time (in hours), Duffie & Beckman (1991) suggests the following equation

$$Solar\ Time = Standard\ Time + \frac{4(L_{st} - L_{loc}) + EOT}{60} \tag{E.19}$$

where L_{st} is the standard meridian for the local time zone and L_{loc} represents the specific longitude of the particular location, with longitudes in degrees west ($0° < L < 360°$). The term EOT indicates the equation of time.

Duffie & Beckman (1991) gives a relation for the equation of time (in minutes) as follows:

$$\begin{aligned} EOT = 229.2(&0.000075 + 0.001868\cos B - 0.032077\sin B \\ &- 0.014615\cos 2B - 0.04089\sin 2B) \end{aligned} \tag{E.20}$$

where B is in degrees and is given by

$$B = (n-1)\frac{360}{365} \tag{E.21}$$

where n is the specific day of the year.

According to Lombaard (2002), the SAWB propose the following formula for the equation of time (in minutes)

$$\begin{aligned} EOT = 1440\ [&0.005114\sin(P + 3.0593) + 0.006892\sin(2P + 3.4646) \\ &+ 0.00022\sin(3P + 3.3858) + 0.000153\sin(4P + 3.7766)] \end{aligned} \tag{E.22}$$

where P is once again the annual phase angle, in radians.

When comparing equations (E.20) and (E.22), it is clear from figure E.5 that there is only a very slight variation between the two relations. Therefore, if necessary, equation (E.20) should be used for all time conversion calculations at any global location.

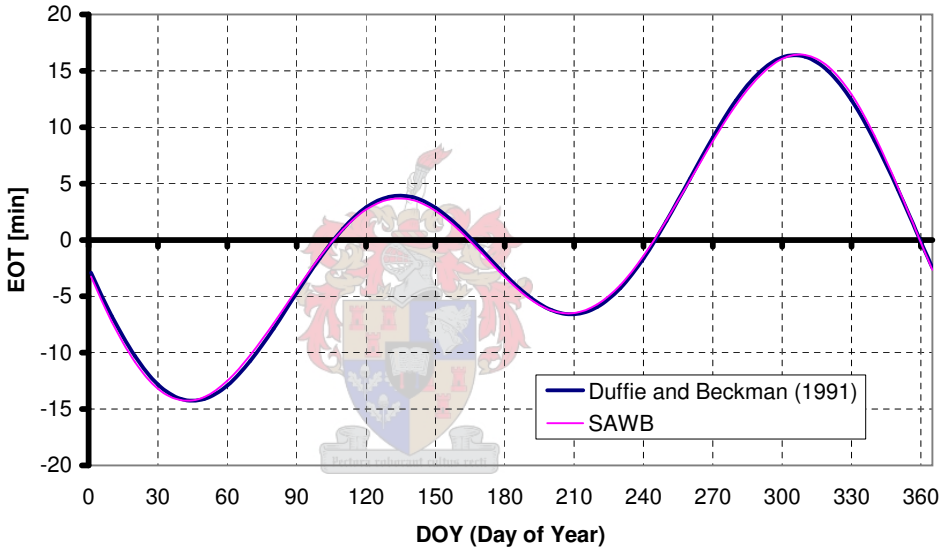

Figure E.5: Equation of Time comparison vs. specific day of the year

Appendix F

Tower Shadow Effects

As the rays from the sun strike the tower of the solar tower power plant, it casts a shadow on the collector. Solar beam radiation does not reach collector areas shaded by the tower, which will undoubtedly affect the power plant performance. This Appendix discusses how the tower shadow effect is taken into account when performing power output calculations.

When inspecting figure F.1, it is clear that the angle between the incident rays from the sun and the normal to the collector roof surface is the beam radiation incidence angle, θ_b. According to Duffie & Beckman (1991), the complement to the beam radiation incidence angle is known as the solar altitude angle, depicted in figure F.1 as α_s.

Also in figure F.1, r_{sh} is the radius reached on the collector by the shadow cast by the tower, while r_2 is the collector perimeter radius.

The solar altitude angle can be expressed in terms of the beam radiation incidence angle as follows:

$$\alpha_s = 90^\circ - \theta_b \tag{F.1}$$

From figure F.1, it is also clear that the radius reached on the collector by the shadow cast by the tower is

$$r_{sh} = \frac{H_t}{\tan \alpha_s} \tag{F.2}$$

During times when the solar altitude angle is very small (early morning and late afternoon), the tower casts very long shadows. At these times r_{sh} is much greater than the collector perimeter radius and consequently r_{sh} is set

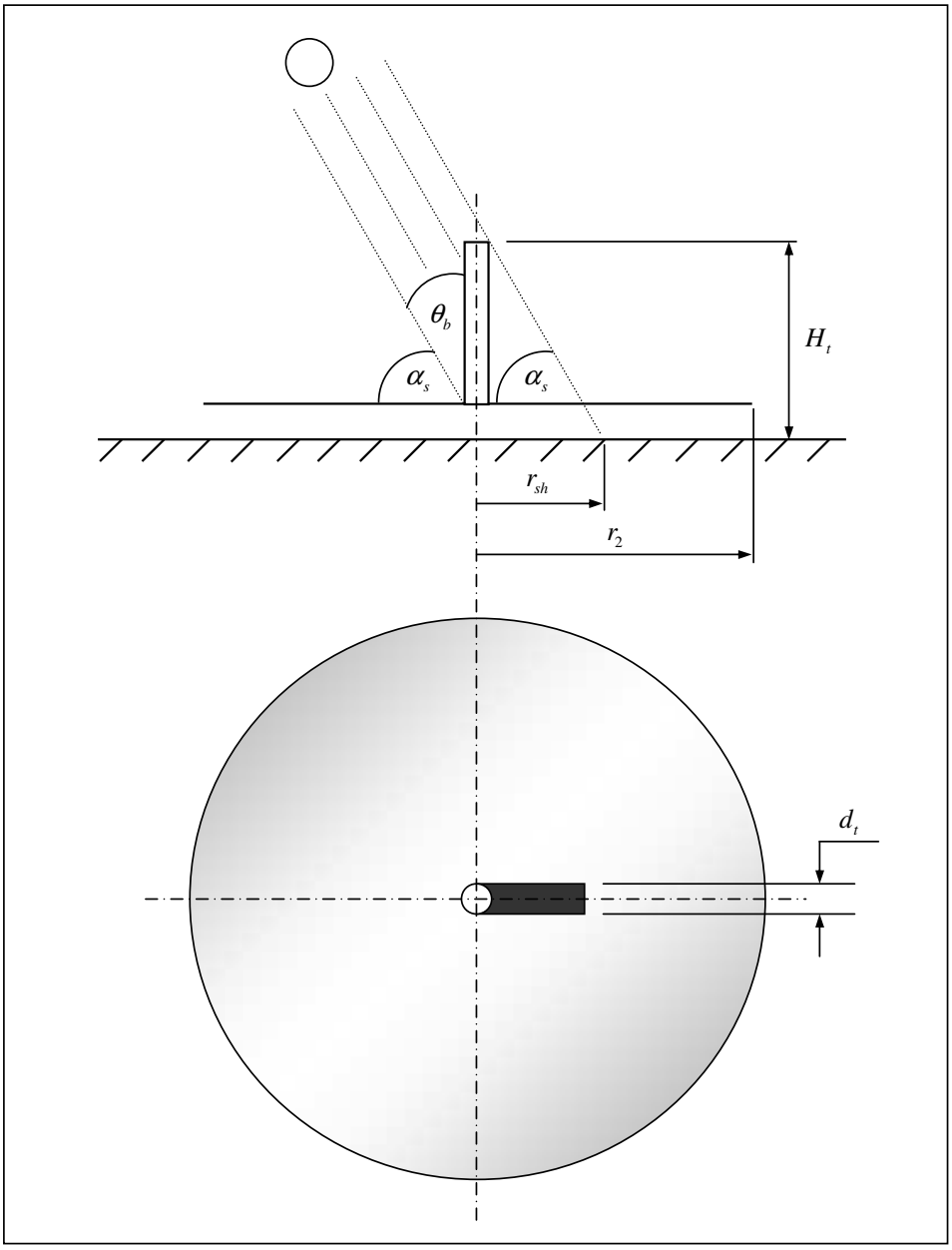

Figure F.1: Frontal and plan view of the solar tower power plant, showing the shadow cast by the tower

equal to r_2. This ensures that only the shadow cast on the collector covered area is taken into consideration.

For the tower shadow calculations, it is assumed that the shadow cast by the tower on the collector may be approximated as rectangular in shape.

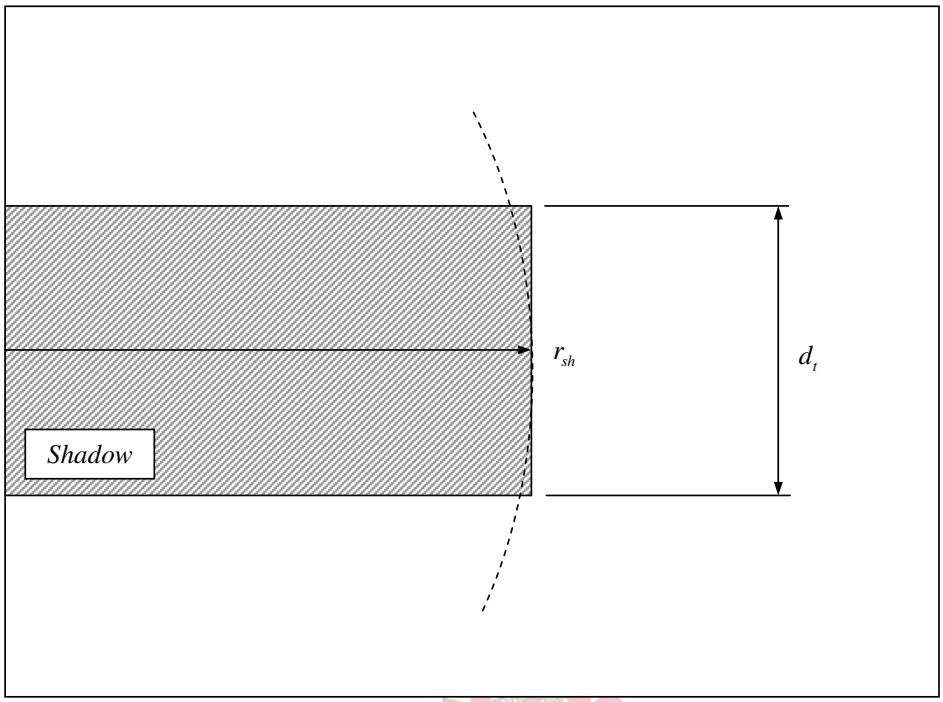

Figure F.2: Tower shadow cast on the collector

When investigating the effect of the tower shadow on the power output of the solar tower power plant, the following strategy is employed.

It is assumed that when part of the collector surface is in shadow, no direct (beam) radiation reaches that part of the collector. It will however receive diffuse radiation.

The strategy is firstly to calculate the percentage of the collector in shadow. Then, the same percentage of direct radiation is subtracted from the total direct radiation incident on the collector roof.

As can be seen in figure F.2, we firstly approximate the shaded area as:

$$A_{sh} = (r_{sh})(d_t) \tag{F.3}$$

where the width of the shadow is taken as the tower diameter, d_t.

The total collector area is

$$A_{coll} = \pi(r_2)^2 \tag{F.4}$$

Therefore, the percentage of the collector in shadow is given by

$$A_{sh,\,\%} = \left(\frac{A_{sh}}{A_{coll}}\right) \times 100 = \frac{(r_{sh})(d_t)}{\pi(r_2)^2} \times 100 \tag{F.5}$$

By taking the tower shadow into account, the effective beam radiation incident on the collector roof now becomes

$$I_{hb,\,e} = I_{hb}\left(\frac{100 - A_{sh,\,\%}}{100}\right) \tag{F.6}$$

Appendix G

Ambient Wind Effects

Many previous studies (by authors such as Buxmann (1983) and Du Preez (1992)) have confirmed that windy ambient conditions affect the performance of cooling towers. It is therefore imperative that the effect of wind on the performance of a solar tower power plant also be evaluated.

This Appendix conducts a preliminary analysis on the performance of a solar tower power plant in the presence of wind. The analysis takes into account the effect of cross-winds on top of the collector roof and at the tower outlet. The effect of cross-winds at the collector inlet is not considered.

G.1 Reference ambient wind speeds

Ambient wind speed measurements were made by the South African Weather Bureau (SAWB) at Kathu, near Sishen (the reference location and proposed plant site for this study) in South Africa. Hourly averages of these measurements for an average day in each month are given in table C.4. The wind speeds were measured at a height of 10 m above ground level. As with the solar radiation values and ambient air temperatures given in tables C.2 and C.3, these wind speeds are used (at a reference height of 10 m) as input to the numerical simulation model.

G.2 Effect of cross-winds on collector roof

The effect of a cross-wind on top of the collector roof is incorporated into the model of the solar tower power plant through the very approximate equation

(2.44), by substituting an ambient wind velocity into v_w (whose value is normally zero for no-wind conditions). This equation calculates the convective heat transfer coefficient h_{ra} for determining the convective heat flux from the collector roof to the ambient air.

As this is only a preliminary study regarding wind effects, the cross-wind velocity v_w substituted into equation (2.44) is taken as the interpolated (as explained in section C.4) reference wind velocity from table C.4. Therefore, although the collector roof height increases from the perimeter towards the tower, the ambient wind velocity profile is assumed constant over the height of the collector roof. Also, no boundary layer or flow development considerations are introduced at this stage regarding the ambient air flow over the collector roof.

G.3 Effect of cross-winds at tower outlet

A fluid flowing across a cylinder causes the static pressure to vary circumferentially around the cylinder. A cross-wind blowing across the tower of the solar tower power plant has a similar effect. During windy conditions the pressure differential changes, causing either an increased or decreased airflow through the solar tower power plant, which affects the plant performance.

The above mentioned pressure differential (Δp_{to}) can be expressed in terms of a tower outlet loss coefficient K_{to}, which varies significantly under no-wind and windy conditions. Section 3.3.5 discusses in further detail how the model evaluates K_{to} during windy (and no-wind) conditions.

In order to incorporate the wind effect at the tower outlet into our model, we need to determine the cross-wind velocity at the tower outlet height. The following section describes the strategy followed for approximating such an ambient wind velocity profile.

G.4 Approximated wind velocity profile

It has already been mentioned in this appendix that a constant ambient velocity profile is assumed over the height of the collector roof.

A study by Burger *&* Scorgie (1999) presents the monthly average wind speed distribution from ground level to high altitudes for Upington (near Sishen) in South Africa. This data was compared to the measurements at

Kathu (near Sishen) given in table C.4. For each month, the monthly average wind speed data corresponding to an approximate height of 1500 m was found to be in the range of twice the speed of the measured values at 10 m above ground level.

It should be stated once again that since this is a preliminary study regarding wind effects, an accurate ambient wind velocity profile will not be introduced in the current study. It is therefore assumed that the ambient wind velocity employed at the height of the tower outlet be approximated as twice that of the interpolated value for a specific time step at 10 m above ground level.

Pectora roborant cultus recti

Appendix H

Reference Solar Tower Power Plant

For the purpose of comparison, a reference solar tower power plant and a typical operating environment is defined (see figure 1.1 for dimensional details).

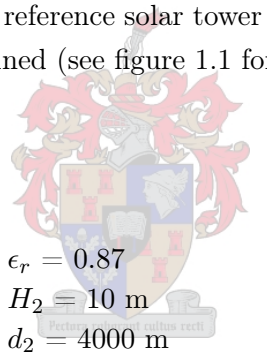

Collector Roof

Emissivity	$\epsilon_r = 0.87$
Perimeter height	$H_2 = 10$ m
Perimeter diameter	$d_2 = 4000$ m
Inside diameter	$d_3 = 400$ m
Inlet loss coefficient	$K_i = 1$
Roughness	$\varepsilon_r = 0$ m
Support diameter	$d_s = 0.15$ m
Support drag coefficient	$C_{sD} = 1$
Supports tangential pitch	$P_t = 10$ m
Supports radial pitch	$P_r = 10$ m
Extinction coefficient	$C_e = 32$ m^{-1}
Roof shape exponent	$b = 0.5$
Refractive index	$n_r = 1.526$
Thickness	$t_r = 0.005$ m

Ground

Type	Granite
Emissivity	$\epsilon_g = 0.9$
Absorbtivity	$\alpha_g = 0.9$
Density	$\rho_g = 2640$ kg/m^3
Specific heat	$c_{pg} = 820$ J/kgK
Thermal conductivity	$k_g = 1.73$ W/mK
Roughness	$\varepsilon_g = 0.05$ m

Tower

Height	$H_t = 1500$ m
Inside diameter	$d_t = 160$ m
Bracing wheel (one) drag coefficient	$K_{bw} = 0.01$
Number of bracing wheels	$n_{bw} = 10$
Inside wall roughness	$\varepsilon_t = 0.002$ m

Turbine

Turbo-generator efficiency	$\eta_{tg} = 80$ %
Inlet loss coefficient	$K_{turb,\,i} = 0.25$

Ambient conditions

Atmospheric pressure	$p_a = 90000$ N/m^2
Wind speed	$v_w = 0$ m/s

Appendix I

Control Volume and Time Step Selection

In order to reduce computational time when running a simulation, short control volume and time step analyses were performed. The goal is to determine the fewest number of control volumes and the largest time step which can be employed without sacrificing significant accuracy.

I.1 Control volume selection

The plant used for the control volume selection analysis is the reference plant as given in Appendix H. The input data given in Appendix C is used as input data to the plant.

A simulation period of one month was employed and the peak power output calculated on 31 January. The simulations were all run on a Pentium III 600 MHz computer with 512 MB RAM.

I.1.1 Tower control volume selection

The number of collector control volumes was kept constant at 50, while running simulations for an increasing number of tower control volumes. Table I.1 shows the comparative results for the various number of tower control volumes employed, where the computing time refers to the computer working time needed to complete all calculations for simulating one calender month.

From table I.1 it is clear that the number of tower control volumes do not have a significant effect on the computing time needed. Also, it appears that

Table I.1: Computing time and peak power output results for varying tower control volumes

Number of tower control volumes	**Computing time** $[minutes]$	**Peak power output** $[MW]$
10	8	92.8975
25	8	91.4406
50	8	91.2349
100	8	91.1841
200	10	91.1713
300	12	91.1688

there is no considerable change in the peak output value when using more than 50 tower control volumes.

Therefore, 50 tower control volumes will be employed in all simulations unless stated otherwise.

I.1.2 Collector control volume selection

From the results of the previous subsection, the number of tower control volumes was kept constant at 50, while running simulations for an increasing number of collector control volumes. Table I.2 gives the comparative results for various numbers of collector control volumes employed, where the computing time again refers to the computer working time needed to complete all calculations for simulating one calender month.

Table I.2: Computing time and peak power output results for varying collector control volumes

Number of collector control volumes	**Computing time** $[minutes]$	**Peak power output** $[MW]$
10	3	90.0011
25	5	91.0792
50	8	91.2349
100	14	91.2698
200	28	91.2753
300	41	91.278

In this case, from table I.2 it is clear that varying the number of collector control volumes does have a significant effect on the computing time. The peak power output solution seem to converge at 50 collector control volumes.

Therefore, 50 collector control volumes will be used in all simulations unless stated otherwise.

I.2 Time step selection

Simulations were also run in order to conduct a time step selection analysis. The input data given in Appendix C is used as input data to the plant.

Due to the transient nature of the ground and the slow thermal conduction into the ground, the deep ground temperatures may take some years to stabilize. In order to assure relatively stable results, the time step selection simulations are repeated for a number of times thereby simulating a number of years with the same energy input. Table I.3 gives the results of the computer simulations for different time steps. The computing time referred to in table I.3 is the computer working time needed to complete all calculations for simulating one calender year.

The simulations were all run on a Pentium III 600 MHz computer with 512 MB RAM.

Table I.3: Computing time and annual power output results for various time step values

Time step (Δt) $[minutes]$	**Computing time** $[minutes]$	**Annual power output** $[GWh/a]$
1	672	318.39442
5	187	321.68504
10	106	323.76414

The most accurate solution we will be able to acquire will be with a one minute time step. From table I.3 it is clear, however, that a simulation employing such a time step will take more than 11 hours to complete. A time step of 10 minutes drastically decreases this computation time to less than 2 hours. We now investigate the loss in accuracy due to larger time steps.
For $\Delta t = 5$ minutes, the error compared to the 1 minute time step solution is:

$$\frac{(321.68504 - 318.39442)}{318.39442} \times 100 = 1.0335\ \% \tag{I.1}$$

while the error with $\Delta t = 10$ minutes compared to $\Delta t = 1$ minute is:

$$\frac{(323.76414 - 318.39442)}{318.39442} \times 100 = 1.686\ \% \tag{I.2}$$

Therefore, with $\Delta t = 10$ minutes a solution is obtained within 2 % of the most accurate solution. In light of this, a time step of 10 minutes will be employed for all simulations unless stated otherwise.

Appendix J

Sample Calculation to Evaluate Flow Development in Collector

When the ambient air enters the solar tower power plant at the collector inlet, a boundary layer develops on the ground surface and on the underside of the collector roof. As the air flows through the collector, the boundary layer on each of these surfaces grows and the flow moves from a developing flow to a fully developed flow regime.

Previous numerical solar tower power plant models have tested for flow development in the collector and have employed both a developing flow and fully developed flow region. The present study assumes that the flow into the collector becomes fully developed fairly rapidly and therefore employs a fully developed flow regime throughout the collector. The aim of this assumption is to simplify the numerical model of the solar tower power plant by only incorporating a fully developed flow regime into the model.

This Appendix validates the above mentioned assumption by establishing the negligible effect of the developing flow region, by calculating the radial distance into the collector at which point the flow becomes fully developed. Sample calculations are done for two cases: for the reference plant described in Appendix H and for the (optimized) reference plant with collector inlet height of $H_2 = 3.1$ m and roof shape exponent $b = 1$ (as in chapter 5).

J.1 Reference plant

The calculations performed in the following section pertains to the reference plant described in Appendix H. The plant conditions in table J.1 and J.2 are selected from simulated reference plant results on January 1st at 13:00.

For the airflow over the collector roof, an approximated mean air temperature (between the collector roof and collector air) is selected near the collector inlet. Similarly, an approximated mean air temperature (between the ground surface and collector air) is selected near the collector inlet when calculating the boundary layer thickness on the ground surface.

J.1.1 Collector roof

Table J.1: Conditions at the collector roof surface, selected from simulated reference plant results on 1 January at 13:00

Mass flow rate	238707.96 kg/s
Mean air temperature near collector inlet	311.9 K

The dynamic viscosity may be calculated from the equation given by Kröger (2004)

$$\begin{aligned}\mu_m &= 2.287973\times10^{-6} + 6.259793\times10^{-8}\ T_m \\ &\quad - 3.131956\times10^{-11}\ {T_m}^2 + 8.15038\times10^{-15}\ {T_m}^3 \\ &= 2.287973\times10^{-6} + 6.259793\times10^{-8}\ (311.9) \\ &\quad - 3.131956\times10^{-11}\ (311.9)^2 + 8.15038\times10^{-15}\ (311.9)^3 \\ &= 1.90127501\times10^{-5}\ \text{kg/m·s}\end{aligned} \tag{J.1}$$

According to Kröger & Buys (1999), radial flow between two surfaces becomes fully developed when the boundary layer thickness $\delta \approx \frac{H_2}{2}$, where H_2 is the collector inlet height as indicated in figure 1.1. Therefore, the flow should become fully developed when

$$\delta \approx \frac{H_2}{2} = \frac{10}{2} = 5\ \text{m} \tag{J.2}$$

Kröger & Buys (1999) suggest the use of equation (J.3) for determining the boundary layer thickness for flow over a smooth surface

$$\delta(r) = H_2 \Bigg\{ \frac{1}{6.218 - 15.08\,b} \left(\frac{r_2}{H_2}\right) \left(\frac{\mu_m r_2}{\dot{m}}\right)^{0.2} \times \left[\left(\frac{r}{r_2}\right)^{1.2-0.2\,b} - \left(\frac{r}{r_2}\right)^{2.743-3.943\,b} \right] \Bigg\}^{5/6} \tag{J.3}$$

where b is the roof shape exponent and r_2 is the collector perimeter radius, as indicated in figure 1.1.

By following an iterative procedure we find for $r = 1551$ m

$$\begin{aligned} \delta(1551) &= 10 \Bigg\{ \frac{1}{6.218 - 15.08(0.5)} \left(\frac{2000}{10}\right) \left(\frac{(1.90127501\times10^{-5}\,)(2000)}{238707.96}\right)^{0.2} \\ &\quad \times \left[\left(\frac{1551}{2000}\right)^{1.2-0.2(0.5)} - \left(\frac{1551}{2000}\right)^{2.743-3.943(0.5)} \right] \Bigg\}^{5/6} \\ &= 5.000674 \text{ m} \end{aligned}$$

The answer to equation (J.3) is approximately equal to the prescribed boundary layer thickness found in equation (J.2), which predicts that the flow will become fully developed at a collector radius of $r = 1551$ m.

Thus we find that for the reference plant, the airflow over the underside of the collector roof becomes fully developed at 449 m from the collector inlet.

J.1.2 Ground surface

Table J.2: Conditions at the ground surface, selected from simulated reference plant results on 1 January at 13:00

Mass flow rate	238707.96 kg/s
Mean air temperature near collector inlet	323 K

Analogous to equation (J.1), the dynamic viscosity is determined by

$$\begin{aligned}\mu_m &= 2.287973\times10^{-6} + 6.259793\times10^{-8}\ T_m \\ &\quad - 3.131956\times10^{-11}\ {T_m}^2 + 8.15038\times10^{-15}\ {T_m}^3 \\ &= 2.287973\times10^{-6} + 6.259793\times10^{-8}\ (323) \\ &\quad - 3.131956\times10^{-11}\ (323)^2 + 8.15038\times10^{-15}\ (323)^3 \\ &= 1.95142197\times10^{-5}\ \text{kg/m·s}\end{aligned} \tag{J.4}$$

For flow over rough surfaces, Kröger & Buys (1999) suggest the use of equation (J.5) for determining the boundary layer thickness.

$$\begin{aligned}\delta(r) &= H_2 \left(\frac{\varepsilon_g}{H_2}\right)^{0.2026} \left(\frac{r_2}{H_2}\right)^{0.7974} \\ &\times \left\{ q \frac{\left(\frac{r}{r_2}\right)^{1.51-0.51\,b} - \left(\frac{r}{r_2}\right)^{2.866-4.12\,b}}{2.55 - 6.787\,b} + \frac{\frac{r}{r_2} - \left(\frac{r}{r_2}\right)^{2.866-4.12\,b}}{17.38 - 38.37\,b} \right\}^{0.7974}\end{aligned} \tag{J.5}$$

where ε_g is the ground roughness and q is determined as

$$\begin{aligned}q &= \left(\frac{\mu_m H_2 r_2}{\varepsilon_g \dot{m}}\right)^{0.51} = \left(\frac{(1.95142197\times10^{-5})(10)(2000)}{(0.05)(238707.96)}\right)^{0.51} \\ &= 0.005157243\end{aligned} \tag{J.6}$$

By following an iterative procedure find at $r = 1849$ m (and with equation (J.6)) that equation (J.5) gives

$$\begin{aligned}\delta(1849) &= 10 \left(\frac{0.05}{10}\right)^{0.2026} \left(\frac{2000}{10}\right)^{0.7974} \\ &\quad \times \left\{ (0.005157243) \frac{\left(\frac{1849}{2000}\right)^{1.51-0.51(0.5)} - \left(\frac{1849}{2000}\right)^{2.866-4.12(0.5)}}{2.55 - 6.787(0.5)} \right. \\ &\qquad \left. + \frac{\frac{1849}{2000} - \left(\frac{1849}{2000}\right)^{2.866-4.12(0.5)}}{17.38 - 38.37(0.5)} \right\}^{0.7974} \\ &= 5.001646316\ \text{m}\end{aligned}$$

The answer to equation (J.5) is approximately equal to the prescribed boundary layer thickness found in equation (J.2). This implies that the flow will become fully developed at a collector radius of $r = 1849$ m.

Therefore we find that for the reference plant, the airflow over the ground surface in the collector becomes fully developed at 151 m from the collector inlet.

J.2 Optimized reference plant

This section repeats the calculations performed in the previous section for an optimized reference plant with collector inlet height of $H_2 = 3.1$ m and roof shape exponent $b = 1$ (as in chapter 5). Except for H_2 and b, all the conditions, plant dimensions and properties are similar to those of the reference plant given in Appendix H. The plant conditions in table J.3 and J.4 are selected from simulated results for this plant on January 1st at 13:00.

Once again, approximated mean air temperatures are selected for the collector roof and ground surfaces.

J.2.1 Collector roof

Table J.3: Conditions at the collector roof surface, selected from simulated results for the optimized reference plant on 1 January at 13:00

Mass flow rate	229180.1 kg/s
Mean air temperature near collector inlet	308.3 K

Once again, the dynamic viscosity may be calculated from

$$\begin{aligned}\mu_m &= 2.287973\times10^{-6} + 6.259793\times10^{-8}\ T_m \\ &\quad - 3.131956\times10^{-11}\ {T_m}^2 + 8.15038\times10^{-15}\ {T_m}^3 \\ &= 2.287973\times10^{-6} + 6.259793\times10^{-8}\ (308.3) \\ &\quad - 3.131956\times10^{-11}\ (308.3)^2 + 8.15038\times10^{-15}\ (308.3)^3 \\ &= 1.88488607\times10^{-5}\ \text{kg/m·s}\end{aligned} \tag{J.7}$$

For this plant, the flow should become fully developed when

$$\delta \approx \frac{H_2}{2} = \frac{3.1}{2} = 1.55 \text{ m} \tag{J.8}$$

Analogous to equation (J.3), the boundary layer thickness for flow over the smooth collector surface is found at $r = 1880$ m

$$\begin{aligned}\delta(1880) = 3.1\Bigg\{ & \frac{1}{6.218 - 15.08(1)} \left(\frac{2000}{3.1}\right) \left(\frac{(1.88488607\times10^{-5}\ )(2000)}{229180.1}\right)^{0.2} \\ & \times \left[\left(\frac{1880}{2000}\right)^{1.2-0.2(1)} - \left(\frac{1880}{2000}\right)^{2.743-3.943(1)}\right]\Bigg\}^{5/6} \\ & = 1.56063447 \text{ m}\end{aligned} \tag{J.9}$$

The result from equation (J.9) is approximately equal to the calculated boundary layer thickness of 1.55 m necessary for fully developed flow. Thus the flow will become fully developed at a collector radius of $r = 1880$ m.

Therefore we find that for the optimized reference plant, the airflow over the underside of the collector roof becomes fully developed relatively quickly, i.e. at 120 m from the collector inlet.

J.2.2 Ground surface

Table J.4: Conditions at the ground surface, selected from simulated results for the optimized reference plant on 1 January at 13:00

Mass flow rate	229180.1 kg/s
Mean air temperature near collector inlet	312.9 K

Employing equation (J.1) once again, the dynamic viscosity is

$$\begin{aligned}\mu_m &= 2.287973\times10^{-6} + 6.259793\times10^{-8}\ T_m \\ &\quad - 3.131956\times10^{-11}\ {T_m}^2 + 8.15038\times10^{-15}\ {T_m}^3 \\ &= 2.287973\times10^{-6} + 6.259793\times10^{-8}\ (312.9) \\ &\quad - 3.131956\times10^{-11}\ (312.9)^2 + 8.15038\times10^{-15}\ (312.9)^3 \\ &= 1.90581658\times10^{-5}\ \text{kg/m·s}\end{aligned} \tag{J.10}$$

From equation (J.6), we calculate q as

$$\begin{aligned}q &= \left(\frac{\mu_m H_2 r_2}{\varepsilon_g \dot{m}}\right)^{0.51} = \left(\frac{(1.90581658\times10^{-5}\ )(3.1)(2000)}{(0.05)(229180.1)}\right)^{0.51} \\ &= 0.002862834\end{aligned} \tag{J.11}$$

By once again following an iterative procedure find at $r = 1966$ m (and with equation (J.11)) that equation (J.5) gives

$$\begin{aligned}\delta(1966) &= 3.1\left(\frac{0.05}{3.1}\right)^{0.2026}\left(\frac{2000}{3.1}\right)^{0.7974} \\ &\quad\times\left\{(0.002862834)\frac{\left(\frac{1966}{2000}\right)^{1.51-0.51(1)} - \left(\frac{1966}{2000}\right)^{2.866-4.12(1)}}{2.55-6.787(1)}\right. \\ &\qquad\left. + \frac{\frac{1966}{2000} - \left(\frac{1966}{2000}\right)^{2.866-4.12(1)}}{17.38-38.37(1)}\right\}^{0.7974} \\ &= 1.5613585\ \text{m}\end{aligned} \tag{J.12}$$

The answer to equation (J.12) is approximately equal to the determined boundary layer thickness necessary for fully developed flow for this particular plant. Therefore, the flow will become fully developed at a collector radius of $r = 1966$ m.

Thus we find that for the optimized reference plant, the airflow over the ground surface in the collector becomes fully developed at 34 m from the collector inlet.

J.3 Discussion of results

From table J.5 it is clear that the flow over the ground surface becomes fully developed much earlier than the flow over the collector roof surface. The ground surface boundary layer will have a dominating effect, causing the total airflow in the collector to become fully developed as the flow over the ground surface becomes fully developed.

Table J.5: Summary of results - Determination of flow development

	Reference plant	**Optimized reference plant**
Point of fully developed flow over collector roof surface (from collector inlet)	449 m	120 m
Point of fully developed flow over ground surface (from collector inlet)	151 m	34 m

Therefore we assume that the total airflow in the collector will become fully developed at 151 m from the inlet for the reference plant and at 34 m from the inlet for the optimized reference plant. These distances are 7.55 % and 1.7 % respectively of the total collector radius.

It is thus considered reasonable to assume a fully developed flow regime throughout the collector.